UNIVERSITÁ DEGLI STUDI DI MILANO &
UNIVERSITÁ CATTOLICA DEL SACRO CUORE

DIPARTIMENTO DI MATEMATICA E FISICA

CORSO DI DOTTORATO DI RICERCA IN
FISICA, ASTROFISICA E FISICA APPLICATA
Ciclo XXIX

Growth, local structural and electronic properties, and band alignment at $SrTiO_3$-based all-oxide heterojunctions

Settore Scientifico Disciplinare FIS/03

Tesi di Dottorato di:
Alessio Giampietri

Coordinatore: Prof. Francesco Ragusa

Tutore: Prof. Luigi Sangaletti

A. A. 2016-2017

Commission of the final examination:

External Member:
Guido Faglia

External Member:
Alberto Paleari

Internal Member:
Luigi Sangaletti

Final examination:

Date 21/02/2017

Università Cattolica del Sacro Cuore, Dipartimento di Matematica e Fisica, Brescia, Italy

To the ones I will never forget.

Cover illustration:

X-ray photoemission spectroscopy study of a $BiFeO_3/SrTiO_3$ heterostructure: band alignment results and X-ray photoelectron diffraction analysis

Internal illustrations:

None

Illustrator:

Alessio Giampietri

MIUR subjects:

FIS/03

Keywords:

RF Sputtering, Growth characterization, Band alignment, Oxide heterostructures, $SrTiO_3$, X-ray photoemission spectroscopy, X-ray photoelectron diffraction

Contents

Introduction

Motivation

Recent advances in the growth of epitaxial oxide thin films have fostered a steady increase of research on perovskite oxide heterojunctions, which are now produced with unprecedented quality. Applications of these systems in the field of electronics [1], photovoltaics [2] and photocatalysis [3] strongly rely on the capability to master band gap engineering on the atomic scale in ultra-thin interfaces. Strontium titanate ($SrTiO_3$, STO) is the substrate of choice commonly used in the production of all-oxide heterostructures [4], as in many cases these systems display a two dimensional electron gas (2DEG) confined at the interface, such as in the $LaAlO_3/SrTiO_3$ junction [5]. The band offsets at the interface determine on which of the constituent materials the 2DEG will be confined [6], and provide additional information on the degree of confinement as well [7], so the study of the band alignment in oxide-based heterostructures is of crucial importance. Novel properties and functionalities can be achieved upon substitution of $LaAlO_3$ with other oxide materials, an example being the $BiFeO_3$ perovskite. In fact, $BiFeO_3$ is a multiferroic material [8], and a complete control of the $BiFeO_3/SrTiO_3$ heterostructure may allow the tuning of the 2DEG at the interface through the application of an external electric or magnetic field, which can indeed control the surface polarization. The growth of non-perovskite oxide materials on a $SrTiO_3$ substrate expands the range of possible applications. Indeed, a 2DEG is observed also in the $Al_2O_3/SrTiO_3$ junction, which show electron mobilities greater than those previously measured in perovskite-based heterojunctions [9]. Despite in many structures the 2DEG is not observed, different interesting applications can still be obtained, such as in the $CuO/SrTiO_3$ heterostructure, which is a promising material for the production of solar cells [10] and for photoelectrochemical water splitting applications [11]. Usually, such heterostructures are grown by PLD (pulsed laser deposition), MBE (molecular beam epitaxy) and less commonly by sputtering deposition. However sputtering is fast, cheap, and produces samples with a large practicable area, and high quality films, suitable for device fabrication, can be obtained through the use of an off-axis sputtering geometry [12]. The main objective of this work is to demonstrate the growth of high quality $BiFeO_3/SrTiO_3$, $Al_2O_3/SrTiO_3$ and $CuO/SrTiO_3$ heterostructures by off-axis sputtering, and to provide a detailed analysis of the interface properties. The band alignment at the interface is thus measured and discussed for each of these materials.

Thesis overview

The present thesis is organized in five chapters. In the first chapter the band alignment at oxide interfaces is reviewed. The most common methods to experimentally track the band alignment at the interface are presented, and the band alignment configurations at the $LaAlO_3/SrTiO_3$ heterointerface are shown. Furthermore, other conducting and insulating STO-based all-oxide heterostructures are also considered. In the second chapter the experimental details are provided, and a short description of the main experimental techniques used is reported. In the third chapter a detailed description of the $SrTiO_3$ substrate is provided, and the analysis of surface and bulk defects by resonant photoemission techniques is discussed. In the fourth chapter the growth of $BiFeO_3$ is calibrated upon deposition on Si, and the $BiFeO_3/SrTiO_3$ interface is accurately studied. In the last chapter non-perovskite $SrTiO_3$-based interface are investigated, namely $Al_2O_3/SrTiO_3$ and $CuO/SrTiO_3$. A complete characterization of the interfaces is presented, from the growth process to the measurements of the band alignment.

CHAPTER 1

Band alignment at heteroepitaxial perovskite oxide interfaces

1.1 Introduction

A key focal point in modern condensed matter science is the study of the exotic phenomena which can arise at the interface between two oxide materials, such as the formation of a two-dimensional electron gas (2DEG) at the interface between the wide-gap insulators lanthanum aluminate ($LaAlO_3$, LAO) and strontium titanate ($SrTiO_3$, STO) [5] [13] [14] [15] [16] [17] [18] [19]. The oxides junction properties are crucially dependent on the energy bands alignment at the interface, corresponding to the conduction band offset (CBO) and the valence band offset (VBO) between the two materials. Thus the analysis of the electronic structure and band alignment at oxide heterostructure interfaces is necessary for a complete understanding of these interesting phenomena; indeed a complete and fine control on these properties would favor the production of novel oxide electronic and photovolatic devices [20] [21] [22] [23] [24] [25]. The band offsets are however not known a priori, but must be measured experimentally and eventually compared to theoretical predictions obtained through simulations.

The study of band alignment in oxide heterostructures is a critical step in the evaluation of the electrical and optical material properties. The VBO study provides important information about the current transport, potential distribution and quantum carrier confinement at the interfaces, and thus determines the performance of the devices which use these peculiar phenomena [26]. The band alignment determines the height of the barrier for hole and electron transfer through the interface [27] and can depend on the possible presence of interface dipoles which can modify the band alignment diagram consistently with their orientation. Accordingly, the band alignment can be tuned by the introduction of additional charges at the interface, with the consequent formation of a dipole due to induced screening charge [28] [29].

In the field of oxides, the main applications of band offset engineering are the 2DEG confinement control, all-oxide photovoltaics and photocatalysis; and the direct evaluation of the band alignment is usually performed through X-ray photoelectron spectroscopy (XPS) measurements. It should be pointed out that in XPS measurements the VBOs can vary slightly with the photon energy, thus adding an additional parameter which should be tuned in VBO studies in order to determine the correct interface electronic structure [30]. Regarding photovoltaic applications the possibility of a band flattening induced by photocarriers should also be taken into account [31]. The band offset at the interface determines on which of the constituent materials the 2DEG will be confined, and provide additional information on the degree of confinement as well. In fact, electrons are located in the side of the interface whose energy of the conduction band is lower than the one of adjacent materials. The 2DEG is usually assumed to be confined

near the interface in a triangular potential well [32], as will be discussed further later in this work.

The band alignment of an oxide heterostructure is strongly sensitive on the structural properties and interface composition [29] [33] of the materials involved, such as strain [34], grain orientation [35], surface atomic termination [36], oxygen vacancies [31], chemical ligands at the surface [37], film thickness [38], and interdiffusion [39]. Even the presence of a single interface monolayer of secondary phase may induce a strong variation in band offsets [40], thus high-quality samples are needed for the study of the band alignment of a heterojunction.

The aim of this chapter is to discuss the band alignment of all-oxide perovskite heterojunctions where top perovkite layer is grown mainly on $SrTiO_3$ substrates. In Section 1.2 the possible band alignment configurations are discussed, while the experimental and theoretical methods for the evaluation of the band alignment are reported in Section 1.3. In Section 1.4 the determination of band alignment in 2DEG systems is discussed. Finally, in Section 1.5 the discussion is brought beyond the materials that display the 2DEG at the interface, by considering non-perovskite layers grown on $SrTiO_3$. Examples are drawn from all-oxide photovoltaics and photocatalysis system that to some extent can provide new ideas to engineer novel oxide heterojunctions.

1.2 Band alignment configurations

The band alignment characteristic of an heterojunction can be classified into three main configuration schemes, as shown in Figure 1.1: (1) Type I (or straddling) heterojunction, (2) Type II (or staggered) heterojunction, and (3) Type III (or broken-gap) heterojunction. In a type-I heterojunction, the VBO and CBO of the two materials have opposite sign, while in a type-II heterojunction, the VBO and CBO signs are identical. A type III heterojunction is a peculiar case of the type II band alignment, where the valence band of one of the constituent materials overlaps the conduction band of the other material at the interface, thus forming two gaps which show no superimposition [26].

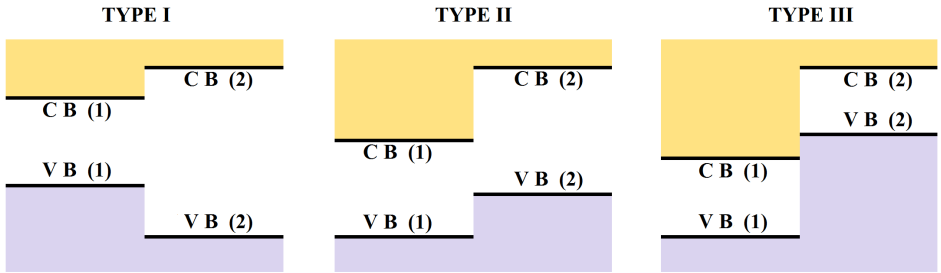

Figure 1.1: Schematic representation of the different band alignment configurations, determined by the conduction band (CB) and valence band (VB) offset of the two materials.

The formation of a type I heterojunction induces a concurrent confinement of both electrons and holes inside one of the constituent materials (Figure 1.2 (a)), thus rendering the heterostructure suitable for high-efficiency luminescence and optoelectronic devices, an example being the $Co_3O_4/SrTiO_3(001)$ interface [20]. A type I heterojunction is necessary for the employment of a material as a transistor gate dielectric. In fact, in a straddling band alignment the gate leakage is predicted to be negligible, while hetero-

junctions with a small CBO show a remarkable leakage current across the interface, an example being $SrTiO_3$-Si based devices [41]. A remarkable application of a type I junction is the creation of a 2DEG at the interface due to the transfer of electrons (which is related to the possible presence of an internal electric field) from the material with the higher-conduction band edge into the conduction band of the oxide on the other side of the interface (Figure 1.2 (b)). The electrons are then spatially confined in one of the constituent materials [42], as will be seen more in detail in Section 1.4.

When a type II band alignment occurs, electrons are transferred in one side of the junction, and holes are collected at the other one (Fig. 1.2 (c)). This results in electrons and holes confined in different layers, and this carrier separation can be exploited in photovoltaic applications. Indeed a type II alignment is more suitable for the production of photovoltaic devices than a type I interface, since only indirect transitions between holes and electrons confined in different materials are possible, while a type I band alignment usually shows worse performance in terms of a faster electron-hole recombination and a smaller radiative lifetime following an external photon excitation [20]. However, in a type II band alignment the effective energy gap for interface recombination (distance between the VB of one material and the CB of the second one) is smaller than the band gaps of the two materials, and this may result in a increased recombination rate and reduced open-circuit voltage [33], thus a careful band alignment analysis is usually needed.

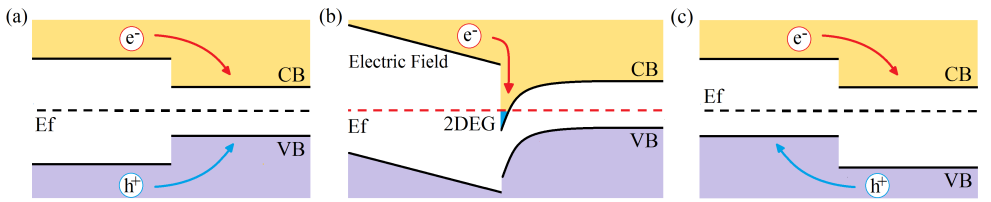

Figure 1.2: (a) Schematic representation of the charge confinement in a type I heterojunction. (b) Two-dimensional electron gas generation in a type I heterojunction. (c) Confinement of electrons and holes in different materials in a type II heterojunction.

1.3 Methods to determine band alignment

The band alignment at the interface between two materials can be investigated by several analytical and theoretical methods. X-ray photoelectron spectroscopy (XPS) is one of the main experimental techniques employed for the analysis of the band alignment, due to the possibility to directly probe the valence band of a material. The valence band offset (VBO) in an heterojunction can thus be evaluated by two main independent methods. The first one involves the decomposition of the valence band spectrum of the heterostructure, by performing a linear combination of pristine materials VB spectra [43]. Alternatively, the band alignment can be determined by the study of energy differences in core level pairs between the heterostructure and constituent materials [31]. Additionally, with XPS it is also possible to directly measure the Fermi energy position and thus its distance to the valence band maximum (VBM). The presence of a built-in potential or a band bending at the interface should be taken into account in order to evaluate the band alignment correctly. These properties can be estimated by analyzing the presence of a valence band weight in the gap or at the chemical potential, and looking for signs

of any asymmetry or spectral change in emission angle-dependent measurements [9]. Notched bands have been indeed one of the focus issues in $LaAlO_3/SrTiO_3$ and related heterointerfaces, and the effects of notches in x-ray photoemission core levels have been carefully considered by several authors [9] [43] [44] [45]. These effects will be thoroughly discussed later in this chapter (Section 1.4).

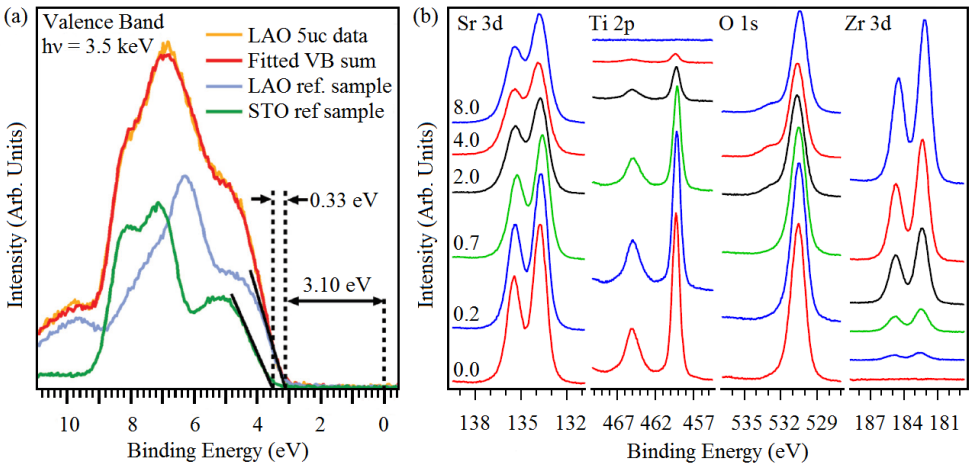

Figure 1.3: Methods to determine the band alignment in an heterojunction. (a) Valence band spectrum of a 5 u.c. $LaAlO_3/SrTiO_3$ heterostructure and its decomposition into the individual $LaAlO_3$ and $SrTiO_3$ contributions. The black lines indicate the determination of the VBM energies. Adapted from [31]. (b) X-ray induced core level spectra of $SrTiO_3$ recorded during the interface formation with $SrZrO_3$. The Ti 2p and Zr 3d peaks should be used to determine the band alignment. The $SrZrO_3$ thickness is given in nm. Adapted from [46].

1.3.1 Linear combination method

In this method the VB for the heterojunction is reproduced by a linear combination of VB spectra for the bulk constituent materials, which thus interpolate the experimental data measured for the heterojunction (Figure 1.3 (a)) [31]. The relative energy shift and intensity are introduced as fitting parameters to be determined, where the intensities take into account the thickness of the film. The fitting procedure determines the relative energy shift in the constituent materials valence bands, and enables the evaluation of the valence band maximum (VBM) at each side of the junction. The VBM can be directly determined from the intersection between a linear extrapolation of the VB leading edge and the zero-intensity constant background [47], which takes into account for the finite resolution of the spectrometer. Evidently, the VBM value is very sensitive to the position of the leading edge point chosen to obtain the regression line [48]. However, this linear method has been proven to yield correct VBMs with an accuracy of about ± 0.1 eV [47]. The conduction band maximum (CBM) of each material can be subsequently determined by considering the respective band gap.

1.3.2 Core levels method

The method proposed by Kraut *et al.* [49] is based on the assumption that the spectrum of a heterojunction is the superposition of the separate spectra of each constituent layer. In the heterostructure, the valence bands maxima are aligned with a certain offset; however, the energy separation between core levels and the VBM edge in principle doesn't change. The valence band offsets at the interface are thus evaluated by the analysis of the binding energy difference between two specific core-level peaks which should be present only in a single layer of the heterojunction, such as Zr 3d and Ti 2p core-levels for the $SrZrO_3/SrTiO_3$ interface (Figure 1.3 (b)) [46]. The energy difference between a core level and the respective VBM has to be determined in both bulk materials, and the same core levels energy position have to be evaluated in the heterojunction, accordingly. From these data is possible to calculate the valence band offset through the following expression:

$$VBO = (E_{Peak1} - E_{VBM1})_A - (E_{Peak2} - E_{VBM2})_B - (E_{Peak1} - E_{Peak2})_{A/B}$$

where the A/B subscript denotes the heterostructure, E_{VBM1} and E_{Peak1} are the valence band maximum and the binding energy of the selected core level evaluated for the first bulk material (A), while E_{VBM2} and E_{Peak2} are measured on the second bulk material (B). In the last term of the equation E_{Peak1} and E_{Peak2} are evaluated in the heterojunction. Three samples are thus necessary for the complete evaluation of the band alignment: two bulk, homogeneous films to determine the energy position of a core level with respect to the VBM, and the respective heterostructure to determine the selected core level offsets. In addition, it is essential to measure the separate core level binding energies with at least an accuracy of $\pm$ 20 meV in order to archive a maximum $\pm$ 100 meV error for the valence band offset, which is determined through several differences and sums of these measured binding energies [30].This method is often used to probe the band alignment of oxide heterointerfaces [50] [51] and, in particular of the $LaAlO_3/SrTiO_3$ junction [52] [53] [54].

1.3.3 Calculations

Although this review is mainly focused on the experimental results of band alignment, it is important to point out the importance of the theoretical calculation as a support of the experimental analysis. Indeed, several authors studied the band alignment through first-principle calculations and helped to archive a better description of the interesting phenomena underlying oxide heterojunctions [29] [32] [44] [55] [56] [57] [58].

Usually the band alignment at an interface between two materials is obtained by initially performing calculations for the first bulk material and second separately, in which the VBM and CBM are evaluated referenced to the bulk average electrostatic potential. As a second step, the average electrostatic potentials at the two sides of the junction are aligned by carrying out a calculation for the resulting interface. In this case, the difference between the average electrostatic potentials of the two bulk materials is evaluated in a region far enough from the interface [59]. Complications in the simulation of the correct band alignment are mainly due to the presence of strain phenomena or the formation of a 2DEG. Furthermore, the presence of additional electrons generate a dipole that can shift the bands used for the calculated alignment [6]. The band alignment across an interface can be also displayed through the calculation of the local density of states (LDOS) projected on the central unit cell of the heterojunction for all the materials involved [29].

1.3.4 Alternative methods to determine band alignment

Transitivity Rule - The transitivity rule determines the band alignment in an heterojunction through the comparison with the already known band offsets of two heterostructures, whose constituent layers are a common material and the two components (one located in the first heterostructure, and the other located in the second) of the heterojunction which band alignment must be determined. In other words, the transitivity rule makes use of the band offsets at the junction between A and B materials and between B and C materials, and add them up in order to obtain the band offset between materials A and C [60] [61]. However, the transitivity rule is demonstrated to be inapplicable in the general case, as the error in the band offset evaluation can be greater than 0.5 eV [55].

Electron Affinity Rule - An alternative estimation of the energy band alignment can be obtained from the electron affinity rule [62], which is based on the vacuum level alignment at the interface. The valence band and conduction band offsets are determined through the analysis of the differences in ionization potential and electron affinity, respectively. However the band alignment predicted by the electron affinity rule can show a strong deviation due to the possible formation of dipoles at the interface [63].

1.4 Applications on solid state physics, $SrTiO_3$-based interfaces

1.4.1 The $LaAlO_3/SrTiO_3$ heterostructure

The formation of a two-dimensional electron gas (2DEG) at the interface between the two wide-gap insulators $LaAlO_3$ (LAO) and $SrTiO_3$ (STO) [5] represents one of the more discussed topics in the field of solid state physics. The insulator to metal transition of this heterostructure is found to occur when 4 unit cells or more of LAO are grown on a STO substrate [15] and only if the substrate displays an uniform TiO_2 termination [64]. The origin of the 2DEG is highly debated, and the three more supported hypotheses are: the electronic reconstruction between the film and the substrate (due to the growth of the polar LAO on the non-polar STO) [65], the formation of oxygen vacancies in the substrate during the growth [66], and the intermixing between film and substrate [52]. In particular the band alignment determines which side of the heterojunction hosts the 2DEG, and if the band offset magnitude is sufficient to produce a charge confinement [6]. In this case, the band edge position can be analyzed in detail through resonant photoemission techniques (Figure 1.4), since resonant photoemission spectroscopy (RESPES) measurements are more interface-sensitive with respect to standard photoemission with a laboratory X-ray source, which is more bulk-sensitive due to the higher kinetic energies collected. In resonant photoemission the valence band spectra are collected by resonantly enhancing the spectral weight of selected elements in the valence band region. This occurs when the incoming photon energy is tuned to the absorption threshold of the selected element. For instance, the valence band alignment of $LaAlO_3$ and $SrTiO_3$ is determined by selectively enhancing the valence band edge of $LaAlO_3$ and $SrTiO_3$ by collecting RESPES data at the La M-edge and Ti L-edge respectively. The demonstration of the possibility to probe buried Ti states at the interface [67] fostered a number of studies aimed to study the band structure of the buried states [68] [69] [70], and also offered the possibility to carry out an interface sensitive evaluation of band alignment through soft X-ray electron spectroscopies.

The unusual electronic properties of the LAO/STO interface are linked to the band bending at the STO side, which produces a notched structure in the conduction band

adjacent to the interface where surface charges tend to accumulate (Figure 1.2 (b)). The properties of a potential band bending within the STO substrate have been studied intensively by density functional theory (DFT) calculations, which predict a bending of the conduction band minimum [44] ranging from 180 meV [71] up to 500 meV [9], corresponding to a electrostatic confinement of mobile carriers within 3-5 unit cells into the substrate. The resulting in-gap spectral weight is due to Ti 3d electronic states, whose bands host the 2DEG electrons at the interface [56].

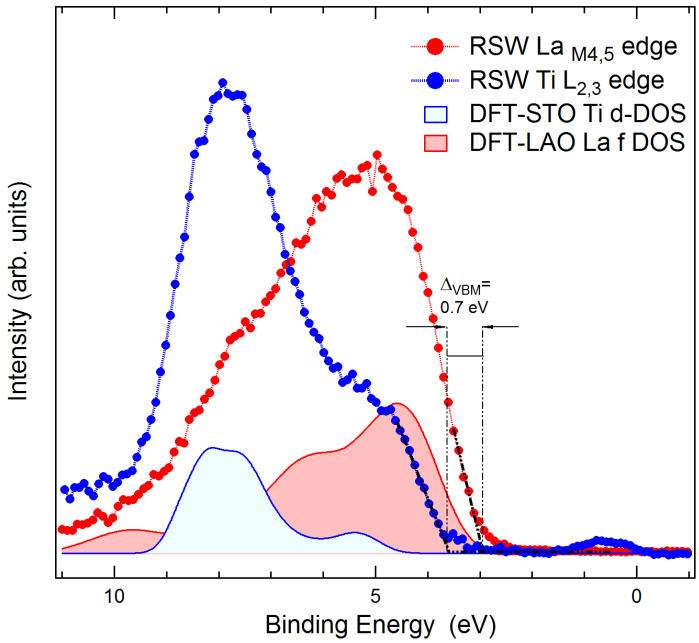

Figure 1.4: Comparison of La 4f and Ti 3d valence band resonating contribution with Ti d-DOS DFT calculation performed on a STO bulk crystal and La f-DOS DFT calculation performed on a LAO film. Adapted from [43].

The profile of the notched structure can be analysed by directly probing the shift of the VBM with the variation of the film thickness (Figure 1.5 (d)) or take-off angle, which introduce a different probing depth in XPS measurements. Alternatively, the band banding can be studied by the analysis of asymmetric line shapes of core levels, since the bending of the valence band corresponds to a shift of the core-level binding energies. In this case, the measured spectral features would consist of a superposition of peaks whose binding energy change in function of depth; as a result, an asymmetric peak shape with a larger FWHM (respect to pristine material) can be measured [52] (Figure 1.5 (a)). Furthermore, this band bending is only observed in conductive LAO/STO interfaces (obtained from the deposition on TiO_2 terminated STO substrates, Figure 1.5 (b)), while insulating interfaces show a flat-band behavior (Figure 1.5 (c)). The band bending is also influenced by the interaction with a tip in the analysis of band alignment by STM [72] [73], which can even bring the CB on the STO side below the Fermi level [74]. The band bending is difficult to determine experimentally, and the existence and the depth of the $SrTiO_3$ potential well is still discussed in literature. An upper limit of 1 ± 0.1 eV was

estimated by photoemission measurements [43], and typically a band bending of 0.25 ± 0.07 eV is claimed for the LAO/STO interface [45]. However, other works show that, within experimental error (± 0.06 eV), there is no detectable band bending within the STO [52] [75], possibly due to intermixing phenomena [76].

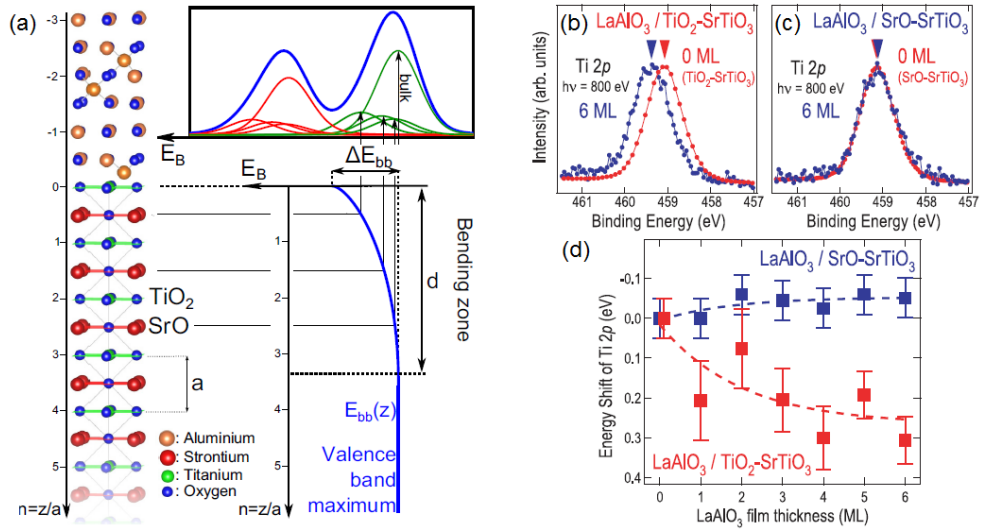

Figure 1.5: (a) Schematic representation of the effect of band bending in the STO substrate on the Sr 3d XPS peaks line shape. The peak from each SrO layer is shifted in energy according to the bending potential $E_bb(z)$. Adapted from [9]. Band bending in $SrTiO_3$ of the Ti2p XPS core level for: (b) TiO_2-terminated metallic and (c) SrO-terminated insulating $LaAlO_3/SrTiO_3$ heterostructures. (d) Resulting plots of the band-bending induced energy shift of the Ti 2p XPS peaks as a function of the $LaAlO_3$ film thickness. Adapted from [45].

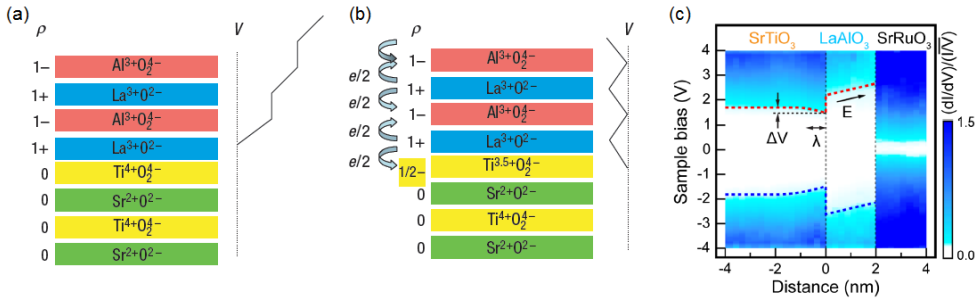

Figure 1.6: (a) Polar catastrophe: the junction between a non-polar material (STO) and a polar material (LAO) leads to an electric potential which diverges with thickness. (b) Electronic reconstruction model: the transfer of half an electron from the LAO surface to the interface induces a finite potential and avoids the polar catastrophe. Adapted from [65]. (c) Spatially resolved scanning tunneling spectroscopy analysis performed on the LAO/STO heterostructure. The band alignment results in a built-in electric field (E) in the LAO layer. The amorphous $SrRuO_3$ (SRO) buffer layer is necessary to prevent tip crash in STM measurements. Adapted from [74].

In the electronic reconstruction scenario, the STO can be subdivided in TiO_2 and SrO charge neutral planes, while the LAO can be subdivided in LaO and AlO_2 polar planes (Figure 1.6 (a)). Thus in order to avoid a polar catastrophe the interfacial LaO layer should donate $0.5e^-$ for each unit cell (Figure 1.6 (b)), which thus flow to the interface due to the large conduction-band offset characteristic of the LAO/STO heterojunction. The electrostatic potential within the LAO layer is represented by the slope of the LAO bands, and should be in principle flat if no charge is transferred through the interface. However, in order to corroborate the electronic reconstruction model, a built-in electric field in the LAO layer is theoretically necessary [57] [77] and detected in few studies [74] [78] (Figure 1.6 (c)). The presence of an electric field in the LAO layer was however excluded by spectroscopic measurements [4] [31] [43] [52] [53]. Indeed, the electronic reconstruction theory would have several consequences which could be detected by photoemission measurements, such as the broadening and binding energy shift in the LAO core levels, or the presence of LAO valence band states crossing the chemical potential, due to the presence of a potential gradient within the LAO film. Despite those features are unobserved experimentally, the flat band situation can be still theoretically explained by the presence of oxygen vacancies in the LAO film [44] [79]. This picture indeed restores the electronic reconstruction scenario with the introduction of oxygen vacancy-induced empty defect states, which replace the hole states of the metallic LAO surface band [68].

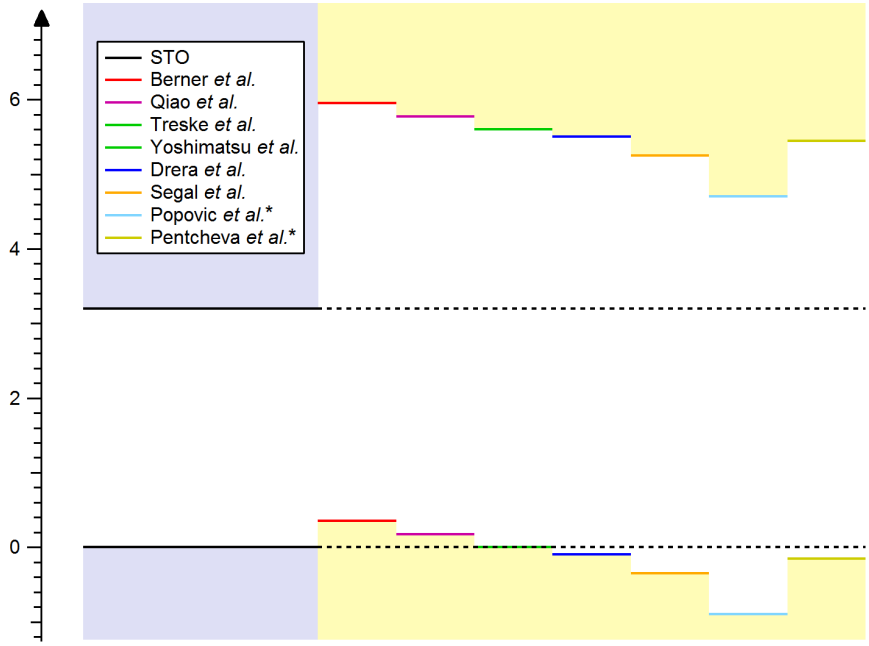

Figure 1.7: Band alignment at the $LaAlO_3/SrTiO_3$ interface as reported by several authors.

The band alignment at the $LaAlO_3/SrTiO_3$ interface has been widely investigated by several authors in literature. The values for the VBO reported vary to a certain degree, with several groups claiming a type I interface [44] [53] [56] [58]. Other groups come to the contrary results, and a type II interface was obtained [31] [76] [80]. Situations with a relatively small value for VBO are also reported (the VB maxima of LAO and STO are

almost aligned), where the discrimination between a type I and a type II junction can be affected by some degree of uncertainty (estimated as $\pm$ 0.2 eV) [4] [43] [45]. These results are summarized in Figure 1.7 and in Table 1.1.

Author	VBO ($\pm$ 0.2 eV)	Alignment	Band Bending
Berner *et al.* [31]	0.35	Type II	Yes
Qiao *et al.* [80]	0.17	Type II	No
Treske *et al.* [4]	0.00	-	Yes
Yoshimatsu *et al.* [45]	0.00	-	Yes
Drera *et al.* [43]	-0.10	Type I	Yes
Segal *et al.* [53]	-0.35	Type I	-
Popović *et al.** [58]	-0.90	Type I	-
Pentcheva *et al.** [56]	-0.15	Type I	-

Table 1.1: Band alignment results at the $LaAlO_3$ and $SrTiO_3$ interface as reported by several authors. The band alignments obtained through calculations are marked with a *. In some cases the discrimination between a type I and a type II junction can be affected by some degree of uncertainty, so the heterojunction type is not reported. The presence of a band bending at the interface, whenever discussed, is also reported.

This remarkable inconsistency in band alignment configuration could be due to the different deposition methods (mainly pulsed laser deposition and molecular beam epitaxy) and growth conditions employed. In order to obtain an agreement in the band alignment a growth protocol is thus needed.

1.4.2 Beyond the $LaAlO_3/SrTiO_3$ interface: other $SrTiO_3$-based heterostructures displaying a 2DEG

The existence of a two dimensional electron gas in the LAO/STO heterojunction triggered a wide search for different materials which could display this intriguing property, mainly thin films grown on STO as a common substrate. For instance, a 2D conductive layer has been detected in $PrAlO_3$, $NdAlO_3$, $NdGaO_3$ and $LaGaO_3$ [81] epitaxial layers on STO.

The research for new heterostructures is often evaluated through calculations [32]. The 2DEG was indeed predicted for the $GdTiO_3/SrTiO_3$ (GTO/STO) heterojunction, where the band bending necessary for a charge confinement is observed for every GTO film thickness considered [57]. A material which share a similar band alignment with the GTO/STO (the difference in their valence-band offsets is within 0.1 eV) is the $YTiO_3$ on $SrTiO_3$ (YTO/STO) heterojunction. Janotti et al. [6] showed that both these interfaces display an excess of electrons, which will be confined on the STO substrate. However the resulting 2DEG is characterized by different densities at the interface respect to the LAO/STO heterostructure. The band gap for many perovskite oxide materials is provided by calculations in the work of Bjaalie et al. [32] (Figure 1.8), where the possible formation of a 2DEG in heterostructures made by a combination of various perovskites is discussed. In this case, separate calculations for the constituent bulk materials are initially performed in order to obtain the VBM and CBM respect to the average electrostatic potential of each material, then these electrostatic potentials are aligned by carrying out a calculation for the heterostructure.

The 2DEG in STO-based junctions is found experimentally in many materials, including those with non-perovskitic overlayer, such as the epitaxial interface with γ-Al_2O_3 (GAO) studied by Schütz et al. [9]. Here, a type I band alignment was measured and

the relative valence band offset at the GAO/STO interface was ≈600 meV. Furthermore, a downward band bending was detected, which results in the CBM of STO crossing the chemical potential near to the interface. The 2DEG is also found by Treske et al. [4] in the $LaGaO_3/SrTiO_3$ and $NdGaO_3/SrTiO_3$ heterojunctions, which display a STO band bending similar to the one observed in the LAO/STO heterostructure. Indeed, a downward interface band bending of 0.4 eV is revealed by XPS measurements carried out at different emission angles, with the consequent generation of a confining potential in the STO substrate at increasing overlayer thickness. The conduction band thus bends downwards, crosses the Fermi level energy and hosts the 2DEG. A built-in electric field is not observed in these heterostructures, and the valence band maximum of the thin film layers are aligned to the valence band maximum of the STO substrate. These results are consistent with the electronic reconstruction model triggered by defects, where the charge transfer to the interface is provided by surface donor states. The 2DEG is predicted by band alignment measurements also in the $BaSnO_3/SrTiO_3$ heterointerface [7], where the observed type II band alignment show a $BaSnO_3$ (BSO) CBM lower in energy than that of the STO substrate, resulting in a carrier confinement within the BSO film.

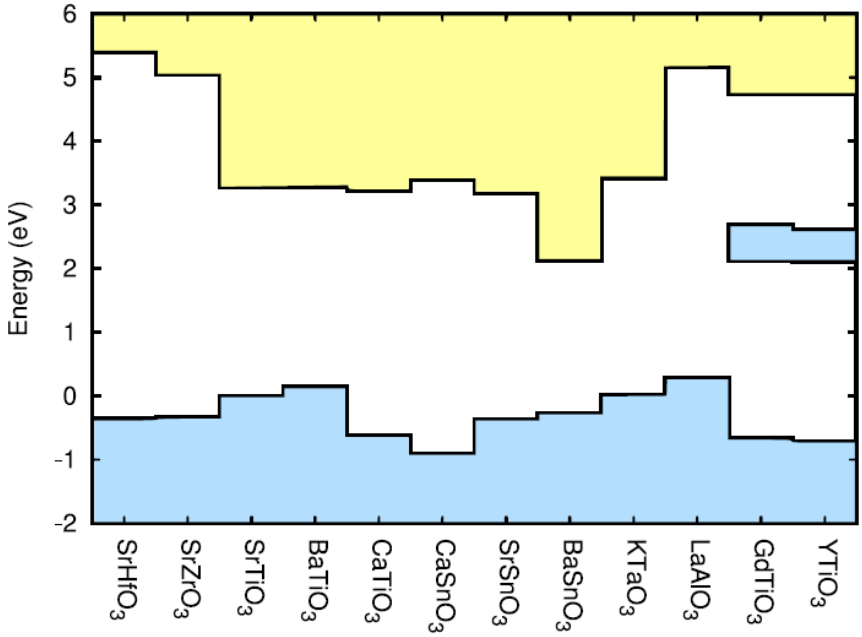

Figure 1.8: Calculated band gaps for various perovskite oxide materials. The VBM of STO was used as the zero of energy. Adapted from [32].

In some works the conductivity was not found, an example being the $LaCrO_3/SrTiO_3$ (LCO/STO) heterostructure studied by Chambers et al. [82]. In principle, the electronic reconstruction model predicts that with an increasing film thickness the electrostatic potential within the LCO film should also increase; and thus the valence band maximum of the LCO film should cross the STO conduction band minimum. The electronic charge should thus be confined within the STO substrate, generating a conductive phase at the interface. However, the type II interface obtained is insulating for each LCO film

analyzed, included films whose thickness should be enough to activate the electronic reconstruction.

The band alignment found at the interface between many oxides materials and a STO substrate is summarized in Figure 1.9 and in Table 1.2. Most of the perovskite oxides display a low valence band offset (usually less than 0.5 eV) with the $SrTiO_3$ substrate, with an exception being the $BiFeO_3$ (VBO = 0.9 eV), and such interfaces usually host a two-dimensional electron gas. A 2DEG is also predicted in the heterojunction with the Mott-insulators $GdTiO_3$ [83] and $YTiO_3$ [6], which display a valence band (lower Hubbard band) almost aligned with the conduction band of STO; this characteristic is due to the peculiar electronic properties of Mott insulators.

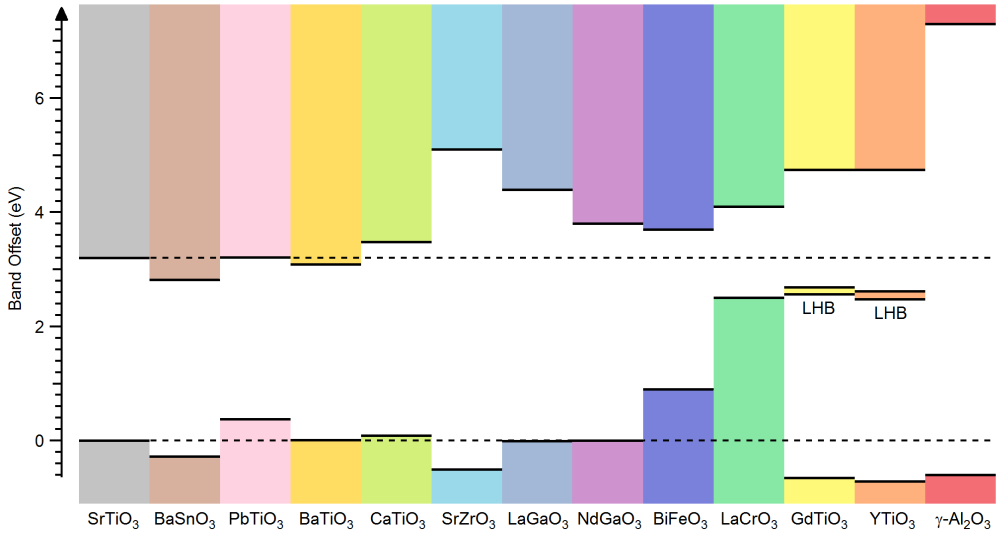

Figure 1.9: Band alignment between various oxide materials and $SrTiO_3$ as reported by several authors. Most of the heterostructures display a Type II band alignment. The authors of the different band alignments are reported in Table 1.2.

Though the formation of a 2DEG at the $ABO_3/SrTiO_3$ interface cannot be discriminated just with the band alignment analysis alone, this analysis is important to predict on which side of the junction the possible 2DEG will be confined. The level of charge confinement can also be directly evaluated, since a larger conduction band offset induces a better carrier confinement [7]. For example, in the study of Comes et al. [36] the band offsets between the alloy perovskite $(LaAlO_3)_{0.3}$-$(Sr_2AlTaO_6)_{0.7}$ (LSAT) and STO is discussed. The large conduction band offset between STO and LSAT clearly demonstrates that for any STO-based heterostructures grown on LSAT, electrons will not diffuse into the LSAT, and a band bending is excluded by a Ti 2p line shape analysis. The conduction band offset is between 2.4 and 2.8 eV, thus any itinerant electron in the system will be confined to the STO and any electronic contributions from the LSAT can be safely discounted.

The 2DEG was also found at the heterojunction between $SrTiO_3$ and many other perovskite material, such as $LaTiO_3$ [88], $LaVO_3$ [88], $PrAlO_3$ [89], $NdAlO_3$ [89], $YAlO_3$ [90], $DyScO_3$ [91], $KTaO_3$ [92] and $CaZrO_3$ [93]. Other similar studies report an insulating interface for $LaMnO_3$ [92], $LaYO_3$ [90], $BiMnO_3$ [94], and non-perovskitic La_2O_3 [90] and

Material	Authors	VBO (± 0.2 eV)	2DEG
$BaSnO_3$	Chambers *et al.* [7]	-0.30	-
$PbTiO_3$	Lebedev *et al.* [55]	0.38*	Yes [84]
$BaTiO_3$	Lebedev *et al.* [55]	0.01*	-
$CaTiO_3$	Lebedev *et al.* [55]	0.09*	-
$SrZrO_3$	Schafranek *et al.* [46]	-0.50	Yes [85]
$LaGaO_3$	Treske *et al.* [4]	0.00	Yes [4]
$NdGaO_3$	Treske *et al.* [4]	0.00	Yes [4]
$BiFeO_3$	Schafranek *et al.* [86]	0.90	Yes [87]
$LaCrO_3$	Chambers *et al.* [82]	2.50	No [82]
$GdTiO_3$	Janotti *et al.* [6]	2.69*	Yes [83]
$YTiO_3$	Janotti *et al.* [6]	2.61*	Yes [6]
γ-Al_2O_3	Schütz *et al.* [9]	-0.60	Yes [9]

Table 1.2: Band alignment results between various oxide materials and $SrTiO_3$ as reported by several authors. The band alignments obtained through calculations are marked with a *. The presence of a two-dimensional electron gas at the interface, whenever discussed, is also reported.

Y_2O_3 [90] upper layers. Unfortunately for these systems an accurate band alignment is still lacking in literature, and therefore they cannot be further considered in this review of band alignment.

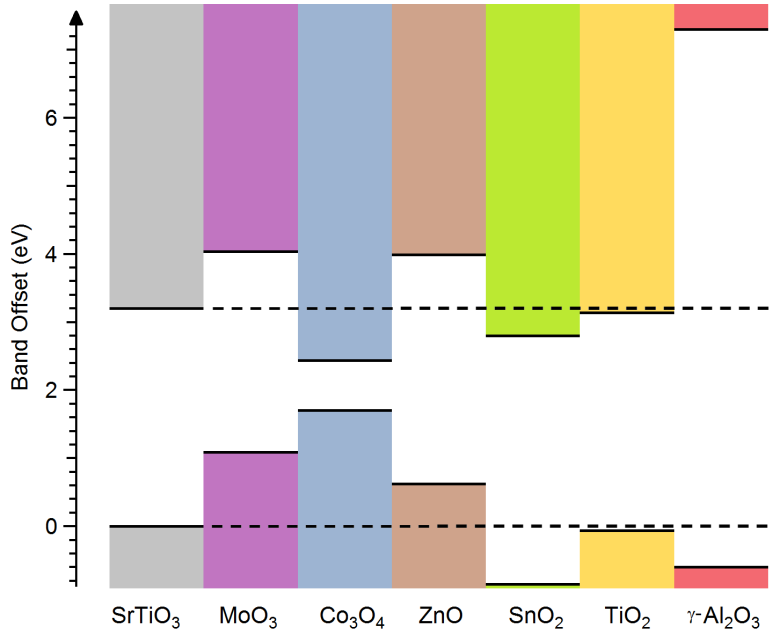

Figure 1.10: Band alignment between various non-perovskitic oxide materials and $SrTiO_3$ as reported by several authors. The authors of the different band alignments are reported in Table 1.3.

1.5 Beyond all-perovskite junctions

It is interesting to observe that the 2DEG physics in LAO-STO has triggered several studies where the top-most layer is not a perovskite (Figure 1.10, Table 1.3). In addition to the γ-Al_2O_3, a recent study has presented the possibility to grow MoO_3 on STO, where remarkable effects of charge transfer have been evidenced due to the large work function difference between $SrTiO_3$ and MoO_3 [95]. An unexpected type I band alignment was instead detected at the interface between Co_3O_4 and $SrTiO_3$, where the simultaneous confinement of holes and electrons in the Co_3O_4 layer allows the use of the heterostructure in luminescence and optoelectronic devices [20]. Other interfaces have also been studied, such as the ZnO/$SrTiO_3$ (type I) [27] and SnO_2/$SrTiO_3$ (type II) [96].

Material	Authors	VBO ($\pm$ 0.2 eV)
MoO_3	Du *et al.* [95]	1.08
Co_3O_4	Qiao *et al.* [20]	1.7
ZnO	Lallart *et al.* [27]	0.62
SnO_2	Ke *et al.* [96]	-0.85
TiO_2	Chambers *et al.* [97]	-0.06
γ-Al_2O_3	Schütz *et al.* [9]	-0.60

Table 1.3: Band alignment results between various non-perovskitic oxide materials and $SrTiO_3$ as reported by several authors.

These studies show that thinking beyond all-perovskite heterointerfaces can bring new suggestions to tailor the band gap alignment in all-oxide heterojunctions. The main field of inspiration can be all-oxide photovoltaics and photocatalysis.

All-oxide photovoltaics strongly relies on the capability to control and engineer the band gap alignment, as the performance of an all-oxide heterojunction solar cell is greatly affected by the band alignment at the heterointerface. To understand the charge transport in the device, the band alignment at the junction between the two constituent materials is thus of crucial importance.

The band alignment in this case is often studied by the analysis of ultra-violet photoemission spectroscopy (UPS) data, an experimental technique commonly used for the characterization of photovoltaic devices. In contrast, quite few papers have been reported on the study of band alignment by UPS in LAO/STO and related materials. The main difficulty for this materials is represented by the strong charging effects, as discussed by Siemons *et al.* [98], where the authors resorted to use Nb:STO substrates to overcome charging effects.

One of the most interesting oxide materials for all-oxide photovoltaics is the cuprous oxide (Cu_2O). Cu_2O-based photovoltaic devices are however characterized by a low open circuit voltage, and this underperformance is mainly due to the excessive conduction band offset between Cu_2O and the n-type material partner chosen for the heterojunction. For instance, the TiO_2/Cu_2O junction has a large (up to 1.4eV) conduction band offset which causes a loss in photovoltage [99]. A promising material to replace TiO_2 in the heterojunction is Ga_2O_3, which offers a small conduction band offset and thus reduces recombination phenomena at the interface [33]. This band alignment brought to the record in open circuit voltage for Cu_2O-based cells [2] [39].

An accurate band alignment scheme between Cu_2O and $SrTiO_3$ is still lacking in literature, albeit the formation of the heterojunction is supposed to change the valence band offset and improve the separation of photogenerate charge carriers [100]. Indeed, the band alignment at the Cu_2O/$SrTiO_3$ interface should trigger improved properties re-

spect to other Cu_2O-based devices, such as enhanced photoelectrochemical water splitting performance [100] and photocatalytic activity [101].

In heterojunctions with a type II (staggered) band alignment an accurate control of the separation and transport of photoexcited charge through the interface is possible. Here, the driving force for carrier migration is provided by the electric potential. An interesting phenomena related to this situation is the enhanced photocatalytic activity detected in the mixed-phase of anatase and rutile TiO_2 with respect to the pristine separated materials [3]. This effect is probably due to charge migration, whose direction is however highly debated [102]: many works suggest that the electrons flow from rutile to anatase [103] or anatase to rutile [104]. The charge transfer direction is strictly related to the sign of the valence band offset at the interface (Figure 1.11). Indeed, the bandgaps of rutile and anatase TiO_2 are 3.03 and 3.20 eV, respectively, and a type II band alignment is usually claimed [105]. When the VBO between rutile and anatase is positive the alignment would favor the migration of photogenerated electrons from the anatase side of the junction to rutile, and the transport of holes from rutile to anatase [106]. Alternatively, other photoemission studies have reported the opposite situation, placing the conduction band minimum of anatase below that of rutile [107]. Kullgren et al. [108] tried to explain this inconsistency through a band offset induced by OH^-/H^+ molecules adsorbed on the surface. This open debate however demonstrates that the current band alignment models at the junction between rutile and anatase needs to be improved in order to fully explain the bidirectional migration observed for electrons.

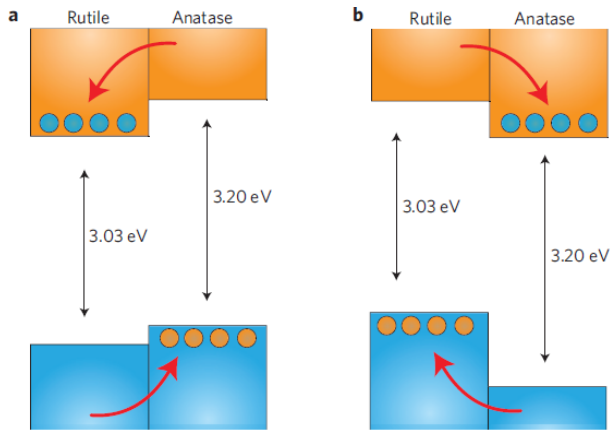

Figure 1.11: Two proposed valence and conduction band alignment mechanisms for the anatase/rutile interface. (a) Type-II (rutile). (b) Type-II (anatase). Red arrows indicate the flow of electrons (holes) in the conduction band (valence band). Blue and orange dots represent electrons and holes, respectively. Adapted from [105].

In $SrTiO_3$-based heterojunctions the conductive phase formation is strictly related to the presence of a TiO_2 termination plane, and thus the STO-anatase band offset is a critical factor for the determination of the heterostructure properties. This band offset is discussed in the work of Chambers *et al.* [97], where various sample were obtained through different preparation methods, and where a band offset ranging between -0.06 ± 0.05 and $+0.16 \pm 0.05$ eV is reported. In this case the two materials display the same band gap and a near aligned band structure, so electrons and holes are unlikely to become confined in the STO substrate and don't contribute to surface photocatalytic processes.

CHAPTER 2

Experimental details

2.1 Sputtering deposition

2.1.1 Sputtering process bases

The sputter deposition is a physical vapor deposition method which is widely used in industrial application, due to the low production costs, reproducible and fast growth (with a typical growth rate of 1-10 $Å s^{-1}$ [109]) of large-area thin films. With a proper setup and deposition geometry calibration, sputtering can produce high-quality epitaxial films, often at a lower cost than other growth techniques [12].

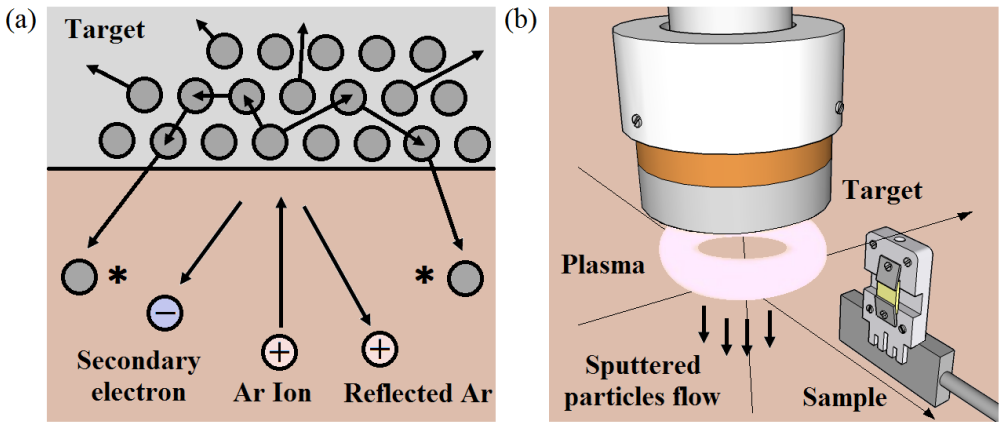

Figure 2.1: (a) Schematic representation of the sputtering process, along with the parallel emission of secondary electrons from the sample surface. Sputtered particles are marked with a *. (b) Schematic representation of the geometry employed in off-axis sputtering deposition.

The sputtering is a process which occurs whenever a particle strikes a material with enough energy to remove an atom from the surface (Fig. 2.1 (a)). The incident particles are generally ions because they can be accelerated towards the material by an electrical potential. Usually argon ion gas is used as the sputtering medium, since it's a plentiful heavy rare gas with a low ionization potential. The inert nature of argon also inhibits compounds from being formed at the sputtered surface. In sputtering deposition the Ar^+ ions are accelerated towards a cathode (target) representing the source of coating material, and the accumulation of atoms which are blasted off the target onto a nearby substrate induces the film growth.

An electrical potential is thus applied between the target (cathode) and the anode, and this generates a low pressure glow discharge (plasma) between the electrodes. A grounded cylindrical protecting shield, placed around the target material, is used to prevent a discharge formation in undesirable areas. A continuous flow of ions collected from the plasma must be guaranteed in order to sustain the discharge. Luckily sputtering deposition is also characterized by a generation of secondary electrons due to the collision of ions on the target surface. These secondary electrons are accelerated by the cathode potential, and ionize gas atoms within the plasma, producing thus the additional ion flow necessary to maintain the discharge active [110].

2.1.2 Sputtering of oxide materials: RF sputtering

When the sputtering target is an insulator, the sputtering process induced by the argon ions results in an accumulation of positive charge on the target surface. This charge may grow to the point that the bombarding ions are repelled and the sputtering process will stop. In order to make the process continue the polarity of the target must be reversed to attract enough electrons from the discharge to eliminate the surface charge. In order to attract the electrons and not repel the ions necessary for sputtering, the frequency must be high enough to reverse before the direction of the ions are affected. Usually a radiofrequency (RF) source with a frequency of 13.56 MHz is used, a band assigned to industrial production by the Federal Communications Commission [110]. In this frequency region the electrons are effectively attracted to the target following the electric field switching, whereas the ions (which have an higher mass than the electrons) are only affected to the time-averaged field.

The main disadvantages of RF sputtering are the need for electromagnetic shields, necessary to block the RF radiation propagation in undesirable areas, and the requirement of a complex matching network. RF power supplies are indeed designed to drive a load of a given impedance, which usually don't match with the one characteristic of the sputtering plasma. Therefore, a matching network with variable capacitors is necessary to tune the overall impedance of the system, which thus becomes equivalent to the driving source impedance [12].

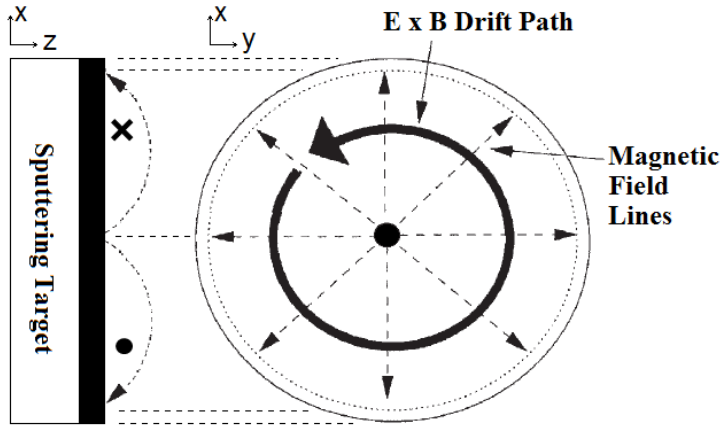

Figure 2.2: Schematic representation of the magnetic field orientation in a circular planar magnetron cathode. Adapted from [111].

In order to enhance further the efficiency of the RF sputtering system a magnetron can be used. The magnetron generates a static magnetic field parallel to the target surface to force the secondary electrons to flow in a direction perpendicular to both the magnetic field and the electric field, which is normal to the surface. By tuning the magnetic field this $E \times B$ drift can become closed on itself, and the resulting current loop confines secondary electrons in a ring shape (Fig. 2.2) [111]. This configuration enhance the number of ionizing collisions for each electron in the plasma [110], and the collision of secondary electrons with other gas atoms or electrons reduces their kinetic energy, increasing the density of the plasma in the ring-shaped region [111]. The introduction of a magnetron system enhances the deposition rates (10 times the DC diode) with less substrate heating, due to a lowered substrate electron bombardment [110].

2.1.3 Parameters influencing the sample quality

The quality of the thin films grown by sputtering deposition is strictly dependent on many parameters which can be established in the deposition, and a small variation of one of these parameters can greatly alter the final properties of the grown sample, in terms of crystallinity, chemical composition (due to the possible formation of secondary phases) and eventually magnetic and electric properties. In the following sections, the parameters chosen for the achievement of high quality thin films are discussed.

Sputtering power

The sputtering power directly determines the sputtering rate; indeed at very low incident ion energies (up to 30 eV) there is very little sputtering, and with an excessive energy (more than 50 keV) many ions become trapped or implanted within a damaged target. In order to obtain high quality thin films the knock-on energy regime (40 to 1000 eV) is desirable, since this ion energy range supports the dislodge of hundreds of atoms and favors erratic collisions, which improve the sputtering rate.

Target considerations

In certain cases volatile elements can be present in the sputtered species (such as Bi in the $BiFeO_3$ material) and in order to achieve a stoichiometric film growth it is necessary to use non-stoichiometric targets (with excess of Bi, $Bi_{1.1}FeO_3$). The target used in sputtering deposition must be as dense as possible in order to avoid the ejection of large particles, which can produce inhomogeneous films. The heat produced in the target during the deposition is generally dissipated through the bonding with a water-cooled copper plate [110].

Background gas pressure

For the purpose of ensure the flow of sputtered particles from the target to the substrate and in order to maintain the discharge, the deposition chamber must be evacuated at an operating pressure of $10^{-2} - 10^{-3}$ mbar. The gas pressure must be low enough to avoid chemical reactions between low level contaminants present in the deposition chamber (water vapours, oxygen, nitrogen, ...) and the sputtered atoms in transit from the target to the substrate, which would produce secondary phases or impurity inclusions [111].

Substrate heating

Most oxide materials display growth modes that are extremely dependent on the deposition temperature. The heating of a substrate in sputtering deposition can be achieved in different ways, such as the use of resistive block heaters, where the temperature is transmitted by thermal contact between the heater and a directly connected substrate. In radiative heating, instead, the substrate is heated by radiation produced by a heating element placed at a certain distance from the substrate.

Sputtering geometry

In order to obtain high-quality epitaxial thin films, is usually necessary to deal with an off-axis geometry, where the substrate is placed 5-20 cm back from the central axis of the chamber (Fig. 2.1 (b)), with the sputtered particles main direction orthogonal to the plane of the substrate. The main advantage for the use of an off-axis deposition geometry is to reduce resputtering mechanism, which occurs when already deposited material is ejected from the growing film because of the collision with energetic sputtered particles. Indeed, in off-axis geometry only thermalized atoms with an uniform energy distribution can be deposited on the substrate, because these particles are subjected to many collisions with other sputtered particles before the interaction with the substrate (which is placed out of the main stream). As a consequence, a more homogeneous film is obtained [12].

2.2 Atomic force microscopy

2.2.1 Introduction

The Atomic Force Microscopy (AFM) technique allows the measurement of the surface topography of a sample, evaluated from the variation in interaction forces between the sample surface and a tip placed on a flexible cantilever (Figure 2.3). Variations in the surface topography of the sample lead to a deflection of the cantilever, thus producing a variation in the reflection of a laser beam which hits the cantilever upper side. The changes in the reflected laser beam positions are measured by a four-quadrant photodiode, and could thus indirectly probe the variations in the sample topography. However, in common AFM analysis, a feedback control unit keeps a constant cantilever deflection, obtaining an image with constant interaction force. The variation in the force while scanning leads to changes in the tip-sample distance, providing the topography. The tip-sample distance is thus a critical factor, and a vibration isolation system should be implemented in the experimental setup. In this technique the vertical deflection resolution is on the order of fractions of a nanometer, thus allowing the detection of surface steps with the height of one atom [112]. The lateral resolution of few nanometers characteristic of this technique enables the detection of features in all three dimensions. A small area of the sample surface can be raster scanned through changes in the deformation of a piezoelectric material placed under the sample holder. Different piezos are commercially available with different possible xy scan areas (ranging between $1\mu m \times 1\mu m$ and $200\mu m \times 200\mu m$) and z ranges (with a maximum of $15\mu m$) [113].

The AFM setup can be employed in two different main operation modes, depending on the distance between the AFM tip and the sample: contact mode and non-contact (or oscillatory) mode. In contact mode the tip is in direct mechanical contact with the sample surface thus providing highest sensitivity achievable in AFM, with the drawback of possible tips breakage and sample damages, especially in fragile specimens such as organic

and biological samples. In non-contact mode the sensitivity can be improved through the so-called semi-contact mode (or tapping mode), where the cantilever oscillations are forced with a resonance frequency characterized by an amplitude of 10-100 nm. In this way the tip gets periodically in contact with the sample surface throughout the lower semioscillation [114].

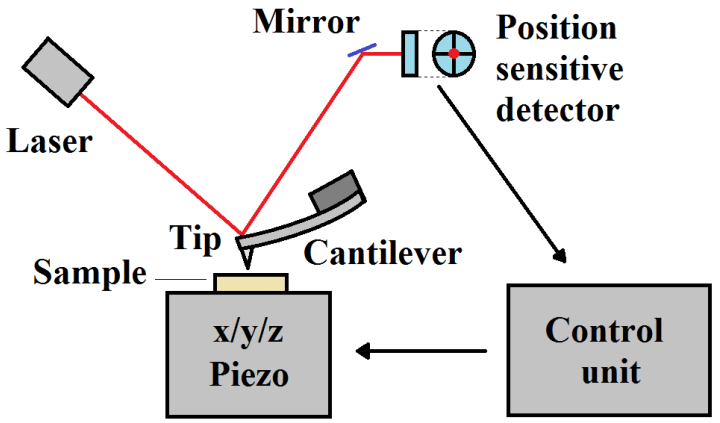

Figure 2.3: Schematic representation of the atomic force microscopy setup.

The tip-sample interaction forces are mainly due to Van Der Waals, electrostatic, hydrophobic, hydrophilic, and capillary effects [113]. The sum of this forces is described by the Lennard-Jones potential, with its characteristic jump-to-contact which happens when the attractive forces (at large tip-sample distances) become repulsive (at small distances) [114]. The interaction is strictly dependent on the tip shape, which is multiatomic at its apex (with a curvature radius ranging between 1 and 50 nm), and should be as sharp as possible in order to avoid artifact signals originating from the convolution with the tip shape.

One of the main advantage of atomic force microscopy is that a vacuum environment is not necessary, thus AFM measurements are usually carried out in air, and good images can be achieved also in water or other liquids. Very little sample preparation is thus needed. The main drawbacks are that scans can be slow (on the order of ten minutes) and the possible contamination-induced tip wear, which changes the surface interaction.

2.2.2 Piezoresponse force microscopy

Piezoresponse Force Microscopy (PFM) is an upgrade of the atomic force microscopy technique [115], which enables the detection of the local piezoelectric deformation in a sample surface caused by an applied electric field. PFM is a versatile, easy-to-handle, non-invasive method for the detection and imaging of piezoelectric and ferroelectric domain patterns in air environment with a lateral resolution of a few nanometers [116] and without the necessity of an accurate sample preparation.

In a piezoelectric material (Figure 2.4 (a)) a surface polarization charge arises as a consequence of an applied external mechanical strain and vice versa, while in a ferroelectric material (Figure 2.4 (b)) the spontaneous polarization can be switched and reversed through the application of an external electric field [117], in the form of an hysteresis

loop. All ferroelectrics are also piezoelectric: when an electric field is applied to a ferroelectric material, the material expands if the electric field is parallel to the material's polarization, and contracts if anti-parallel. PFM can be then used for imaging ferroelectric domain patterns if an hysteresis loop is recorded on a specific piezoelectric domain [118]. The shape of the hysteresis loop signal is however highly affected by artifacts which originate from surface charge injection and current flow [119], and these phenomena must be considered in order to prevent the detection of artifact ferroelectric signal in non-ferroelectric and non-piezoelectric materials.

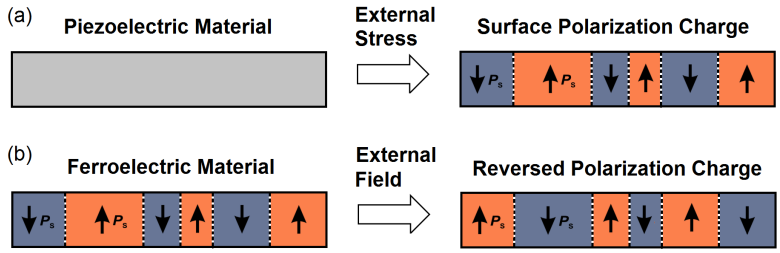

Figure 2.4: Schematic representation of the difference between a piezoelectric and a ferroelectric material.

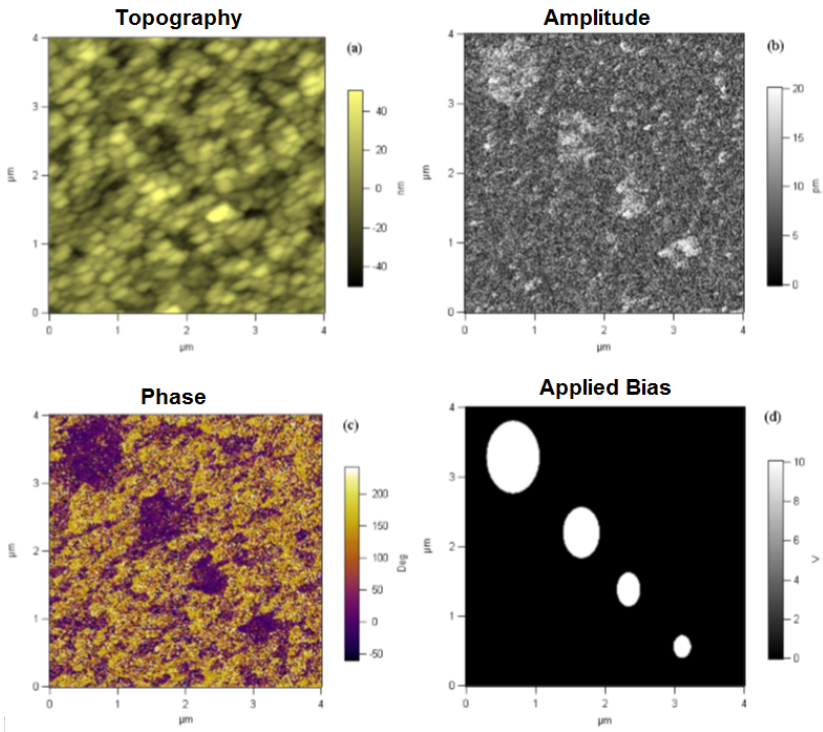

Figure 2.5: (a) AFM topography image of a $BiFeO_3$ thin film. (b) PFM magnitude. (c) PFM phase. (d) scheme of the applied bias. Each picture covers $4\mu m \times 4\mu m$. Adapted from [120].

The PFM experimental setup is an AFM system upgraded for the PFM operation with the introduction of a function generator and a lock-in amplifier [115]. An alternating voltage, with amplitude V and frequency f, is applied to the tip by the function generator and the consequent oscillations of the cantilever are read through the lock-in amplifier. A simultaneous topography acquisition is also feasible, with the drawback of possible residual topographic features in PFM data. Indeed variations in tip-sample contact stiffness during the topographic scan induce variations in the AFM cantilever resonance, and thus can generate artifact features in PFM contrast. The cross-talk between piezoelectric and topographic signals can be prevented through the use of a low pass filter, typically placed in front of the feedback [121].

The theory at the base of PFM is very simple [122]: the strain S_j developed in a piezoelectric material by an applied electric field E_i is described by a simple equation: $S_j = d_{ij}E_i$, where d_{ij} are components of the piezoelectric tensor (with the unit of m/V). The longitudinal piezoelectric constant, d_{33}, is determined in PFM by measuring the displacement (Δz) of the sample along the applied field (E_3). Indeed $\Delta z = d_{33}V$, assuming as approximations $S_3 = \Delta z/z_0$ and $E_3 = V/z_0$, where V is the applied voltage and z_0 is the thickness of the sample. Furthermore, the detection of the PFM signal needs an alternate voltage $V = V_{AC}cos(\omega t)$ applied to the tip, so: $\Delta z = d_{33}V_{AC}cos(\omega t + \theta)$, and the longitudinal piezoelectric constant d_{33} is readily determined. The quantities evaluated in PFM analysis are thus the magnitude and the phase of the piezoelectric response, which provide information about the intensity of the deformation and the orientation of the piezoelectric domains respectively.

In PFM-based lithography [120] is also possible to produce sub-μm sized domains on the surface of a ferroelectric material using the AFM tip as an electrode (Figure 2.5). Several experiments on PFM-based lithography have been performed, where the formation of domains is demonstrated for samples thickness ranging from a few 10nm (thin films) to 1mm (bulk samples).

2.3 Photoelectron spectroscopy techniques

2.3.1 X-ray photoelectron spectroscopy

The X-ray Photoelectron Spectroscopy (XPS) technique is based on the interaction between a sample and a X-ray beam, which results in the emission of electrons from the surface of the sample. The emitted electrons then pass through transfer lenses, are collected by an analyzer and finally the electron kinetic energy is measured by a detector (Figure 2.6 (a)). In this work, an hemispherical deflection analyzer is used and photoelectrons are subjected to a pre-retardation stage, which decelerate all electrons to a given kinetic energy (called pass energy) prior to the entrance into the analyzer [123]. Indeed within the analyzer photoelectrons are deflected by the potential difference applied to the concentric capacitors, and only the electrons which enter the analyzer with a given kinetic energy can reach the exit slit and be measured by the detector. Furthermore, the presence of a retardation stage allows the measurements of the photoelectrons with a fixed pass energy and thus a fixed energy resolution.

However only a small portion of the electrons excited by the X-ray source are photoemitted, since inelastic scattering between the atoms of a specimen and electrons traveling from the bulk to the surface can reduce the electrons kinetic energy, which can thus be less than the energy necessary to guarantee photoemission. The mean depth of electron emission in XPS is thus as small as a few atomic layers [124], and the analysis is carried on electron emitted from the topmost 3-4 nm. Thus XPS is a surface sensitive

technique, which can be exploited for the study of the surface physical and chemical properties. In order to study the surface properties of a material, atomically clean surfaces are then needed [123]. A sample with reduced surface environmental contaminations can be obtained relying on an ultra-high vacuum environment ($p \leq 10^{-9} mbar$), which also allow the transfer of photoemitted electrons from the sample to the analyzer without collisions with gas particles present in the air. This vacuum regime can be easily obtained through a combination of rotary and turbo-molecular pumps.

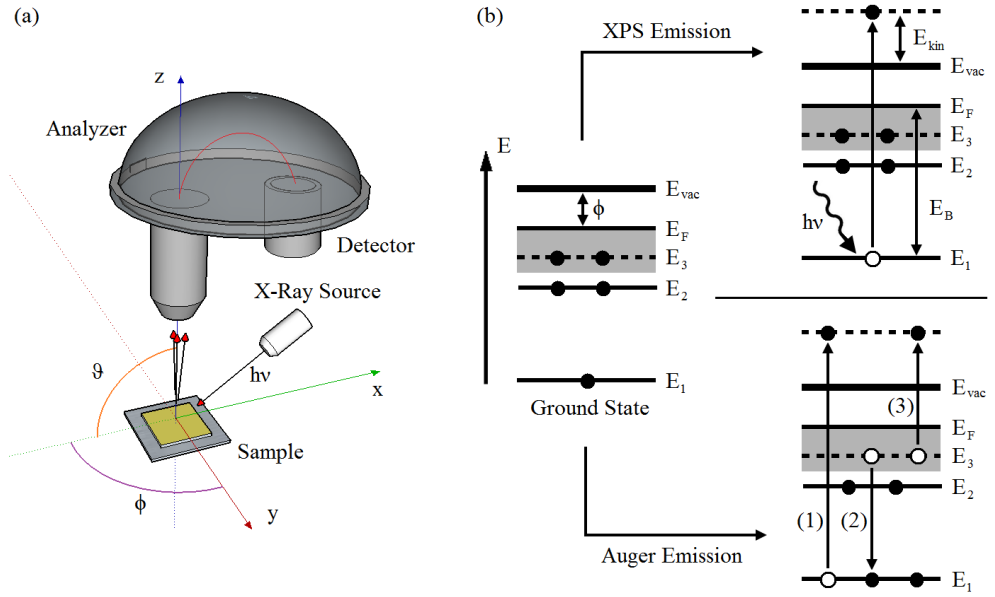

Figure 2.6: (a) Schematic representation of the experimental setup used in XPS analysis. (b) Schematic representation of the photoemission process, along with the parallel emission of Auger electrons.

The basic equation which controls the photoemission process is: $h\nu = E_b + E_{Kin} + \varphi$, thus the binding energy E_b of a photoemitted electron can be directly evaluated, as the energy of the X-ray beam ($h\nu$) is fixed, the kinetic energy of the photoelectron E_{kin} is measured by the detector and φ is a constant (Figure 2.6 (b), upper side). The φ term include the work function of the material (potential barrier which must be trespassed in order to escape the sample surface) and possible charging effects which are due to the accumulation of charge on the sample surface. The φ constant can be determined by the alignment of the position of peaks related to surface environmental contaminations, which have a fixed binding energy position and are not involved in chemical bonds. The X-ray source anodes more commonly used in XPS produce the $Al\ k_\alpha$ (1486.6 eV) and the $Mg\ k_\alpha (1253.6eV)$ lines, which enable a detailed analysis of the core levels of the sample surface.

The binding energy of a photoemission peak carries information about the specific energy level of the specific element from which the electron is photoemitted. Thus the chemical composition of the surface can be evaluated, as an accurate quantification can be obtained by the analysis of the area underlying the photoemission peaks, and the chemical bonds can be determined through the analysis of possible shifts in the peaks

positions and shape. Furthermore, the depth distribution of the elements within the material can be evaluated by the study of angle-resolved photoemission spectra. Indeed, the surface sensitivity of a photoemitted electron depends on the tilt angle θ, as the mean escape depth of emission d is given by $d = \Lambda_e sin\theta$, where Λ_e is the photoelectron inelastic mean free path characteristic of the material [124] (Figure 2.7 (a)). The intensity of a photoemission peak arising from an electron emitted at a depth z is thus determined by $I(z) = I_0 exp[-z/\Lambda_e sin\theta]$ [125]. However, it should be pointed out that the escape depth depends on the material and on the choice of the photon energy used for the photoemission process (Figure 2.7 (b)) [126].

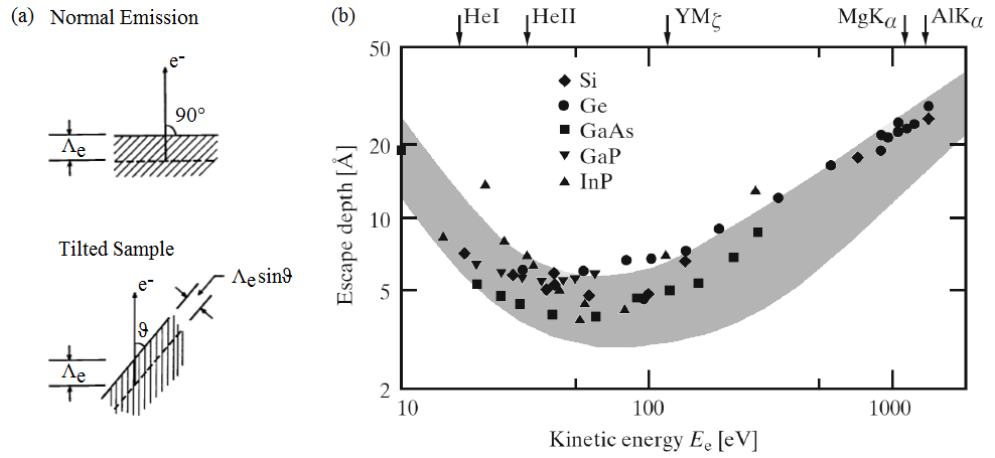

Figure 2.7: (a) Schematic representation of the variation in the emission depth with the introduction of a tilt angle. Adapted from [124]. (b) Experimental escape depth measured in various solids (dark band) and in the most common semiconductors (markers). The energy of typical laboratory sources is also specified through the upper labels. Adapted from [126].

Generally the interaction between the sample and the X-ray beam produces also secondary electrons, due to inelastic scattering processes, and Auger electrons [124]. Auger electrons are emitted when an electron vacancy within the core levels induces an electronic transition which produces the energy necessary to an additional electron emission (Figure 2.6 (b), bottom). The Auger electron energy is determined by the energy difference between the photoemission-induced core vacancy state and the two-hole state which is produced by the Auger emission [127]. Auger electrons are thus characterized by a fixed kinetic energy, which doesn't depend on the energy of the X-ray source, and are easily recognizable. The inelastic scattering of emitted electrons induce a step-like background in the resulting photoemission spectra.

2.3.2 X-ray photoelectron diffraction (XPD)

X-ray Photoelectron Diffraction (XPD, Figure 2.8 (a)) is an experimental technique which studies the angular dependence of XPS spectra. Indeed, the variation of the polar angle θ (Figure 2.8 (b)) induce changes in the intensity of the XPS peaks characteristic of an ordered crystal (Figure 2.9 (a)), since the interference between the directly emitted electron wave and the secondary electron waves which undergo scattering processes induce diffraction effects. In this way a XPD slice is obtained (Figure 2.9 (b)), and a full stere-

ographic projection (Figure 2.9 (c)) is obtained through the variation of the azimuthal angle φ. This XPD interference pattern allows the determination of the local crystalline structure around the emitter atom, since the local environment produces characteristic scattering processes and thus specific interference patterns. XPD is capable to detect features on the atomic scale, and can be used for the analysis of the long-range crystal order of the sample down to a monolayer [128]. Furthermore, XPD analysis is performed on a core level, and thus a detailed analysis of chemical bonding and crystal structure respect to a specific element is possible.

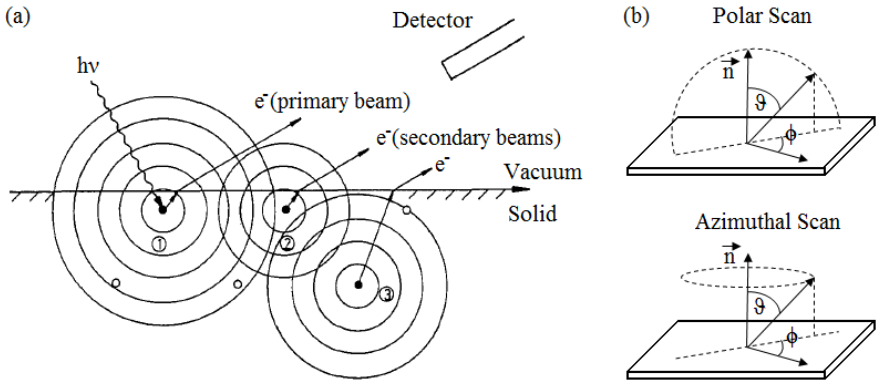

Figure 2.8: (a) Schematic representation of the interference process at the basis of XPD analysis. Adapted from [123]. (b) Geometry characteristic of polar and azimuthal scans.

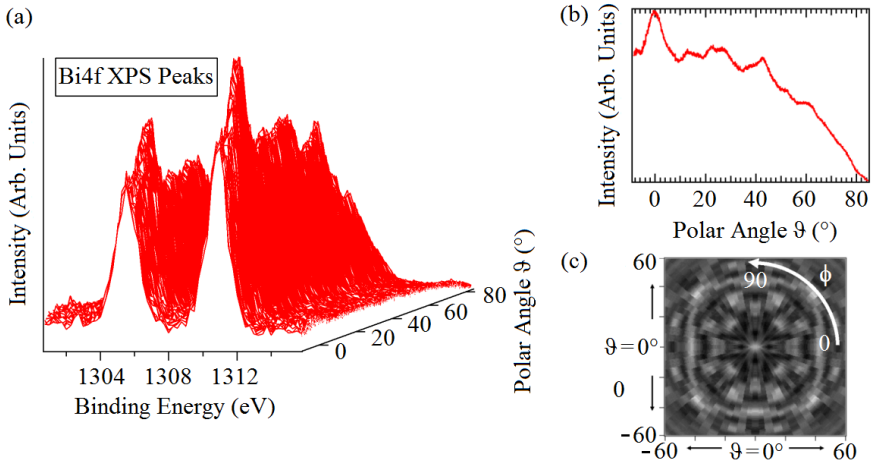

Figure 2.9: (a) XPD modulation obtained from the variation of Bi4f XPS peak intensity with the change in polar angle (azimuthal angle fixed at $\varphi = 0°$). (b) Resulting XPD slice at $\varphi = 0°$. (c) Full stereographic projection, obtained through the variation of the azimuthal angle.

In order to obtain quantitative information XPD experimental data can be compared with theoretical simulations. However single scattering calculation results usually produce an excess in forward focusing ($\theta = 0°$) intensity, due to the topmost atoms which

focus the emission in the forward scattering direction, while in the practical case the scattering arising from subsequent atoms tend to defocus the signal [128]. Thus features due to scattering phenomena from a finite cluster around the photo-electron source aren't sufficient for a complete description of the photoelectron diffraction process, and Kikuchi arches, arising from Bragg-related scattering by lattice planes of a long range periodic structure, should be also considered. The Kikuchi lines are in connection with a given low-index set of crystal planes and should be predominant for photoelectron kinetic energies larger than 1 keV, when the forward scattering process diminishes. The main XPD features are thus placed at the superposition of Kikuchi bands originating from different low-index planes of the crystal [124]. Multiple scattering calculations should thus be used in order to take into account for the large number of scattering events.

X-ray photoelectron diffraction can be employed in advanced analysis, such as the determination of the properties of adsorbates on the sample surface. Indeed with an accurate analysis the adsorbate structure, orientation and site position on the sample substrate can be determined [129]. Other applications include the study of the ferroelectric polarization state orientation in a material [130], the determination of small lattice distortions around the emitter, spin-dependent effects and magnetic dichroism [131].

2.4 Synchrotron-based techniques

Synchrotron radiation is a specific form of electromagnetic radiation which is emitted whenever a charged particle which travels at relativistic speeds is forced to follow curved trajectories by external magnetic fields. This radiation is exceptionally intense and shows an energy which ranges in the electromagnetic spectrum from the hard X-rays to infrared region.

In order to produce synchrotron radiation electrons are accelerated up to the MeV range by a linear accelerator and then up to the GeV range by a booster ring. The electrons then enter into an evacuated circular accelerator called storage ring, where they can be accelerated again by the radio frequency fields produced by RF cavities, which compensate the loss of energy due to the radiation emission. In this way a stationary circular trajectory is obtained and the synchrotron radiation is produced by insertion devices, such as wigglers or undulators. The insertion devices consist of a periodic structure of magnets with alternate poles, which force electrons to oscillate perpendicularly respect to the circular trajectory, emitting synchrotron radiation in the process. The bending radius and number of magnets determine the intensity and the brightness of the emitted radiation [132].

Synchrotron radiation shows many peculiar properties: high intensity, a narrow angular collimation, high polarization, brightness and collimation. In particular, the possibility to tune the beam energy over a continuous spectral range allows the use of the radiation for interesting experimental techniques, such as resonant photoemission, X-ray absorption and dichroism.

2.4.1 Resonant photoemission

The resonant photoemission process is characterized by an intensity enhancement of photoemission peaks with the variation of the photon energy.

Resonant photoemission is based on the interaction between direct photoemission (Figure 2.10 (a)) and parallel phenomena where the excitation of intermediate core states and the subsequent decay by autoionization processes produce a final state identical to

the one obtained by direct photoemission [127]. Indeed the absorption of X-ray radiation can excite an electron to the resonant bound state (Figure 2.10 (b)), leaving the system charge neutral until an Auger-like deexcitation transition induce the emission of the electron previously excited (Figure 2.10 (c)). Thus a single valence vacancy is obtained, and this electronic state shows an energy equivalent to the one observed in the direct photoemission of a valence electron [133]. The resonant photoemission signal is mainly due to the interference between the direct photoemission and the core-hole assisted transition, and this interference induces a variation in the spectra intensities with the change in photon energy, which is characterized by Fano-like profiles [134].

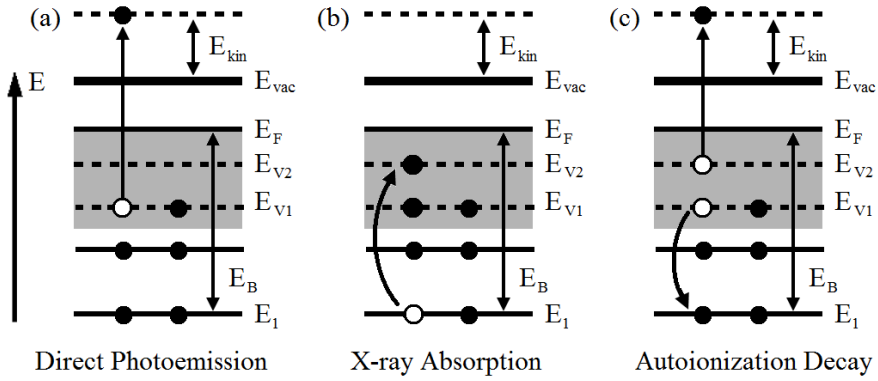

Figure 2.10: Schematic representation of: (a) direct XPS photoemission, (b) X-ray absorption, (c) autoionization decay. The interference between the two equivalent final states produces the resonant photoemission signal.

Symmetry selection rules are at the basis of this process, which can thus be used to determine the symmetry properties of the analyzed electronic states [127]. Resonant photoemission can be employed for the study of the atomic origin and symmetry of valence electron states, for the identification of the orbital symmetries, and for the analysis of possible dynamic properties [127].

2.4.2 X-ray absorption spectroscopy

When X-rays of intensity I_0 interact with a sample, a certain part of the intensity is absorbed depending on the sample thickness d and the energy E of the incident photons. The transmitted intensity I_t is determined by the Beer's law: $I_t(d) = I_0 e^{-\mu(E)d}$ and the X-ray absorption coefficient $\mu(E)$ is determined by $\mu(E) \approx \rho Z^4/mE^3$, where ρ, Z and m are the density, the atomic number and the mass of the material, respectively. The absorption coefficient thus decreases when the photon energy increases, however when the photon energy is sufficient to photoemit an electron a new photon channel is available and the absorption coefficient drastically increases [135]. This sharp element specific transition is called absorption edge and when the photon energy is increased further the absorption coefficient start to decrease again until a new absorption edge is reached. The X-ray absorption signal can be measured through the analysis of the transmitted intensity; however when the sample transmission is large or when the total absorption is only slightly influenced by the signal of interest, the absorption coefficient can be measured by fluorescence processes [136].

The absorption of X-ray photons by a material induces an excitation of electrons in unoccupied bound states (Figure 2.11 (a)), and photoemission arises when the energy exceeds a certain threshold. The absorption coefficient is thus increased for particular photon energies which correspond to the difference in energy between the starting core level and the excited electronic state [135]. Different absorption edge are associated with different atoms within the studied material, and to an excitation transition into an unoccupied electronic level. The nomenclature of x-ray absorption edge is therefore related to the core orbital of origin (Figure 2.11 (b)), where K edges refers to excitation which originate from the innermost 1s electron, while L edge refers to transitions from 1s and 2p core levels (L_1 and $L_{2,3}$ respectively) and the M edge is associated to excitations from 3s and 3p states (M_1 and $M_{2,3}$ respectively) [137].

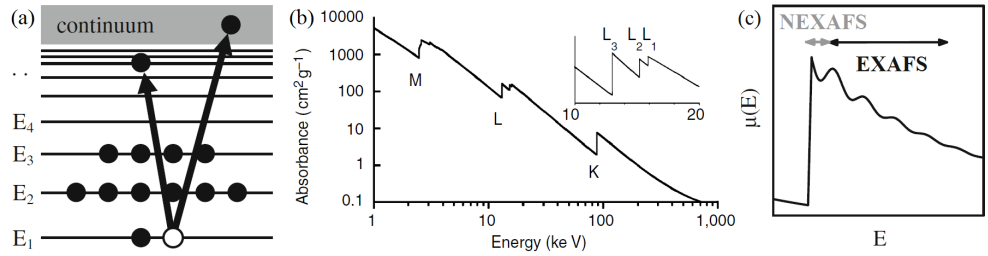

Figure 2.11: (a) Schematic representation of the absorption process. (b) Low-resolution XAS spectrum for Pb, where the three major transitions (K, L, and M edges) can be recognized. Inset: higher resolution showing the split in the L edge. Adapted from [136]. (c) Position of the NEXAFS and EXAFS regions. Adapted from [135].

The electrons photoemitted due to the interaction with the X-ray beam are associated to a wave which is scattered by the atoms present in the material under study. The quantum-interference between the directly emitted and the scattered waves produces the fine structure of the absorption coefficient, since this interference varies with photon energy [137]. The absorption spectrum can be separated into two regions: the near edge X-ray absorption fine structure (NEXAFS) and the extended X-ray absorption fine structure (EXAFS) regions (Figure 2.11 (c)). The NEXAFS region is also called X-ray absorption near edge structure (XANES) and features due to the transition into unoccupied electronic states are located in this region, so the chemical bonding can be easily studied in NEXAFS analysis [138]. Furthermore, the sensitivity on multiple scattering effects allow the analysis of the crystal phase of the sample [139]. Differently, in the EXAFS region ($E \geq 30eV$) the electrons are excited into a continuum state, which is related on the displacement of atoms around the absorption site, and is no long dependent on the chemical bonding. Thus in EXAFS analysis a study of the coordination number, distances between constituent atoms and disorder induced by structural displacement and thermal variations can be performed [137].

2.4.3 X-ray dichroism

A dichroism effect happens when a variation in X-ray absorption spectral features intensity is observed with the change in the polarization of the incident radiation. If these effects are obtained employing linearly polarized radiation, a X-ray linear dichroism (XLD) signal is achieved (Figure 2.12 (a)), while if a magnetic field is applied to the sam-

ple and the radiation is circularly polarized a X-ray magnetic circular dichroism (XMCD) is obtained (Figure 2.12 (c)).

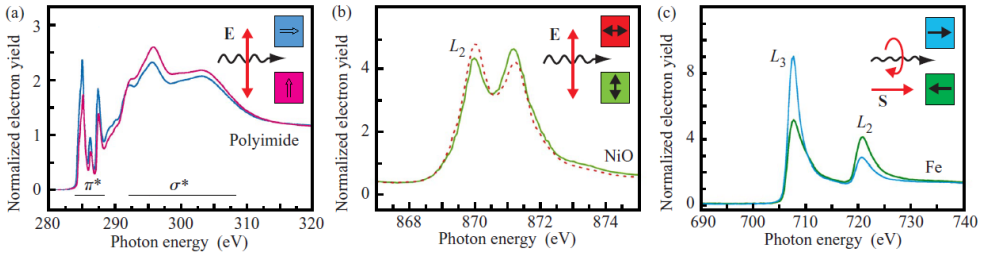

Figure 2.12: (a) X-ray linear dichroism (XLD) arising from the differential bond orientation in polyimide films respect to the electric field of incident radiation. (b) X-ray magnetic linear dichroism (XMLD) due to differential orientation in the antiferromagnetic axis of NiO(100) films respect to the electric field of incident radiation. (c) X-ray magnetic circular dichroism (XMCD) arising from the magnetic moment unidirectional orientation in a Fe metal sample respect to the photon helicity. Adapted from [140].

The use of circularly polarized radiation allows a spin-dependent analysis of X-ray absorption data, because the angular momentum of circularly polarized photons can be transferred to the emitted photoelectrons. In this way the magnetic moment can be evaluated by measuring the difference in the number of d holes characterized by up and down spin, as in most of the ferromagnets (such as Fe, Co and Ni) the magnetic behavior is determined by the properties of d valence electrons [141] and by the imbalance between spin-up and spin-down holes. The maximum effect is obtained for parallel and antiparallel direction between spin and magnetization [140].

Circularly polarized X-rays are particularly incisive for the analysis of materials with a net magnetic moment, such as ferromagnets or ferrimagnets [140]. In XMCD analysis the direction of the magnetic moment can be studied exploiting the angular dependence of this technique, since the intensity of the signal is proportional to $K \cdot M$, where K is the propagation vector of X-ray radiation [142]. The size of atomic magnetic moments and the possible anisotropies in charge, spin and angular momentum can also be studied by XMCD [143].

X-ray linear dichroism can instead be used for the analysis of the orientation of molecular orbitals, and thus of the chemical bonds properties. Linear dichroism obtained from X-ray absorption data can also be used for the analysis of the orbital occupancy difference between the t_{2g} and e_g orbitals. Furthermore it has been demonstrated that in LSMO thin films tensile strain favors the occupancy of $x^2 - y^2$ orbitals, while a compressive strain favors the occupancy of $3z^2 - r^2$ orbitals, thus XLD can be used for the analysis of stress phenomena at the surface of a sample [144].

In a sample with no net magnetic moment (spin up and spin down equally present), the local atomic spins can align along a preferential magnetic axis creating a magnetic anisotropy, which can be probed by X-ray magnetic linear dichroism (XMLD) (Figure 2.12 (b)). A XMLD study can thus be really a powerful tool for the analysis of antiferromagnets [145]. XMCD and XLD techniques sensitivity allow the analysis of single interfaces [146], and the high sensitivity of XMCD allow the detection of very small magnetic moments ($\approx 0.005 \mu_B/atom$) [142].

CHAPTER 3

Strontium titanate

3.1 Introduction

Strontium titanate ($SrTiO_3$ or STO) is a model perovskite oxide with a large impact in science and technological application. STO exhibits lots of interesting properties ranging from being a paraelectric insulator [147] to a ferroelectric induced by epitaxial strain [148] to a metal [149] or even to a superconductor if suitably doped [150]; moreover, it is one of the most common substrates for epitaxial oxides growth and thus can be used as a substrate for complex heterojunctions systems [81] [151]. Other interesting applications of STO include the use as insulating layer in random-access memories [152], gate oxide [153], immobilization material of nuclear waste [154], catalyst for the photoelectrolysis of water [155] and electrode in oxide fuel cells [156]. The recent possibility to grow STO epitaxially on Si (100) [157] enables the production of FETs with STO gate oxides, which can thus introduce ferroelectric, superconducting, or magnetoresistive properties in these devices.

When the STO is used as a substrate for the deposition of thin films an accurate substrate termination is needed, since commercially available STO substrates usually display a mixed SrO and TiO_2 termination. A TiO_2 termination is needed in order to induce the insulator to metal transition at the $LaAlO_3/SrTiO_3$ interface [64], and the resulting step-like morphology favors an homogeneous epitaxial growth of the thin films.

STO transport properties are tightly bound to the presence of defects, oxygen vacancies and to external mechanism, such as elemental doping, light exposure and interface effects. In $SrTiO_3$ single crystals, oxygen vacancies are the main defects and locate mainly at surface, while Ti interstitials are the minor defects and locate in the bulk [158]. There are three main ways to create oxygen deficient STO: by annealing at high temperature (600-1400°C) in vacuum [159] [160], by Ar-ion bombardment [161] [162], and through the deposition of inherently oxygen reduced thin films, such as $LaAlO_3$ (LAO) films [66]. Vacuum annealing at 650°C induce an oxygen vacancy density increase near the surface and a reduction of Ti interstitials density in bulk [158].

The oxygen vacancies defects are well known to influence greatly the electrical properties of STO, changing the insulating behavior of stoichiometric STO into a n-type conductor for oxygen vacancies concentrations exceeding 10^{15} cm^{-3} [162]. These vacancies are believed to act like donors since when oxygen defects are present, electrons are released into the conduction band with a mobility greater than 10^4 cm^2 / V s at low temperatures [163], among the most prominent in any oxide [164]. Vacancies are also responsible of defect-induced ferroelectricity [165], defect-driven variations in thermal conductivity [166] and blue light emission [167] [168].

The physical properties of STO can also be tailored by cation substitution. For example, Nb (substituted on the Ti site) [169], La (substituted on the Sr sites) [170] and

Sb (substituted on the Ti site) [171] dope $SrTiO_3$ to give an n-type metallic conductivity, introducing also superconductivity at lower temperatures [150]. Additionally, p-doped STO can be achieved by Sc [172] and In doping [173].

In conductive STO-based heterostrucures, such as in the two dimensional electron gas (2DEG) at $LaAlO_3/SrTiO_3$ interface (LAO/STO) [5], it is often difficult to separate the different doping sources. While the proposed mechanism for 2DEG onset is strongly focused on $LaAlO_3$ polarity [65], which should result in an electron doping at the surface without structural defects, alternative mechanism have also been proposed. In particular, oxygen vacancies [66], intermixing at the interface [52] or non stoichiometric La:Al ratio have been invoked [174]. The identification and the explanation of the electronic structure of the conductive phase is still an active topic of research.

In most cases, the STO transport and structural properties are marked by the presence of a small contribution of electronic states in its gap, which usually cannot be directly probed with standard photoemission technique (XPS or UPS). However, these Ti related 3d states can be successfully probed by exploiting the photoelectron resonant enhancement at the 2p-3d absorption threshold. For instance, this method has been used to probe in-gap states in $LaAlO_3$-$SrTiO_3$ heterostructures [67], superconductivity in Nb doped $SrTiO_{3-\delta}$ [150] and point defects in TiO_2 [175] [176].

The objectives of this chapter are the study of a method to obtain a correct TiO_2 termination of the STO surface, directed to the production of substrates useful for the deposition of thin films, and the characterization of $SrTiO_{3-\delta}$ for various oxygen substoichiometry level (δ), carried out with resonant and standard photoemission spectroscopy (ResPES and XPS) and X-ray absorption spectroscopy (XAS). The defect density has been tuned by Ar^+ sputtering, in-vacuum annealing (at 600°C) and oxygen exposure cycles. The scope of this work is to provide reference data, which can be used as a guideline in order to discriminate oxygen vacancies and other structural defects from possible external doping sources. Furthermore, the simultaneous combination of standard core-level XPS, partial and total yield XAS and ResPES allows to access the electronic structure with a specific probing depth, thus allowing to disentangle surface and near-surface defects.

3.2 Experimental details

The $SrTiO_3$ termination study is carried out with an etching treatment similar to the one proposed by Koster et al. [177]: the as-received $SrTiO_3$ (100) MaTecK substrates are ultrasonically soaked in distilled water for 10 minutes, in order to induce the formation of Sr-hydroxide compounds on the surface. These surface compound can be easily eliminated by a selective etching of ≈ 30 seconds with a NH_4F-buffered HF solution (BHF, 1.25:8.75). The etching time is determined by an experimental analysis, which reveal that a longer etching exposition produce acid-induced pits on the surface of the substrate. The etching remnants are removed by ultrasonically soaking the substrate again in distilled water for 10 minutes. Additional hydroxide compounds are not produced since water doesn't react with TiO_2 terminated layers. The sample is then dried with a nitrogen-flow, and recrystallization of the surface is obtained by annealing the substrate at 950°C for 1 hour. The possible environmental and annealing-induced dust grain which can contaminate the surface are eliminated through an additional nitrogen flow treatment. The substrate termination and subsequent analysis is performed at the Surface Science and Spectroscopy Laboratory of the Università Cattolica (Brescia, Italy). The sample is analyzed through atomic force microscopy (AFM) measurements, which have been collected by a NT-MDT Solver Pro instrument, operated in semi-contact mode, and through X-ray photoelectron spectroscopy (XPS) and X-ray photoelectron diffraction

(XPD), which are carried out with the Al K α line ($h\nu = 1486.6eV$) of a dual-anode PsP X-ray source and a VG Scienta R3000 electron analyzer operating in transmission mode. In particular, the XPD measurements have been collected by exploiting the analyzer angular mode, which allows the simultaneous spectra acquisition in a $\pm 10°$ angular range in the polar direction.

In order to analyze the effects of surface and bulk defects the properties of the $SrTiO_3$ (100) MaTecK substrates are tailored by several treatments (Table 3.1): 1 kV Ar^+ sputtering cycles are used in order to generate surface defects, keeping the bulk crystal still insulating. Then, a vacuum annealing at high temperature (T $>$ 600°C) allows to create bulk oxygen vacancies, making the entire substrate conductive. The exposure to molecular oxygen during the substrate cooling induces the re-oxidation of the surface, also favoring the oxygen migration to the surface. The sample conductivity is not evaluated directly by transport measurements, but is deduced by the lack of an energy shift of the measured photoemission spectra, which is usually present in an insulating sample due to the accumulation of surface charge. Finally a 600°C annealing followed by Ar^+ sputtering generates defects both at surface and in bulk crystal, preventing the migration of oxygen to the surface and resulting again in a conductive sample.

Treatment	Sputtering	Annealing	Defects	Conductivity
A	1kV Ar^+	-	Surface	Insulating
B	-	600°C	Bulk	Conductive
C	1kV Ar^+	600°C	Surface,Bulk	Conductive

Table 3.1: Labels of the various treatments applied on the $SrTiO_3$ substrate. The different Ar^+ sputtering intensities and annealing temperatures are specified. The resulting defects and sample conductivity are also reported.

The NEXAFS, X-ray absorption, X-ray photoelectron spectroscopy (XPS) and resonant photoemission (ResPES) spectra have been measured at the ALOISA beamline of the Elettra synchrotron in Trieste (Italy). The peculiar ALOISA analysis chamber geometry allows to simultaneously collect total yield XAS, Auger channel partial yield and photoemission spectra with specific take-off angles, thus with variable probing depth. For instance, in the ResPES setup, photoemission is measured in the sample normal direction while XAS in partial yield is collected with a 60° take-off angle. The beamline works in a grazing ($\leq 8°$) incidence geometry, with p-type polarized X-rays; photon energy resolution was better than 0.25 eV while the final photoemission resolution was 0.3 eV.

3.3 Substrate termination

XPS analysis reveals that upon BHF termination the STO substrate maintains the correct stoichiometry, with a Ti:Sr ratio (1:0.95) similar to the expected 1:1 result. Thus the acid treatment doesn't induce an excessive alteration of the chemical composition of the sample surface. Furthermore, the surface morphology is improved upon substrate termination, as can be seen in the AFM topographic measurements performed before and after the treatment (Figure 3.1). Indeed, a clear step-like surface is observed as a result of the combined acid and heating treatment.

In order to further verify the quality of the treatment performed, the XPD result of the terminated sample is compared to the one measured for a commercially available TiO_2-terminated $SrTiO_3$ substrate (Shinkosha, JP), as reported in Figure 3.2.

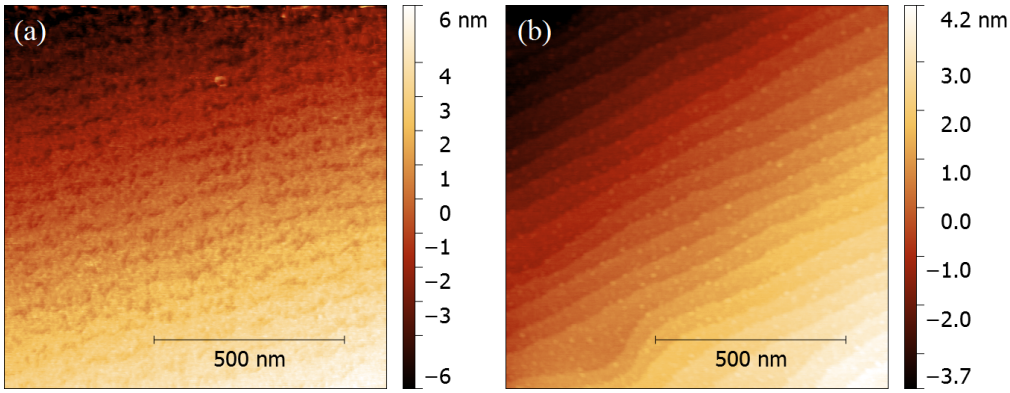

Figure 3.1: AFM measurements of a STO substrate performed (a) before the termination treatment and (b) after the termination.

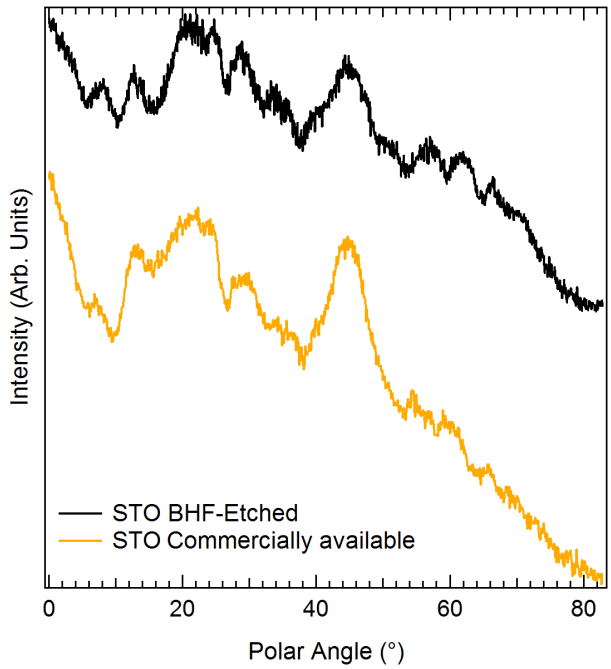

Figure 3.2: XPD results obtained from the Sr 3d XPS peaks analysis, evaluated for a STO substrate terminated through a combined acid and annealing treatment and for a commercially available TiO_2-terminated $SrTiO_3$ substrate. Measurements were performed with a fixed azimuthal angle ($\varphi = 0°$).

The XPD results are very similar for the two analyzed samples, thus confirming the high-quality of the substrates terminated through a combined acid and annealing treatment, which are thus a good template for the epitaxial growth of oxide thin films.

3.4 Defects analysis

The resonant photoemission and XAS data collected after the sequential treatment steps are reported in Fig.3.3. Detailed angle-resolved XAS and XPS core-level spectra are given in Fig.3.4.

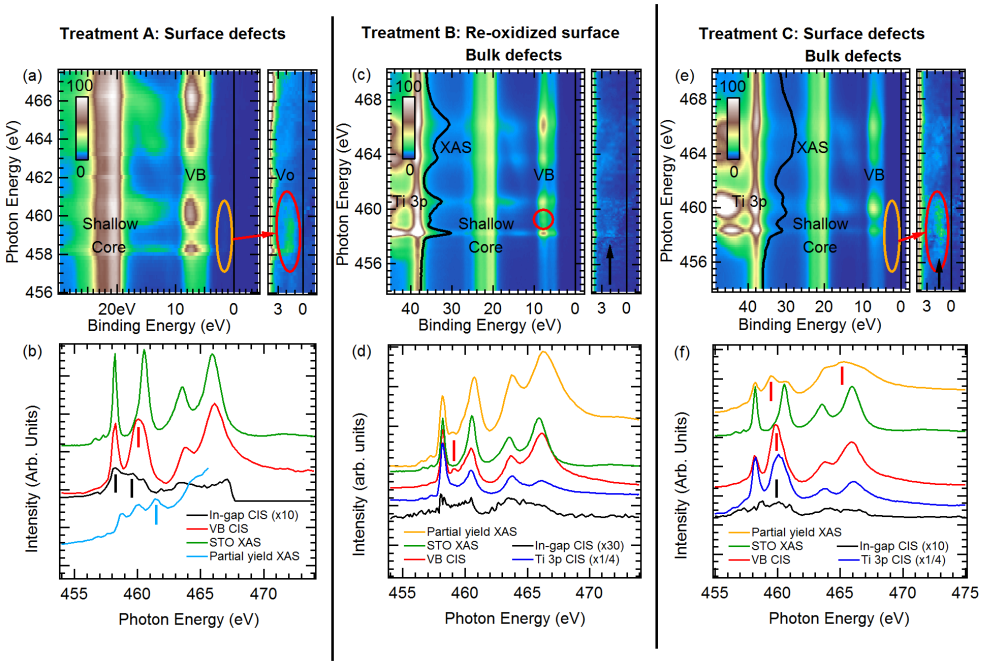

Figure 3.3: Data collected after the different treatment steps on the $SrTiO_3$ substrate. In (a), (c) and (e) the resonant photoemission spectra of the shallow core and valence band peaks are reported. In (b), (d) and (f) the constant initial state and partial yield XAS spectra collected on the $SrTiO_3$ substrate are shown. A magnified in-gap spectrum is also reported. The $SrTiO_3$ XAS, adapted from Ref.[67], is reported for reference.

The sputtering of the $SrTiO_3$ substrate generates surface defects, which spectroscopic signature is the formation of a near-Fermi structure in the resonant photoemission spectroscopy spectra at resonance (red circle in Figure 3.3 (a)). Strontium titanate is a strong insulator, and the accumulation of surface charge during the photoemission measurements induces a shift of the photoemission peaks, which is not constant as the photon energy is swept across the absorption edge (Figure 3.3 (b), blue line). As a result, a data post-processing was mandatory to recover the aligned map (Figure 3.3 (b), red line). Each photoemission spectrum has been normalized to the O 2s (at BE $\approx$ 20 eV) shallow core peak area; such normalization is justified by the localized nature of Ti core-hole which lead to the final autoionization process in ResPES. After this normalization is carried out, the VB (BE = 3 - 9 eV) resonances becomes detectable. Additionally, a weaker contribution of resonant electronic states in the STO gap (hereafter referred as in-gap states) is clearly visible (orange circle in Figure 3.3 (a)). In order to analyze the XAS features related to in-gap states, constant initial state (CIS) measurements have been also collected. Given the strong intensity of resonant process for Ti atoms, such CIS can be

effectively compared to standard XAS spectra. This comparison is shown in Figure 3.3 (b).

Pure $SrTiO_3$ XAS spectrum collected in total-yield mode (green line) can be considered in this case as the reference for the non defective crystal. Such spectrum is composed by seven peaks and can be easily calculated with Ti^{4+} atomic multiplet in an octahedral ligand field [178]. The second sharp XAS peak ($h\nu$ = 460.8 eV) is usually split in two components when the octahedral symmetry is lowered, such as in tetragonal rutile TiO_2 [175]. A good representative XAS of surface defect states can be also obtained by in-gap state CIS spectrum (black line), in which an additional resonating peak can be observed at $h\nu \approx 459.0$ eV. These electronic states can be obtained only by Ti^{3+} atomic configuration. Instead, resonant state in the VB are mostly due to the O 2p - Ti 3d hybridization [175] and should be measured in any STO sample. In fact, the CIS spectrum collected on the main VB (red line) follow closely the shape of crystalline STO. However, the small asymmetry of the second resonance peak (stressed by the red marker) already points out the presence of structural defects, which may alter the Ti octahedral coordination. ReSPES in this case is expected to show the same surface sensitivity of partial yield Auger detection. Standard XPS can not be performed due to charging effects.

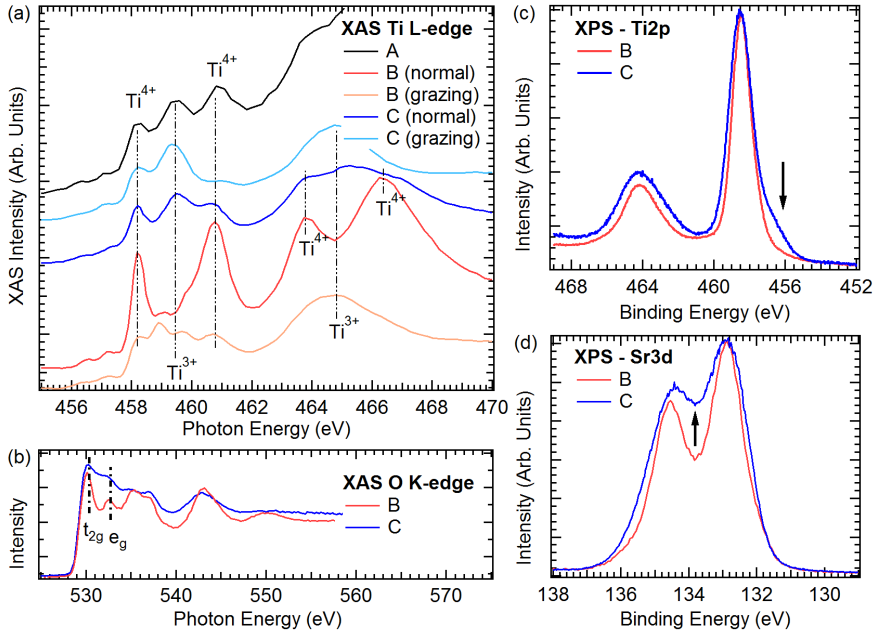

Figure 3.4: NEXAFS spectra at (a) Ti L-edge and (b) O K-edge, performed after the first sputtering treatment (A), after the first annealing and oxygen exposure step (B) and after the final combined sputtering and annealing treatment (C). (c) Ti 2p and (d) Sr 3d X-ray photoemission spectroscopy peaks are reported for treatment B and C.

The main effect of high temperature annealing (Fig.3.3 (c)) is to induce an highly defective bulk, which relieves the charging effects. The oxygen exposure helps the surface re-oxidation, at least in the range of X-ray electron spectroscopy measurements (few nanometers). A weak in-gap electronic structure can still be detected; its intensity re-

duction can be observed also with the related CIS, shown in Figure 3.3 (d) (black line, please note the scaling factor). Both partial yield XAS (yellow line), VB and Ti 3p CIS are in agreement with a nearly undefected $SrTiO_3$, with a small (but detectable) residual of defect state stressed by the red marker. Such small VB resonances contribution marks a clear difference between structural and electrostatic charging effects; in fact, in LAO/STO a much stronger in-gap state intensity can be observed, although VB CIS spectra does not show any visible sign of structural defects.

Photoemission spectrum from Ti 2p core level (blue line in Figure 3.4 (c), collected at $h\nu$=700 eV) doesn't show any sign of Ti^{3+}-like states, which should give a contribution at the lower BE side of Ti $2p_{3/2}$ peak. The actual depth of the residual defect state origin can be tracked out with the help of angle-resolved XAS spectra, given in Figure 3.4 (a). In fact, the grazing incidence (70° from the sample normal) partial yield XAS (orange line) is consistent with sample A results and shows a strikingly different shape from the one collected at normal emission (red line). Defect state should then be confined near to the STO surface (under the first layer), by considering the probing depth of either XPS and ResPES measurements.

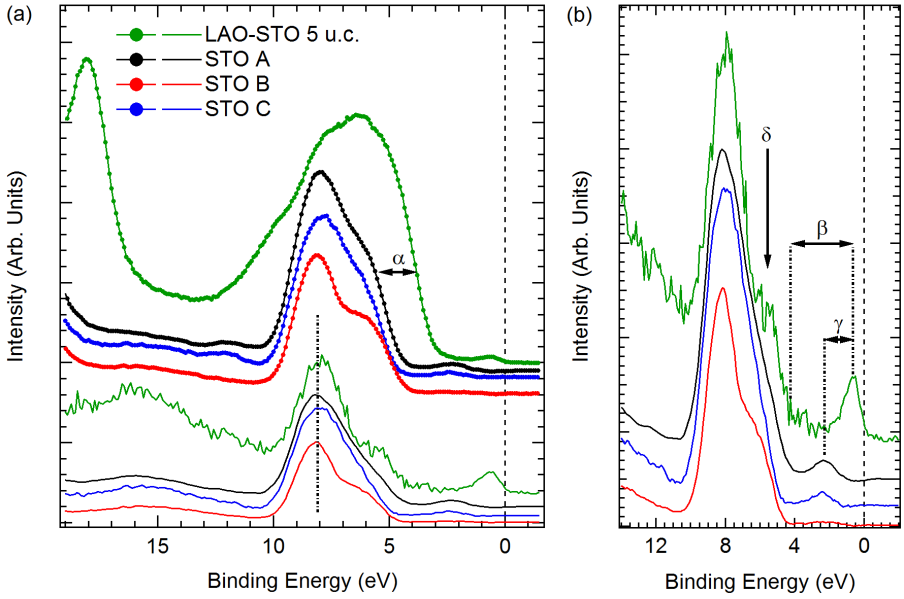

Figure 3.5: (a) Valence band spectrum at the Ti^{3+} maximum resonance and (b) on-off resonance subtraction evaluated for the different treatments applied on the $SrTiO_3$ substrate. The spectra characteristic of the $LaAlO_3/SrTiO_3$ heterostructure are reported as a reference.

Finally, vacuum annealing at 600°C followed by an Ar^+ sputtering step results in a sample showing both surface and bulk crystal defects. Indeed, studies on ion sputtered and subsequent annealed STO (100) surfaces [161] show that the bombardment depletes the surface in O and Sr with respect to Ti, and the annealing doesn't restore the surface stoichiometry (even though a well-ordered surface is detected), mainly due to the formation of Ti^{3+} ions associated to oxygen vacancies. After this combined treatment step a large in-gap CIS intensity arises (Figure 3.3 (f), black line), which is comparable to the results observed after the first sputtering treatment. Thus the amount of defects features

revealed by ResPES (Figure 3.3 (e)) are mainly related to the sample surface defects. The main valence band (Figure 3.3 (f), red line) CIS shows less Ti^{4+} character than the partial yield XAS (red ticks), due to larger probing depth of partial yield XAS than valence band ResPES, as can be seen in the grazing NEXAFS results reported in Figure 3.4 (a). XPS Ti 2p spectrum shows the expected additional Ti^{3+} features (Figure 3.4 (b)) and also Sr 3d display an overall larger broadening due to the increased structural disorder (Figure 3.4 (c)).

The O K-edge XAS of oxidized surface is compatible with STO in literature [142], and surface defects results in a relevant XAS profile XAS broadening. Finally, the valence bands Ti^{3+} contribution is evaluated for the different treatments applied on the $SrTiO_3$ substrate. The resulting VB spectrum at the Ti^{3+} maximum resonance is reported in Figure 3.5.

The $SrTiO_3$ spectra reported in Figure 3.5 are aligned to the VB Ti 3d - O hybridized states resonance maxima, only for comparison, and the $LaAlO_3/SrTiO_3$ reference is adapted from Ref.[43]. The $LaAlO_3/SrTiO_3$ and $SrTiO_3$ valence states apparently display a large offset (α) due to the $LaAlO_3$ states contributing to the VB [43]. The distance of VB and Ti^{3+} states (β) is larger in $LaAlO_3/SrTiO_3$ heterostructure because of the different type of doping mechanism. In the $SrTiO_3$ case, even with the correct binding energy, in-gap states do not lie at the Fermi Edge (γ). Spectral weight of feature δ is sharper in the $SrTiO_3$ with surface defects, while in $LaAlO_3/SrTiO_3$ the valence band resonance is similar to re-oxidized $SrTiO_3$, suggesting a similar physical origin (i.e. a comparable number of defects).

3.5 Conclusions

In conclusion we demonstrated that etched $SrTiO_3$ substrates show a surface topography and XPD signal similar to those observed in commercially available high quality TiO_2-terminated substrates. Resonant photoemission data on defected $SrTiO_3$ crystals show an enhanced near-Fermi signal for the samples with surface defects as compared to the re-oxidized sample. CIS spectra on valence band and in-gap states can be effectively used to identify the Ti bonds type and defects density, with a stronger Ti^{3+} weight for defected surfaces and with the expected enhancement for grazing angle measurements. Doping mechanism from $SrTiO_3$ defects results in different in-gap spectra respect to $LaAlO_3/SrTiO_3$ heterostructures, and the valence band measurements in $LaAlO_3/SrTiO_3$ are compatible with the CIS of a re-oxidized STO surface.

CHAPTER 4

Bismuth ferrite

4.1 Introduction

4.1.1 Growth and characterization

Multiferroic materials, which can simultaneously display ferroelectricity, ferromagnetism (or antiferromagnetism) and ferroeleasticity, have already attracted much attention due to the promising multifunctional device applications [179]. In particular, multiferroics properties can be exploited in magneto-electric sensors [180], ferroelectric random access memories [181], photonic crystal devices [182], spintronics applications [183] and solar cells [184]. Since most of these materials are oxides and belong to the perovskite structure group, multiferroics could be also combined in complex heterostructures junctions, which are now opening the field of oxide-based electronics [14, 185].

The bismuth ferrite ($BiFeO_3$) is the only room temperature single-phase multiferroic material, with high ferroelectric Curie temperature (T_C = 1103 K) and Neel temperature (T_N = 643 K) [8]. The $BiFeO_3$ thin films are usually grown by PLD (pulsed laser deposition) [86], MBE (molecular beam epitaxy) [186] and by sputtering depositions [187, 188], which offer several technical advantages. The sputtering deposition is fast (typically 1-10 Å s^{-1} [109]), cheap and produces samples with a large practicable area; for these reasons, is one of the most common deposition techniques used in industrial applications. In order to be suitable for devices production, sputtered polycrystalline films must display characteristics similar to those shown by epitaxial layers, both in term of local crystal structure, low secondary phases inclusions and, of course, multiferroics properties.

In order to obtain high quality films, a fine tuning over the growth conditions, such as the gas composition and pressure in the deposition chamber [189], the sputtering power [190] and the substrate temperature [191], is required. Several optimal temperatures have been claimed in literature, spanning from low (400° C [188, 189, 191]) to high (500-700°C [184, 189, 190]) ranges; additionally, $BiFeO_3$ film properties can be tailored by post-growth treatment, such as O_2 annealing, for which only few works are reported in literature [190, 192]. As a rule of thumb, a low growth (or annealing) temperature should result in smooth, amorphous films, while high temperatures should lead to high roughness, due to the nucleation of $BiFeO_3$ and secondary phases crystals. A good balance of morphology and crystalline order must be found. Stoichiometric sputtering is usually achieved from a $BiFeO_3$ target with 10% excess Bi ($Bi_{1.1}FeO_3$), prepared by sintering the constituent oxide mixture powders of Bi_2O_3 and Fe_2O_3 [8, 191]. Anyway, while the crystalline order of thick films can be easily detected by X-ray diffraction (XRD) measurements, a quantitative evaluation of the film stoichiometry through X-ray photoemission (XPS) is missing in literature; this fact may be due to the lack of a proper

XPS measurements calibration, which has to be performed through an appropriate data analysis on a well characterized analyser [193].

In the first part of this chapter, a detailed characterization of $BiFeO_3$ thin films grown on Si substrates by RF magnetron sputtering is reported, carried out with a large set of spectroscopic and microscopic techniques (XPS, μ-Raman, X-ray diffraction, atomic and piezoresponse force microscopy) for various growth temperatures and post-growth treatments. In particular, the well calibrated XPS data can be used as a reference for an accurate stoichiometry detection of Bi/Fe ratio, supported by imaging techniques. For the optimal growth regime, an additional X-ray absorption spectroscopy and X-ray magnetic circular dichroism (XAS and XMCD) analysis is also shown, with the aim to underline possible small differences with respect to other iron oxides spectra and to prove the film antiferromagnetism.

4.1.2 Interface investigation

The second part of this chapter is focused on the interaction at the interface between $BiFeO_3$ films and $SrTiO_3$ substrates, which is of fundamental interest since the physics of oxides interfaces is one of the most promising research field for materials engineering. In fact, the discovery of a two-dimensional electron gas (2DEG) [5] at the interface between lanthanum aluminate ($LaAlO_3$, LAO) and strontium titanate ($SrTiO_3$, STO) has disclosed relevant perspectives in the physics of oxide-based junctions. Perovskite structures research strongly depends on the availability of clean procedure for substrate termination and on reliable growth method for high-quality epitaxial thin films, mainly pulsed laser deposition (PLD) [194] and molecular beam epitaxy (MBE) [45]. Apart from $LaAlO_3$, many other polar ($A^{3+}B^{3+}O_3^{6-}$) perovskite materials have also been considered; for instance [81], a 2D conductive layer has been detected also in $PrAlO_3$, $NdAlO_3$, $NdGaO_3$ and $LaGaO_3$, suggesting a rather universal mechanism for the conductivity onset.

Among perovskites with trivalent cations, bismuth ferrite ($BiFeO_3$, BFO in short) is a promising candidate material for epitaxial ABO_3/STO heterojunctions, with the additional properties of being a multiferroic. While bulk crystals display a rhombohedral symmetry [8], epitaxial growth results in a strained orthorhombic structure [195], which still shows multiferroicity. BFO properties could then be used to permanently tune the 2DEG carrier density through ferroelectric domain modulation techniques, such as piezoresponse force microscopy (PFM). STO is the substrate of choice for BFO growth, due to the good matching of cubic lattice parameter (≈ 3.9 Å) [196]. However, in order to investigate its multiferroic properties, in most cases BFO is grown on conductive doped Nb:STO crystals [86], or on epitaxial buffer layers such as $SrRuO_3$ [184].

So far, only few [151, 197] studies have been devoted to the bare STO/BFO interface and to possible novel heterojunction effects. In fact, a conductive layer has been measured by means of cross sectional AFM [87], although the authors suggest a cationic interdiffusion as a probable source of conductivity. An experimental, direct measurement of the sheet resistivity or the carrier density is still lacking in literature.

To achieve heteroepitaxy, the sputtered BFO films should display an excellent quality, in term of crystal structure, homogeneity and absence of secondary phases. In this sense sputtering is considered a rough deposition technique, which in general results in low-quality films. Moreover, sputtering also lacks accurate in-growth characterization techniques, as opposite of PLD in which reflection high-energy electron diffraction (RHEED) can be used to monitor the growth process; as a result, counting the absolute number of deposited layer can be difficult. The feasibility to achieve epitaxial growth by RF sputtering has already been proved (see e.g. Koster et al.[12] and Ziegler et al.[198]).

However, the epitaxial growth of $BiFeO_3$ on properly terminated $SrTiO_3$ by RF sputtering has been so far virtually neglected.

The objective of the second part of this chapter is then to demonstrate the heteroepitaxial growth of ultrathin BFO films on STO (001) by means of RF-sputtering, suitable to X-ray spectroscopies interface investigation and to test X-ray photoelectron diffraction (XPD) as an effective tool to track the transition from amorphous to epitaxial ultrathin layers. The band alignment at the interface is finally evaluated.

4.2 Experimental Details

The $BiFeO_3$ thin films have been grown by RF magnetron sputtering on Si (111) substrates for the first part of the chapter and on TiO_2-terminated STO (001) substrates for the second part, from a 2" target made of a sintered Bi_2O_3/Fe_2O_3 mixture. The sputtering power was 120 W for the deposition on Si and 80 W for the deposition on STO, with an Ar flux in the 1.9 - 2.3 sccm range and a 8.5 x 10^{-3} mbar pressure.

For the growth and characterization section the film thickness has been set to be about 100 nm, according to calibrated sputtering rates. Film crystallization has been achieved either with post-growth annealing in air and with in-growth direct heating. Good adhesion of $BiFeO_3$ on Si substrate has been obtained through the removal of surface SiO_2 with HF etching (for the RT deposition) and with in-vacuum high temperature flash annealing.

The BFO/STO interface investigation needs a substrate termination which has been achieved through HF buffered solution treatment, following the method described by Koster et al [177]. Several films have been grown at different deposition temperatures, ranging from RT up to nearly 700°C. In order to trigger the epitaxial growth an off-axis deposition geometry has been selected, which reduces the re-sputtering mechanism and allows for a more homogeneous energy distribution of the deposited material [199, 200]; as an additional test, two films have been grown in normal and partially off-axis geometry (sample normal tilted of 70° from the deposition axis).

The XPS data have been performed with the Al K_α line ($h\nu$=1486.6 eV) of a non-monochromatized dual-anode PsP X-ray source and a VG Scienta R3000 electron analyzer operating in transmission mode. In X-ray photoelectron diffraction (XPD) measurements the angle between X-ray direction and analyzer axis is fixed at 55.4°. Single XPD spectra are collected by rotating the sample polar angle (θ) by step of 5°, exploiting the analyzer angular mode [193], which allows for the simultaneous acquisition of XPS data in a $\pm$10° range in the the polar direction. Full stereographic images are collected by performing single XPD spectra acquisition for various azimuthal angles (ϕ) in the -5°,95° range at step of 2.5° each. Data are subsequently 4-fold symmetrized to obtain the full image. Each component of Bi 4f spin-orbit doublet spectra have been measured and subtracted with a Shirley-type background.

Multiple scattering XPD calculations have been performed with the EDAC calculation software [201]. Convergence in angular momentum expansion and scattering order have been carefully checked. Because of the high Bi 4f kinetic energy ($\approx$ 1320 eV) as excited by Al K_α source, a large cluster ($>$ 1300 atoms) calculation was needed; however, the scattering order requirements were partly reduced by the relatively low electron inelastic mean free path, due to the $BiFeO_3$ high density. A total of six Bi atoms emitters, placed at a different depth in the cluster, have been included in the calculation. Both a cubic and rhombohedral [185] $BiFeO_3$ perovkites structures have been considered (the parabolic clusters are shown in Figure 4.9 (d) and 4.9 (e), respectively); in both cases the cubic cell parameter has been fixed to the STO value (3.95 Å). An additional oscillation

dumping correction have been included in order to mimic the presence of surface carbon contamination, due to sample transfer in air to the analysis chamber. Calculated XPD images in this work have been represented on the same angular grid of experimental data for a better comparison.

Atomic and piezoresponse force microscopy (AFM and PFM) have been collected by a NT-MDT Solver Pro instrument, operated in semi-contact mode for morphology measurements and in contact mode (with a conductive, Pt coated tip) for the PFM measurements. Micro Raman (μ-Raman) data have been collected with an In-Via confocal Renishaw microscope, with a lateral resolution of 1 μm at 100x magnification and a 633.3 nm He-Ne laser source.

The film growth and XPS, XPD, AFM/PFM and Raman analysis have been carried out at the Surface Science and Spectroscopy Laboratory of the Università Cattolica (Brescia, Italy). The X-ray diffraction (XRD) data was collected at the Chemistry for Technologies Laboratory of the University of Brescia, using a Bruker D8 grazing incidence diffractometer, with a Cu K_α X-ray source. X-ray absorption spectroscopy (XAS), linear dichroism (XLD), magnetic dichroism (XMCD), and resonant photoemission (ResPES) measurements have been carried out at the CNR-BACH beamline at the Elettra synchrotron facility in Trieste (Italy). The magnetic dichroism experiments have been carried out at a temperature of 4 K, with a magnetic field in the range of $\pm$5 T.

4.3 $BiFeO_3$ on Si - Growth and characterization

The labeled samples list with growth or post-growth temperatures (T_G and T_{PG}) is given in Table 4.1; samples B and C have been grown at room-temperature (RT) and subsequently annealed in air at the specified T_{PG} temperatures, while samples D, E and F have been grown on substrates heated at T_G. Table 4.1 also includes the estimated roughness and average crystal size obtained from AFM data of Figure 4.1. In particular, the average lateral sizes have been obtained by a statistical analysis carried out on more than one hundred particles for each film; the resulting distribution full width half maximum is around 25% of the average value in each case. Sample A (RT deposition, without post-growth treatment) is amorphous, thus in this case crystal size statistic has not been performed.

Label	T_G (°C)	T_{PG} (°C)	Roughness (nm)	Crystal Size (μm)	Fe:Bi ratio
A	RT	-	-	amorphous	0.93
B	RT	300	0.67	0.033	0.81
C	RT	500	16.46	0.057	0.61
D	500	-	8.59	0.14	0.84
E	550	-	39.81	0.35	0.99
F	600	-	54.54	0.45	1.21

Table 4.1: Sample labels with growth or post-growth annealing temperatures (T_G and T_{PG}, respectively); in the fourth and fifth column, average roughness and crystals average lateral size deduced from AFM (Figure 4.1) are summarized; in the last column, Fe:Bi stoichiometry ratio deduced by XPS analysis of Fe 2p and Bi $4p_{3/2}$ core-level peaks (Figure 4.3) is reported.

In general, the crystallite average size and the film roughness are increasing with the temperature. RT depositions (Sample A) results in a remarkable smooth and amorphous film, while a mild annealing at 300°C (Figure 4.1 (d), Sample B) already leads to the nucleation of small nanometric aggregates. However, the growth of pristine $BiFeO_3$

crystals is triggered only for temperatures larger than 500°C, consistently with reports in literature [202, 203].

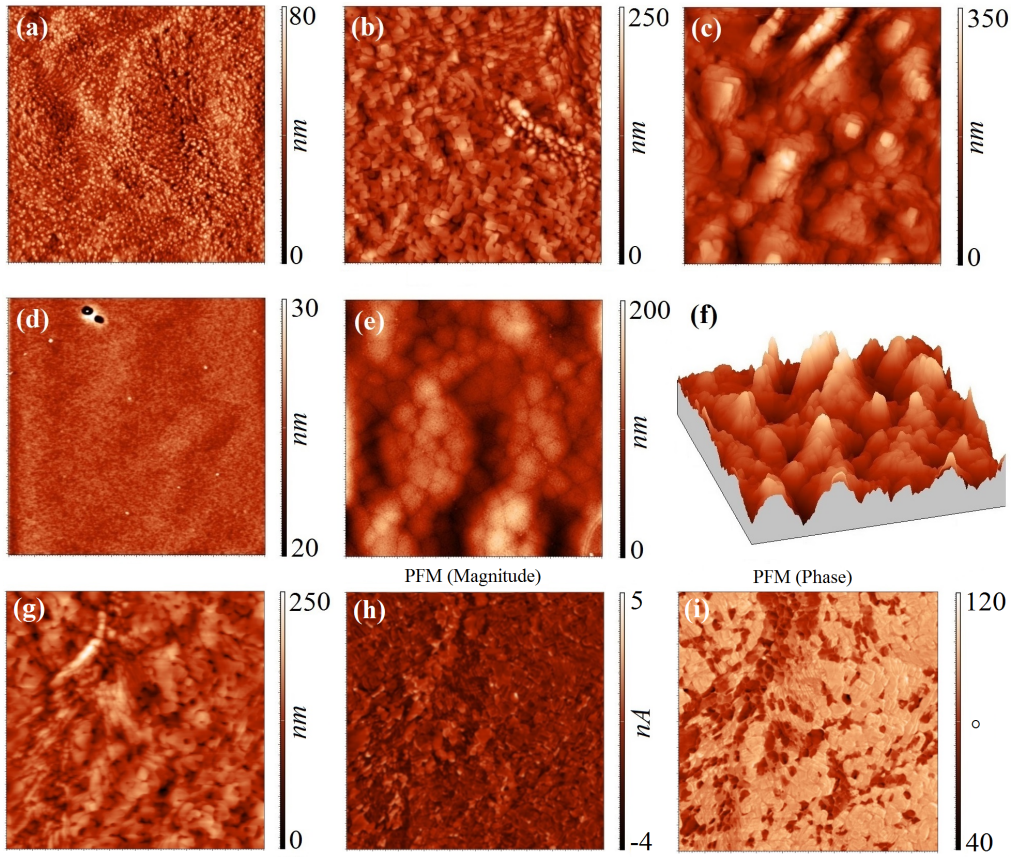

Figure 4.1: AFM topographic analysis carried out on $BiFeO_3$ films with different growth temperatures ((a) 500°C, (b) 550°C, (c) 600°C). AFM data on post-growth annealed films ((d) 300°C, (e) 500°C) are also reported. (f) 3D plot of image (c). (g) AFM topographic scan compared with the PFM images (h, PFM magnitude) and (i, phase) collected simultaneously on the $BiFeO_3$ film grown at 550°C. Each image covers an area of $10 \times 10\ \mu m$.

Both in-growth and post-growth annealed films thus exhibit a polycrystalline structure; however, the same treatment temperature (500°C, Sample C and D) induces notable differences of the surface morphology. The in-growth process (Figure 4.1 (a), Sample D) results in an almost homogeneous distribution of nanocrystals, while the post-growth annealing (Figure 4.1 (e), Sample C) leads to a mixture of large clusters (vertical structures) and smaller nanocrystals resulting in a larger average roughness.

The film homogeneity is strongly reduced for the highest growth temperature considered (600°C, Figure 4.1 (c), Sample F), due to the formation of vertical structures (Figure 4.1 (f)) which leads to an overall roughness of ≈ 54 nm. This pillar-like growth is also marked by a local preferential orientation; vertical crystal nucleation likely follows the template induced by the early $BiFeO_3$ crystal layer in contact with the Si substrate. In this case, the crystal lateral size obtained by AFM is less reliable, since each crystal can

be connected to others.

The growth at 550°C (Sample E) shows an intermediate behavior, displaying both a good crystallinity and homogeneity. AFM alone can not be used to rule out the presence of Bi_2O_3 or Fe_2O_3 secondary phases; however, with the use of a conductive probe, it is possible to track the sample piezoelectric response (i.e. the local morphology modification) due to the voltage applied by the tip in AFM contact measurements.

An example of the PFM analysis is shown in the last row of Figure 4.1. Due to the polycrystalline morphology, we do not expect a direct observation of single piezoelectric domains; however, with PFM it is possible to analyze the different piezoelectric response due to the various orientation of each single crystallite. Figure 4.1 shows a PFM (Figure 4.1 (h)-(i)) /AFM (Figure 4.1 (g)) scan for Sample E. The PFM contrast is given by the signal oscillation amplitude and phase at AFM detector, proportional to the tip deflection. Both the PFM magnitude (Figure 4.1 (h)) and phase (Figure 4.1 (i)) images provide a good contrast; the latter, in particular, highlights large crystal groups with a markedly different piezoelectric response orientation. By considering the differences between morphological (Figure 4.1 (g)) and PFM data, we thus ascribe the measured image contrast to a real piezoelectric response and not to an imaging artifact. Similar PFM results have been obtained in several different film areas. Since both Fe_2O_3 and Bi_2O_3 phases are not expected to display piezoelectricity, we thus conclude that the deposited films are mainly composed by $BiFeO_3$.

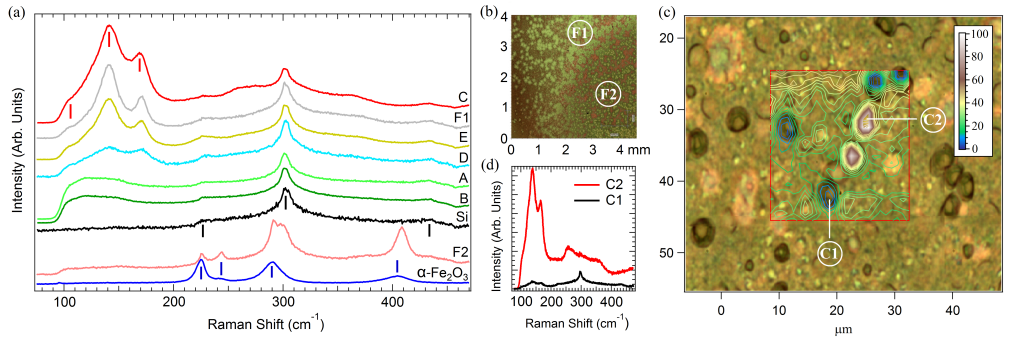

Figure 4.2: μ-Raman analysis survey (sample labels in Table 4.1). Panel (a), μ-Raman spectra; predominant features are marked in red ($BiFeO_3$), black (clean silicon) and in blue (Fe_2O_3). (b) Optical image in true colors (5x magnification) of the Sample F. Reference positions for panel (a) spectra are also shown. (c) μ-Raman map (100x magnification) of the Sample C; contour lines are obtained from the spectral intensity in the 90-200 cm^{-1} range. The $BiFeO_3$-poor (rich) areas are marked with blue (yellow) lines. Corresponding spectra are shown in panel (d).

The crystalline order has been further verified by μ-Raman analysis. Raman spectra, shown in Figure 4.2 (a), clearly display the $BiFeO_3$ signal, superimposed to the Si background (black line), for temperatures larger than 500°C, while for lower temperatures the spectra display broadened and smaller $BiFeO_3$ peaks. It should be pointed out that these spectra are comparable to other similar films in literature [204], and should not be compared with single crystal $BiFeO_3$ Raman results [205]. The intensity of 110-190 cm^{-1} features is enhanced at larger temperatures; however, true-color optical images (Figure 4.2 (b)) consistently display the formation of large crystals, analogous to the vertical structures detected by AFM at large annealing temperature. Moreover, the spectra collected in optically different areas (F1 and F2 labels in Figure 4.2 (a)-(b)) of the sample

grown at 600°C (Sample F) are markedly different; the spectra collected in area F2 (pink line in Figure 4.2 (a)), show new features at 220-250 cm^{-1}, 280-295 cm^{-1} and 395-420 cm^{-1}, which are expected in α-Fe_2O_3. Similar large crystallite can be clearly detected in optical images of Sample C; in this case, a detailed Raman mapping (Figure 4.2 (c)) reveals the presence of large $BiFeO_3$ crystals (selected spectrum collected on C2 mark is shown in Figure 4.2 (d)), lying on a disordered background (C1 mark). However, in this case α-Fe_2O_3 features are never detected.

The stoichiometry ratios have been evaluated through XPS analysis of Fe 2p and Bi $4p_{3/2}$ XPS core levels, shown in Figure 4.3. The spectral shape and the binding energy of Fe and Bi core levels are identical to Bi^{3+} and Fe^{3+} ionic state reported in literature [206], for any thermal treatment; however, the peak area intensity, normalized to Fe $2p_{3/2}$ core level, display substantial differences. An absolute quantitative analysis has been carried out, performed after a proper data processing (satellites removal and calibration of the analyzer transmission function) and with the use of relativistic sensitivity factors [193]; the latter are mandatory, due to the bismuth high atomic number. Quantification results reveal deviations from the 1:1 Bi-Fe expected ratio (Table 4.1), which can be ascribed to residual impurity phases, such as Fe_2O_3 and Bi_2O_3. Each sample displays a slightly excess of bismuth with the exception of the 600°C growth, which shows a Fe excess which is likely due to a Fe_2O_3 segregation, compatible with the μ-Raman analysis. In this case, the different inelastic background of Fe 2p (red arrow in Figure 4.3) suggests the secondary phases to be segregated at the surface. Notably, the sample grown at 550°C displays a nearly optimal 1:1 ratio; angle resolved XPS measurements (not shown here) display the same stoichiometry ratio at large XPS take-off angle too, thus proving the absence of surface segregation for the entire XPS probing depth range. By comparison of XPS, AFM and Raman results we thus conclude that, in order to achieve adequately homogenous single-phase $BiFeO_3$ thin films, a 550°C growth temperature should be adopted for Si substrates.

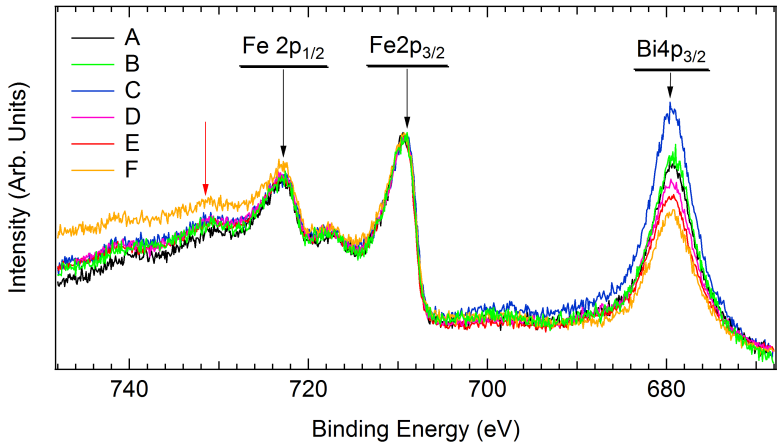

Figure 4.3: Fe 2p and Bi $4p_{3/2}$ XPS spectra (sample labels in Table 4.1). Spectra have been normalized to the Fe $2p_{3/2}$ peak area.

An additional grazing incidence XRD analysis has been carried out on the optimally grown sample (Figure 4.4). Each expected peak (with the expected fine splitting) for the rhombohedral $BiFeO_3$ structure can be found; the only additional peak, located at

$2\theta = 29.5°$, can be ascribed to the silicon substrate. The contribution of secondary phases such as α-Fe_2O_3, γ-Fe_2O_3 and Bi_2O_3 are absent, thus proving the good film quality.

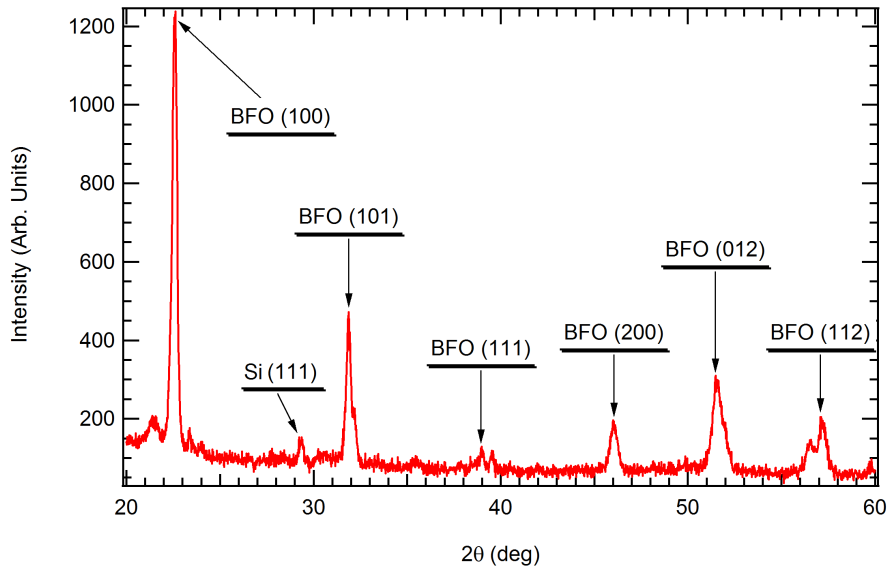

Figure 4.4: XRD data (incidence angle: 1°) obtained from the $BiFeO_3$ sample grown with a substrate temperature of 550°C.

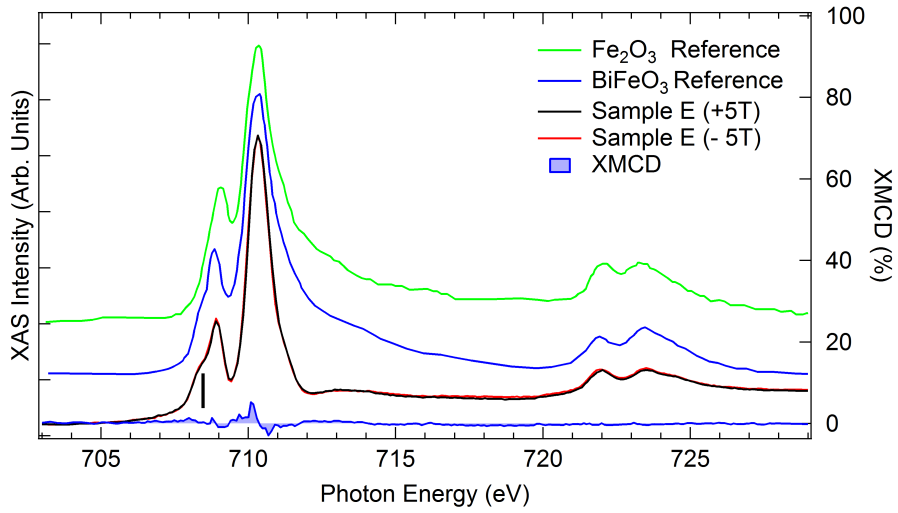

Figure 4.5: XAS and XMCD data obtained from the $BiFeO_3$ sample grown with a substrate temperature of 550°C. The XAS data is compared to the $BiFeO_3$ and α-Fe_2O_3 spectra, adapted from [207] and [208] respectively.

Finally, the XAS spectrum obtained from the sample grown at 550°C (Figure 4.5,

black and red lines) is comparable with data in literature and is rather similar to the Fe_2O_3 one (green line, [207]). In fact, the distorted octahedral coordination of Fe^{3+} ions in the oxygen cage in the structure of $BiFeO_3$ should be nearly identical to the Fe_2O_3 one, especially in polycristalline samples which are not influenced by epitaxy-induced strain. However, a small peak on the pre-edge feature (hν=708.2 eV , black marker) can be found in epitaxial $BiFeO_3$ spectra (blue line, [208]), thus suggesting high quality deposition despite the simple growth method. The overall smaller peak width of our measurements also testify the good film quality. Moreover, XMCD (X-ray Magnetic Circular Dichroism) measured at $\pm$ 5 T (Figure 4.5, blue area) shows a nearly absent signal (despite the large applied magnetic field, see e.g. for comparison [209]), which confirms the antiferromagnetism. With these findings, each expected multiferroic properties is thus proved in this $BiFeO_3$ film.

4.4 $BiFeO_3$ on $SrTiO_3$ - Interface analysis

In order to perform an accurate interface analysis a high-quality sample is needed, and a characterization step of the grown film is thus necessary. The Bi:Fe stoichiometry has been obtained through the analysis of Fe 2p and Bi $4p_{3/2}$ core levels, with the method shown in the previous section; the thickness analysis has been carried out on Bi 4f and Sr 3d photoemission peaks. By analyzing AFM images, XPS quantification and XPD results, stoichiometric epitaxial growth has been achieved in the 540-580°C temperature range. Such results are consistent with the optimal growth conditions for polycrystalline BFO reported in the previous section [210].

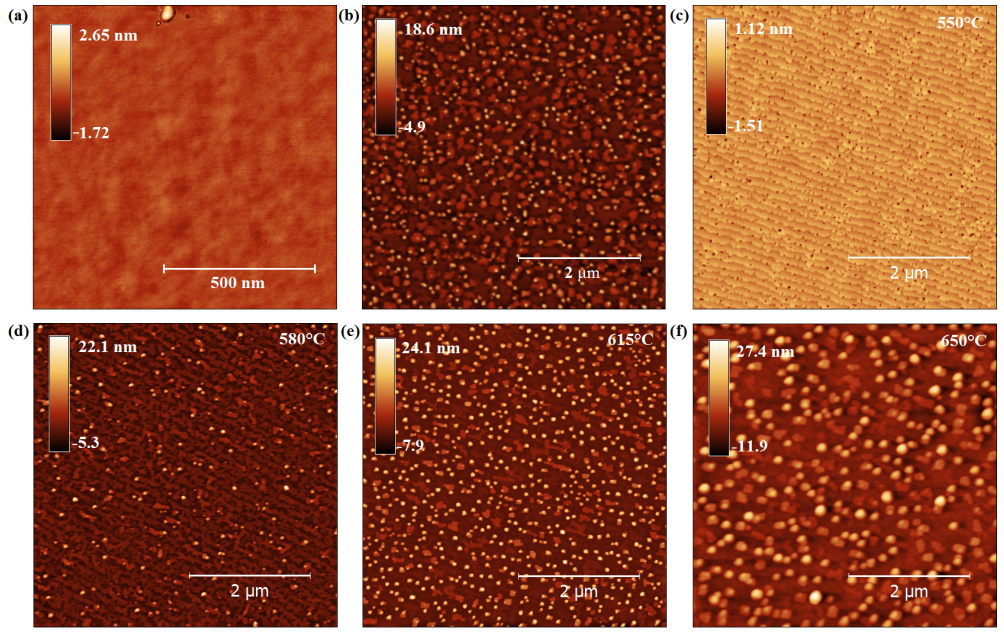

Figure 4.6: AFM topographic images of $BiFeO_3$ films with different temperature and geometry. (a) Amorphous sample, grown at room temperature (area 1×1 μm). (b) Semi off-axis geometry at 500°C. BFO films grown in off-axis geometry at (c) 500°C, (d) 580°C, (e) 615°C and (f) 650°C. Each image beyond the first covers an area of 5×5 μm.

In Figure 4.6 the AFM characterization of the $BiFeO_3$ films topography for different growth geometries and temperatures is shown. Growth temperature lower than 500°C results in amorphous BFO films; for example, the AFM image of a room-temperature BFO film deposited on TiO_2 terminated STO is shown in Figure 4.6 (a). It should be noted that this film has been grown with identical deposition parameters of optimally grown epitaxial samples (Figure 4.6 (c)) and shows the same thickness on XPS analysis. The film thickness, as estimated by XPS, is indeed 3.41 $\pm$ 0.05 nm for each film, compatible with a coverage of 9 $BiFeO_3$ cubic unit cells. Deposition time (140 s) has been kept fixed for each film. While AFM alone often does not allow to discriminate the epitaxial degree in ultrathin overlayers [211], in this case the image of Figure 4.6 (a) is markedly flatter and featureless as compared to epitaxial data.

AFM images collected on partial off-axis growth (20° tilt of sample holder respect to normal emission) at the ideal temperature show the superposition of flat, ordered areas and isolated crystals; such morphology is possibly due to the rather high energy of some of the sputtered atoms, which may damage the substrate and induce seeds for nanocrystal growth.

The growth of secondary phases can also be observed in high-temperature ($\geq$ 550°C) BFO growth. The increase of the $SrTiO_3$ substrate temperature during the deposition results in the formation of nanocrystals with a 40 nm lateral size for the sample grown at 580°C (Figure 4.6 (d)), a 54 nm size for the sample grown at 615°C (Figure 4.6 (e)) and a 121 nm lateral size for the sample grown at 650°C (Figure 4.6 (f)). From the XPS analysis the stoichiometry of the film was found to be different for the four samples; the nearly ideal 0.98 Fe:Bi ratio characteristic of the optimal sample (grown at 550°C, Figure 4.6 (c)) was increased up to 1.28 for the sample grown at 650°C. The excess of Fe atoms thus suggests the presence of Fe_2O_3 nanocrystals. Such findings are consistent with the expected optimal growth temperature range for BFO; similar results have been reported on polycristalline samples [210] grown with RF sputtering.

The comparison between the AFM images of properly TiO_2 terminated STO and epitaxial BFO film, deposited at 550°C, is shown in Fig.4.7.

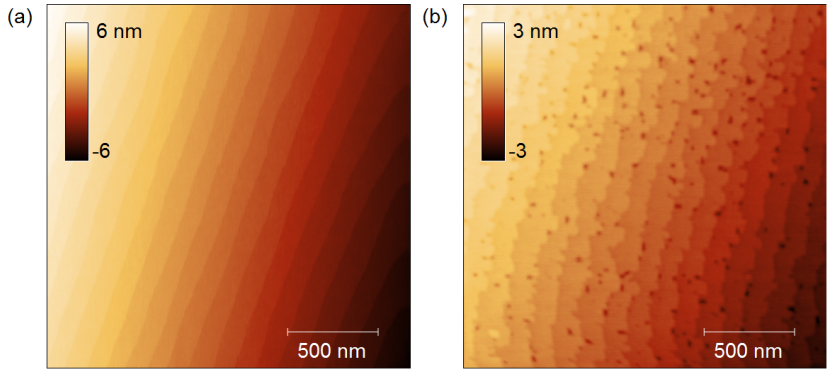

Figure 4.7: AFM topographic images of (a) TiO_2 terminated $SrTiO_3$ (001) substrate and (b) $BiFeO_3$ film grown on $SrTiO_3$.

The STO substrate (Figure 4.7 (a)) displays regular terraces of an average width of 108 nm and a step height of 3.8 $\pm$ 0.1 Å, corresponding to a miscut angle of 0.20°. AFM of deposited film (Figure 4.7 (b)) displays an epitaxial terraces coverage, with the same width and step height of the substrate. Though small holes due to incomplete upper

layer reconstruction can be observed, our result is particularly remarkable by considering the lack of real-time growth control provided by RHEED in conventional PLD or CVD deposition. Furthermore, the optimal Bi:Fe ratio mitigates the possible presence of surface segregation of secondary phases.

The final proof of the epitaxial order of the films has been obtained by means of XPD (Figure 4.8), carried out by evaluating the Bi 4f XPS area while rotating the sample polar angle in the [010] plane. As a reference, similar XPD spectra have been collected on Sr 3d core levels of the bare STO substrate; in fact, Bi and Sr should share equivalent lattice sites and in the high kinetic energy regime the XPD modulation is mostly due to forward scattering.

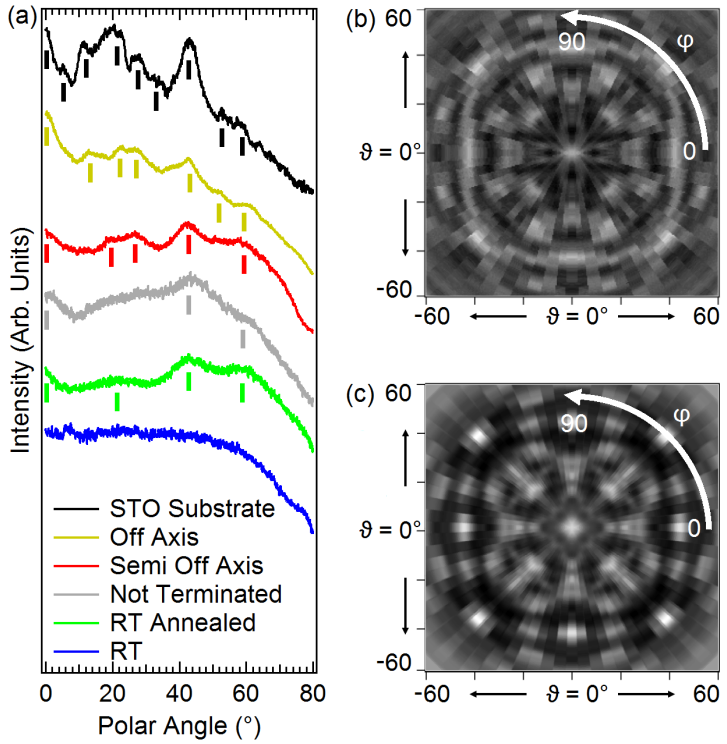

Figure 4.8: (a) XPD analysis of Bi 4f XPS peak area from a $BiFeO_3/SrTiO_3$ heterostructure for different growth conditions (data obtained from Sr 3d of STO substrate is also shown as a reference). The main XPD peaks are marked with ticks. The spectra are collected by sweeping the sample polar angle in the (010) substrate plane, with a fixed azimuthal angle ($\varphi = 0°$). Experimental (b) and simulated (c) full XPD stereographic patterns.

The data reported in Figure 4.8 (a) display how XPD can be used as a characterization tool of thin film epitaxial growth. As expected, the XPD spectrum (blue line) of amorphous BFO, deposited at room temperature, shows a relatively flat dispersion, with an overall modulation originating from the XPS attenuation for different electron take-off angles. Deposition on non-terminated STO substrate with an appropriate growth temperature still results in a nearly featureless XPD dispersion (grey line), with the appearance of peaks at 0° and 45° due to a partial ordering in the Bi cubic structure. Such result proves the capability of XPD as a tool for growth quality assessment, as it can catch

partial ordering and epitaxiality in the growth process. Similar results are obtained for the sample grown at RT and subsequently annealed at 550°C (green line), which shows a comparable long-range crystal order. Sample grown in a partial off-axis geometry on TiO_2 terminated STO (red line) still results in a disordered film (see Figure 4.6); however, a larger number of separated peaks can be seen in the XPD signal, as a results of the higher degree of film epitaxiality. Finally, in off-axis growth geometry (yellow line), a large number of XPD features, which show a good matching with the position of XPD peaks obtained from the STO substrate (black line), can be easily resolved, thus confirming the epitaxial growth.

In the case of fully epitaxial film, the XPD stereographic image (Figure 4.8 (b)) is also reported. Data have been collected in a 0°-90° azimuthal angle range and then symmetrized to obtain the full image. Such results are in a remarkable agreement with simulations for a simple BFO cubic structure (Fig.4.8 (c)), although bulk BFO display a rhombohedral structure [196] and orthorhombic reconstruction have been reported [195] in strained thin, epitaxial BFO/STO.

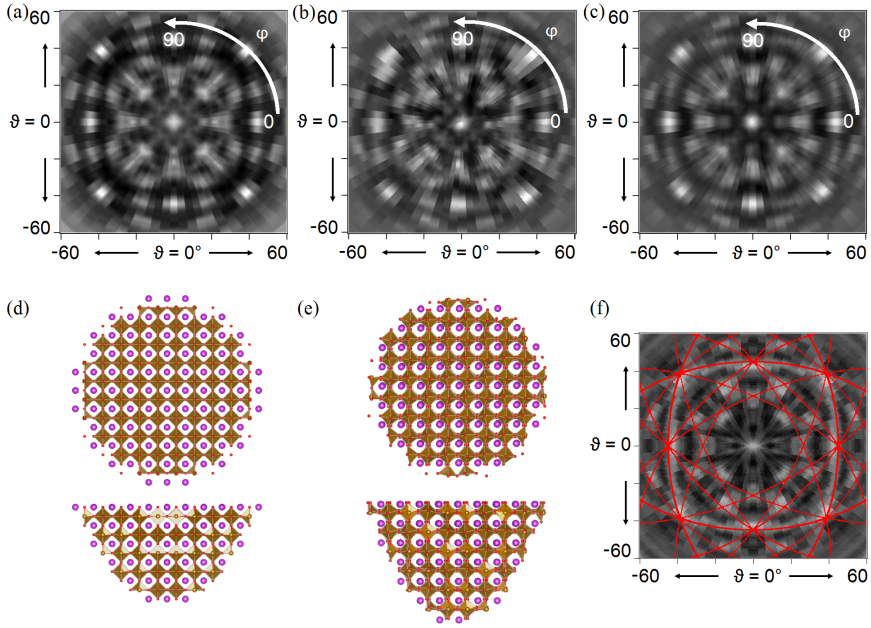

Figure 4.9: (a) Multiple scattering XPD calculations for the cubic BFO perovskite cluster shown in panel (d). (b) XPD calculation result for the rhombohedral BFO cluster shown in panel (e). (c) Simulation results of panel (b) after 4-fold symmetrization, carried out to mimic XPD results on multiple domain sample. (f) Main cubic perovskite Kikuchi arches (red lines) superimposed to experimental Bi 4f XPD image.

In order to analyze the effects of distortions within the thin films, simulations are performed also with a distorted cluster and are compared to the cubic case. The distorted cluster calculations (Figure 4.9 (b)) clearly shows strong asymmetries, as compared to cubic one (Figure 4.9 (a)); such deformations are typical of multiferroic materials and are linked to a specific ferroelectric domain orientation. In our case, the probing area is defined by the analyzer focus (1 mm^2) and thus, whenever present, several domains

could be measured simultaneously. Thus, a better approximation of expected data has been obtained by applying 8-fold symmetry to the calculated XPD image (Figure 4.9 (c)). A closer comparison of the two calculations (Figure 4.9 (a) and Figure 4.9 (c)) reveals small differences close to normal emission ($\theta = \pm 15°$), which could suggest a better agreement of the cubic structure simulation with the experimental data (Figure 4.9 (f)). However, by performing a proper least-square fitting procedure, it has not been possible to discriminate the two phases, due to additional features which become more evident at larger polar angles. For instance, superimposed to multiple scattering modulation, additional Kikuchi arches [131] are also observed. Such features, due to electron reflection on specific crystal planes, are expected in relatively high energy (≥ 1 keV) diffraction experiments. The predicted direction of Kikuchi arches in a cubic symmetry perovskite (red lines in Figure 4.9 (f)) are in perfect agreement with experimental data. The combination of the large probing area and the presence of Kikuchi features (only partly reproduced by the calculations) prevented in this case the discrimination of distorted and cubic structure; however, the applicability of XPD (even on a fixed azimuthal angle dispersion) as a tool for epitaxial order identification is still valid. Full phase discrimination could be feasible in thicker films, by performing a full 2π azimuthal angle dispersion on a single domain sample.

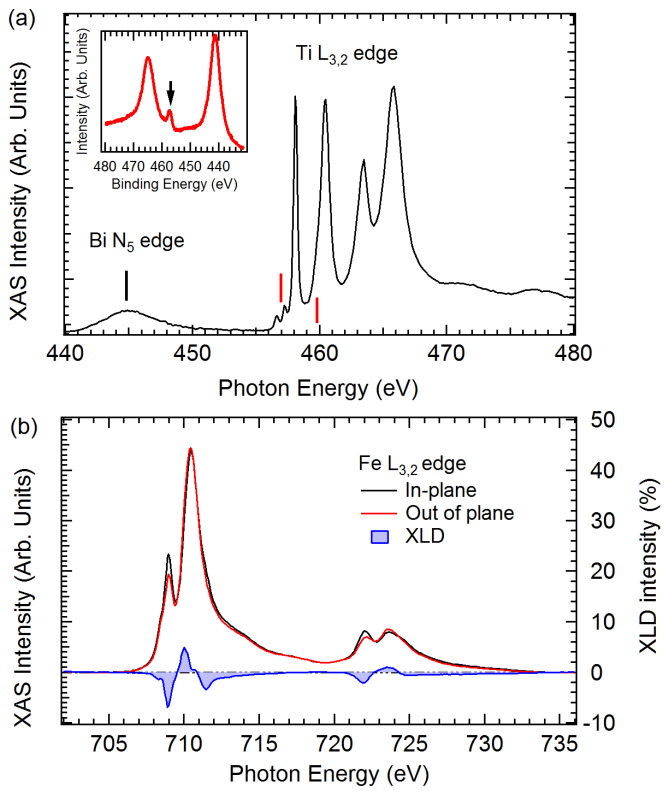

Figure 4.10: (a) XAS spectrum of Ti $L_{3,2}$ and Bi $N_{5,4}$ edges; red lines mark the expected positions for possible Ti^{3+} features. Inset: Bi 4d and Ti 2p (black arrow) XPS peaks. (b) XAS (left axis) and XLD (right axis) of Fe $L_{3,2}$ edge spectra for epitaxial $BiFeO_3$ thin film.

In STO based heterojunctions a typical proof of the presence of the 2DEG is given by small distortion of Ti 2p core-level photoemission spectrum [43]. In this case, however, Bi 4p core-level are superimposed to Ti 2p (Figure 4.10 (a), inset), preventing the application of this method. We resorted then to X-ray absorption spectroscopy (XAS) (Figure 4.10 (a)) to verify the oxidation state of Ti and Fe ions; Ti $L_{3,2}$ edge XAS spectrum is consistent with a completely oxidized Ti^{4+} state, with no obvious residual Ti^{3+} spectral features [43]. Fe $L_{3,2}$ edge is also consistent with the expected 3+ oxidation state. Moreover, a clear dichroism (XLD, Figure 4.10 (b)) is observed by switching from in plane to out of plane X-ray linear polarization; such result is consistent to previously reported results in BFO literature [212] and provides an additional proof of the epitaxial nature of the overlayer, since XLD can not be observed in disordered polycrystals.

The presence of the 2DEG can also be demonstrated by the analysis of in-gap structures probed by resonant photoemission (ResPES) measurements carried on the Ti $L_{3,2}$ edge [67]. However, the 4 nm thick films analyzed aren't suitable to such an accurate measurement, which require thinner films in order to fully take advantage of the resonance enhancement. Furthermore, the insulating behavior of $BiFeO_3$ induce a strong charge accumulation on the sample upon synchrotron irradiation, which induce a strong shift and broadening in the measured photoemission peaks, and can thus make more difficult to deal with the resonant photoemission analysis. The ResPES analysis of the elements constituent the films is still feasible, and a resonant photoemission study carried on the Fe $L_{3,2}$ edge is reported in Figure 4.11.

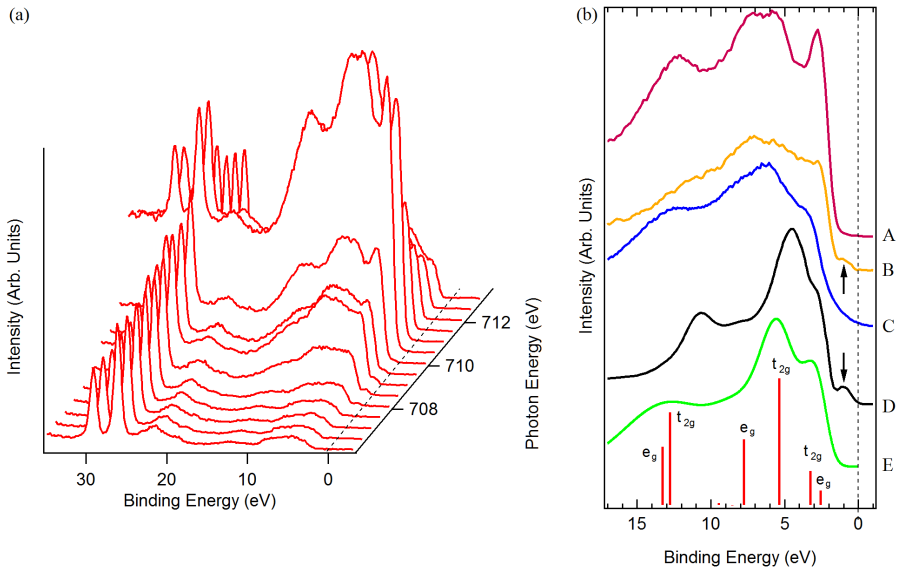

Figure 4.11: (a) Resonant photoemission analysis carried at the Fe $L_{3,2}$ edge with a horizontally polarized source on the valence band of the $BiFeO_3/SrTiO_3$ heterostructure. (b) Comparison between: A - On resonance valence band measured with a horizontally polarized source; B - Pre edge valence band measured with a horizontally polarized source; C - On resonance valence band measured with a vertically polarized source; D - Resonant photoemission study of the $FeTiO_3$ valence band, adapted from [213]; E - Refernce Fe^{3+} valence band spectrum with highlighted crystal field contributions, adapted from [214].

Resonant photoemission measurements of the valence band carried on the Fe $L_{3,2}$

edge show an enhancement of the e_g components for data collected with a horizontally polarized source respect to the vertically polarized one (Figure 4.11 (b)). Furthermore, the presence of a small feature near to the Fermi level in the pre-edge region suggests the presence of a Fe^{2+} contamination, since such a structure isn't predicted for a Fe^{3+} valence band spectrum [214]. This peculiar feature could be due to small intermixing phenomena, which can produce an ilmenite-like local coordination (characterized by a Fe^{2+} oxidation state) through the substitution between Fe and Sr at the interface. The small structure is indeed detected in the resonant photoemission analysis carried out on a $FeTiO_3$ sample [213].

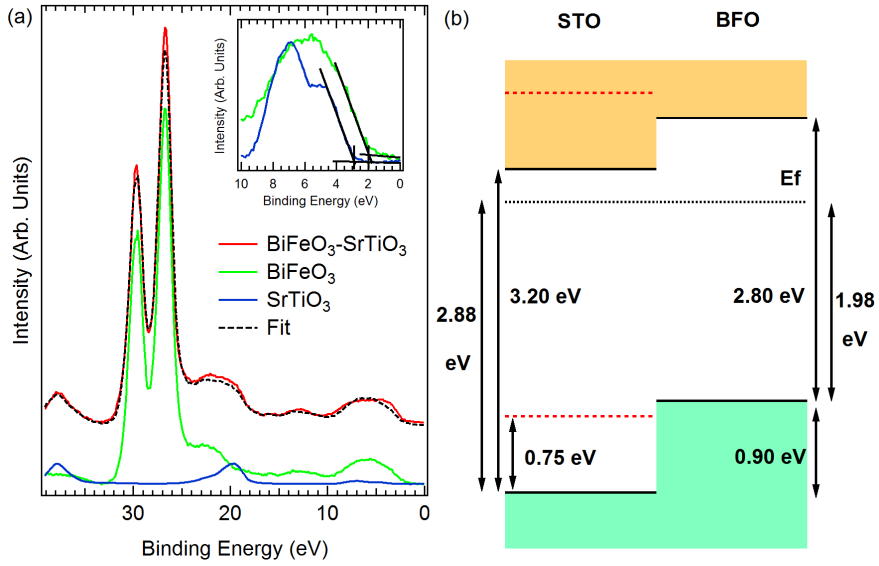

Figure 4.12: XPS analysis of the band alignment. (a): Linear combination of the $BiFeO_3$ and $SrTiO_3$ signals, which produces the fit (dashed line) of the signal of the $BiFeO_3/SrTiO_3$ heterointerface. Inset: detail of the normalized valence bands with measured VBM markers. (b): Resulting band alignment. The position of bare STO bands are reported for comparison (red dashed lines).

Finally, the band junction profile has been studied through XPS valence band analysis shown in Figure 4.12. In order to obtain the valence band maxima (VBM) shift, BFO/STO heterointerface valence band has been interpolated by the linear combination of thick (100 nm) polycrystalline BFO and clean STO spectra; the same method has been applied to LAO/STO case [43]. As a result, an accurate displacement map of occupied states position relative to the Fermi level can be obtained; the energy position of empty bands can then be estimated by considering the gap values reported in literature [215, 216]. In this case, the relative BFO/STO distance can be easily evaluated through the position of well-resolved core levels (Sr 4s, Bi $5d_{3/2}$ and Bi $5d_{5/2}$, at a binding energy of 38.0 eV, 29.7 eV and 26.7 eV, respectively). The resulting band alignment scheme is equivalent to the one measured on a $BiFeO_3$ film grown by PLD [86], which accordingly display the correct electronic properties.

It should be also noted that the deposition of epitaxial BFO results in a large displacement of STO VBM (0.75 eV) with respect to the bare STO surface (red dot lines in Figure 4.12 (b)). Such shift drives the substrate conduction band minimum closer to the Fermi

level and thus can ultimately favor the formation of a 2DEG. In fact, the same effect has been previously observed in LAO/STO and in other heterostructures, grown by PLD, CVD or sputtering [9]. However, in 2DEG system the conductive layer is matched by an additional STO conduction band notch crossing the Fermi level at the interface [43], which couldn't be probed by standard photoemission techniques. Thus, although the sign of the band shift is compatible with a scenario observed in conducting perovskite heterointerfaces, this band profile alone does not provide a proof of 2D conductivity.

4.5 Conclusions

In the first part of this chapter we report the successfully growth of $BiFeO_3$ over crystalline Si through the RF magnetron sputtering technique. Several thin films have been characterized with a large set of experimental probes. The optimal substrate temperature for the deposition is found to be 550°C; in this condition, a smooth, polycrystalline film is obtained, which shows both strong antiferromagnetism and piezoelectricity. Reported XAS spectra evidences small features that can be used to distinguish the $BiFeO_3$ from the similar Fe_2O_3 spectra. Moreover, the XPS analysis shown in this work allows to precisely evaluate the Bi:Fe stoichiometry ratio, which is usually a difficult experimental task. Temperature controlled growth is more reliable than room-temperature deposition followed by post-growth annealing, especially in terms of homogeneity, although a similar crystal order can be recovered. This inexpensive, repeatable and fast growth method can thus be suitable for large scale applications of $BiFeO_3$ in new devices.

In conclusion, in the second part of the chapter we proved the feasibility of high-quality epitaxial growth of $BiFeO_3$ thin films on $SrTiO_3$ by means of off-axis RF sputtering, suitable to interface investigation through photoelectron spectroscopy. Given the intrinsic difficulties in the use of typical growth characterization techniques such as RHEED, Raman and XRD, we resorted to AFM and photoemission to assess the growth quality. In particular, XPD has proven to be an extremely powerful technique for the determination of epitaxial character in ultrathin overlayer. In optimally grown samples, each photoelectron diffraction peak and Kikuchi bands can be easily measured, thus allowing us to recognize the sample as perfectly epitaxial; consistently, it is shown that RF sputtering can be tuned to grow ultrathin oxide heterostructures with a crystalline quality comparable to that displayed by laser-ablation techniques. X-ray absorption spectra confirm the expected Ti^{4+} and Fe^{3+} oxidation states. The valence band analysis of epitaxial films shows a strong shift of STO conduction band minimum towards the Fermi level, which could ultimately favor the appearance of 2D conductive states; such mechanism, which correspond to a strong n-type doping, can be recognized as a common feature [4] of perovskite epitaxial interfaces.

CHAPTER 5

Non-perovskite/$SrTiO_3$ interfaces: Al_2O_3/$SrTiO_3$ and CuO/$SrTiO_3$

5.1 Introduction

The discovery of a two-dimensional electron gas (2DEG) in the $LaAlO_3$/$SrTiO_3$ heterostructure [5] has triggered a wide search for interfaces capable to host a 2DEG, mainly perovskite-based heterojunctions [32]. However, the 2DEG was also found in the γ-Al_2O_3/$SrTiO_3$ interface [9], opening the possibility to found a 2DEG in structures where the top-most layer is not a perovskite. Furthermore, the growth of non-perovskite layers on $SrTiO_3$ can be exploited for the production of all-oxide photovoltaics [33] and photocatalysis system [3]. These applications are influenced by the heterostructure band alignment, which determines the carrier flow direction through the interface and possible charge confinement effects [27]. The growth of non-perovskite films on $SrTiO_3$ can thus provide ideas to engineer novel oxide heterojunctions.

In this chapter, two non-perovskite materials are studied, namely Al_2O_3 and CuO. For both these structures a growth and characterization analysis is reported, and the band alignment at the interface is discussed.

Al_2O_3 displays a wide band gap ($\approx$ 8.0 eV), and is thus commonly used in devices as an insulating layer material. Furthermore, the lattice parameter of γ-Al_2O_3 (7.911 Å) is approximately twice the one characteristic of $SrTiO_3$ (3.905 Å) [217], thus an epitaxial growth of a γ-Al_2O_3 layer on a $SrTiO_3$ substrate is easily achievable. The Al_2O_3/$SrTiO_3$ interface can host a 2DEG which is usually attributed to the formation of oxygen vacancies [90]. Such a 2DEG shows electron mobilities greater than those previously observed in perovskite-based heterojunctions, and a thickness-dependent insulator to metal transition similar to the one observed for the $LaAlO_3$/$SrTiO_3$ heterostructure is reported [9]. The polar properties of the Al_2O_3 layer should induce an interface polar discontinuity, and thus a built-in electric field and a potential gradient through the film. However, in the work of Schütz *et al.* [9] such a gradient was not observed. A bending of the $SrTiO_3$ bands which form a 600 meV deep potential well is still reported, and the presence of this notched structure enables the confinement of electrons within 3-5 unit cells under the interface.

The Al_2O_3 is mainly grown on $SrTiO_3$ by pulsed laser deposition (PLD) [9] [217] and atomic layer deposition (ALD) [90] [218]. The growth of Al_2O_3 on $SrTiO_3$ by RF sputtering has already been demonstrated in the work of Ueno *et al.* [219], where the film is used as a gate insulator for field effect transistor applications. An accurate interface analysis and band alignment for sputtered Al_2O_3/$SrTiO_3$ heterostructures is still lacking in literature. The first part of this chapter is then focused on the study of these topics.

Cupric oxide (CuO) shows many interesting properties, such as a transition from a paramagnetic to an antiferromagnetic phase at $\approx$ 230 K, and a spin reorientation at 212

K, which results in alternating Cu spins with an antiferromagnetic order along the $[10\bar{1}]$ cubic direction [220]. Furthermore, CuO is a promising material for the production of solar cells, because of its electrical and optical properties (band gap of 1.2-1.7 eV) [10]. Cupric oxide, differently from typical transition metal oxides, shows a monoclinic crystal structure [221], despite a tetragonal structure can be obtained upon epitaxial growth on a $SrTiO_3$ substrate [222]. This highly symmetric phase of CuO could show an interplay between the electron-phonon coupling and Jahn-Teller distortions [223]. Another important application of CuO is in photoelectrochemical water splitting, since the performance of the $CuO/SrTiO_3$ heterostructure is increased respect to that of similar heterostructures, such as $ITO/SrTiO_3$ and ITO/CuO junctions. In fact, due to improved conductivity, $CuO/SrTiO_3$ shows a superior photocurrent density and photoconversion efficiency respect to pristine materials [11].

In the second part of this chapter the growth and characterization of sputtered CuO thin films is discussed, where the final objective is the analysis of possible interface phenomena.

5.2 Experimental Details

The Al_2O_3 and CuO thin films have been grown by RF magnetron sputtering on Si (100) substrates for the calibration of deposition parameters, and on TiO_2-terminated STO (001) substrates for the interface analysis, from 2" sputtering targets. The sputtering power was 120 W for the depositions on Si and 80 W for the depositions on STO, with an Ar flux in the 1.9 - 2.3 sccm range and a 8.5 x 10^{-3} mbar pressure. Film crystallization has been achieved either with post-growth annealing in air and with in-growth direct heating. Good adhesion on Si substrate has been obtained through the removal of surface SiO_2 with in-vacuum high temperature flash annealing.

The STO TiO_2 termination has been achieved through HF buffered solution treatment, following the method described by Koster et al [177]. In order to trigger the epitaxial growth an off-axis deposition geometry has been selected, which reduces the resputtering mechanism and allows for a more homogeneous energy distribution of the deposited material [199, 200].

The XPS analysis has been performed with the Al K_α line (hν=1486.6 eV) of a non-monochromatized dual-anode PsP X-ray source and a VG Scienta R3000 electron analyzer operating in transmission mode. In X-ray photoelectron diffraction (XPD) measurements the angle between X-ray direction and analyzer axis is fixed at 55.4°. Single XPD spectra are collected by rotating the sample polar angle (θ) by step of 5°, exploiting the analyzer angular mode [193], which allows for the simultaneous acquisition of XPS data in a $\pm$10° range in the the polar direction. Full stereographic images are collected by performing single XPD spectra acquisition for various azimuthal angles (ϕ) in the -5°,95° range at step of 2.5° each.

Atomic force microscopy measurements have been collected by a NT-MDT Solver Pro instrument, operated in semi-contact mode. Micro Raman (μ-Raman) data have been collected with an In-Via confocal Renishaw microscope, with a lateral resolution of 1 μm at 100x magnification and a 633.3 nm He-Ne laser source.

The film growth and XPS, XPD, AFM and Raman analysis have been carried out at the Surface Science and Spectroscopy Laboratory of the Università Cattolica (Brescia, Italy).

5.3 Al_2O_3 on $SrTiO_3$

In order to calibrate the deposition parameters, such as the substrate temperature and the growth rate, the Al_2O_3 thin films have been initially grown on Si (100) substrates. Two films are grown, at room temperature (RT) and at 600°C respectively, and the film grown at 600°C is subsequently annealed in air at 750°C and 900°C. The film grown at RT is amorphous and shows no AFM features, while the annealing induces the formation of surface crystals (Figure 5.1), whose dimension increases with annealing temperature. The sample roughness is simultaneously slightly reduced (Table 5.1), probably due to the formation of overall flattened large crystals.

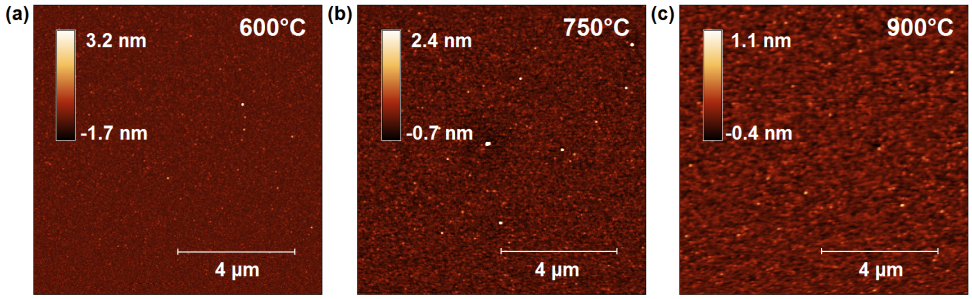

Figure 5.1: AFM topographic analysis carried out on Al_2O_3 films with different post-growth annealing temperatures ((a) 600°C, (b) 750°C, (c) 900°C). Each image covers an area of 10×10 μm.

Substrate	T (°C)	Roughness (± 0.01 nm)	Crystal Size (± 1 nm)	Al:O ratio	Thickness (± 0.1 nm)
Si	RT	-	amorphous	0.81	20
Si	600	0.24	40	0.86	20
Si	750	0.15	85	-	20
Si	900	0.14	104	0.89	20
$SrTiO_3$	600	0.06	-	0.43	1.7
$SrTiO_3$	600	0.10	-	0.12	0.4

Table 5.1: Sample list with the substrates and annealing temperatures considered; in the third and fourth column, average roughness and crystals average lateral size deduced from AFM (Figure 5.1 and 5.3) are summarized. For the samples grown on $SrTiO_3$ the crystal size is not reported since the films cover smoothly the $SrTiO_3$ terraces. In the fifth and last column, Al:O stoichiometry ratio and film thickness deduced by XPS analysis are reported.

Despite an highly ordered crystalline structure is usually preferable, the post-growth annealing induces an oxygen loss within the sample, as can be seen in the stoichiometry quantification reported in Table 5.1 and in the Al 2s and Al 2p XPS peaks shift (Figure 5.2), which increases for higher annealing temperatures. In fact, the presence of oxygen vacancies in the film can change slightly the charging effects of oxides under XPS irradiation, which produce the shift in XPS peaks position. It should be pointed out that the O 1s XPS peak used for the stoichiometry evaluation consists on a chemically bonded component and a part due to environmental oxygen contamination; the stoichiometry related to the bulk-like oxygen fraction is thus less than the quantity estimated in Table 5.1. Anyway, all the sample grown on Si show a strong excess of Al, since the stoichiom-

etry exceeds the 0.66 expected ratio.

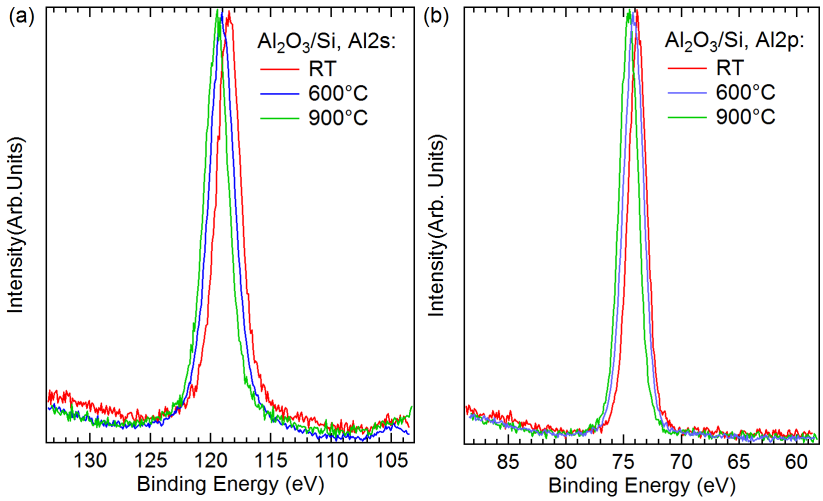

Figure 5.2: (a) Al 2s and (b) Al 2p XPS peak spectra. The spectra are normalized and aligned respect to the C 1s environmental contamination XPS peak. A pronounced peak shift can be observed when the annealing temperature is increased.

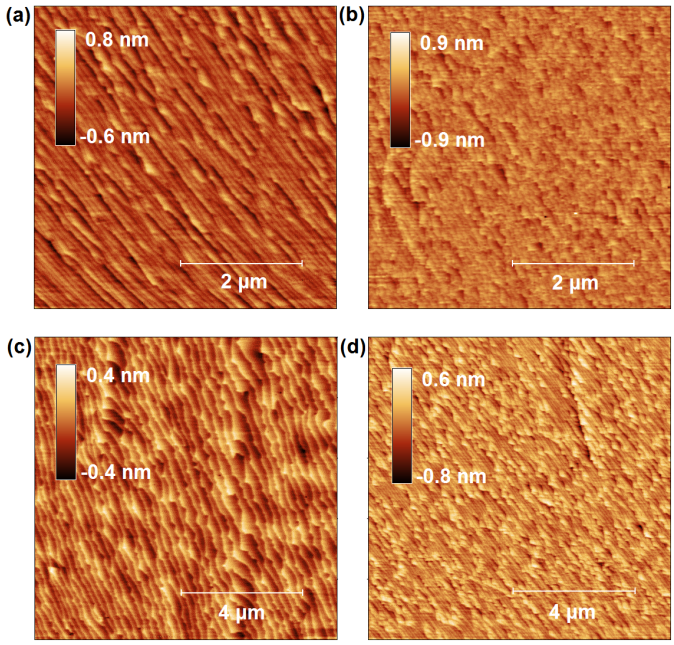

Figure 5.3: AFM topographic analysis carried out on: (a) $SrTiO_3$ (001) substrate, (b) and (d) Al_2O_3 films grown with a 1.7 nm film thickness, (c) Al_2O_3 films grown with a 0.4 nm film thickness. Image (a) and (b) cover an area of 5×5 μm, while image (c) and (d) cover an area of 10×10 μm.

In order to obtain a sample with both a good surface crystallinity and chemical stoichiometry we then deposited Al_2O_3 thin films on $SrTiO_3$ with a 600°C substrate temperature. The resulting films show an homogeneous growth along the $SrTiO_3$ substrate terraces (Figure 5.3), where the step length and height are maintained upon deposition ($\approx$ 100 nm and 3.8 $\pm$ 0.01 Å, respectively). The 0.4 nm-thick film shows many surface clusters which alter the step length, probably present because of an incomplete etching of the substrate surface. The films grown on $SrTiO_3$ show no more an excess of aluminum, but the presence of an oxygen component due to the $SrTiO_3$ substrate can invalidate the stoichiometry analysis. Indeed, the O 1s XPS peak characteristic of the 0.4 nm-thick film (not shown here) should be dominated by the $SrTiO_3$ contribution, and thus the stoichiometry quantification results in a poor Al:O ratio.

Both the films grown on $SrTiO_3$ show a good epitaxial growth since the XPD results, obtained from the tilt-induced variation of the Al 2p XPS peaks area (Figure 5.4 (b)), show a number of peaks comparable to the ones observed in the $SrTiO_3$ substrate signal. Furthermore, a Al_2O_3 film grown by atomic layer deposition (ALD) shows a nearly absent XPD signal, and this demonstrates the higher epitaxial order of Al_2O_3 films grown by RF sputtering.

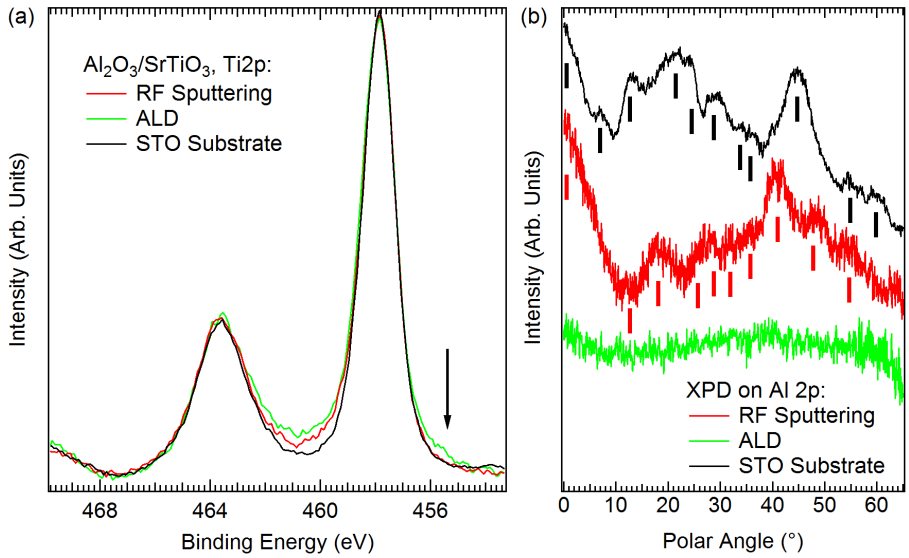

Figure 5.4: (a) Ti 2p XPS peak spectra, measured on the film grown by RF sputtering and on a film grown by ALD. A spectra measured on the $SrTiO_3$ substrate is reported as a reference. A black arrow marks the energy position where the Ti^{3+} states should arise. (b) XPD slice results, measured through the Al 2p XPS peaks on the film grown by RF sputtering and on a film grown by ALD. The XPD result obtained from the Sr 3d peaks of the STO substrate is reported as a reference. Measurements were performed with a fixed azimuthal angle ($\varphi = 0°$).

A spectroscopic signature for the possible presence of the 2DEG in a $SrTiO_3$-based heterostructure is the formation of Ti^{3+} oxidation states. These states can be probed in resonant photoemission measurements as in-gap features [43], and can be also observed as a small shoulder at lower binding energy in the Ti $2p_{3/2}$ standard XPS peak [54]. The Ti^{3+} feature can be barely seen in the sample grown by ALD (Figure 5.4 (a)), while the film grown by RF sputtering doesn't show any Ti^{3+} signal (is equivalent to the $SrTiO_3$

case). Thus RF sputtered films could thus be less suitable for the growth of heterostructure which can host the 2DEG as compared to ALD. A similar situation was observed by Dildar *et al.* [224] in sputtered $LaAlO_3/SrTiO_3$ heterostructures, where a set of deposition conditions suitable to produce a conductive interface wasn't found, and the junction could not be rendered conductive neither by post-annealing treatments.

Finally, the band alignment is reported in Figure 5.5. The valence band maxima (VBM) shift is obtained by the interpolation of the $Al_2O_3/SrTiO_3$ heterointerface valence band with the linear combination of thick (20 nm) polycrystalline Al_2O_3 and clean $SrTiO_3$ spectra. The energy position of conduction bands can then be evaluated by considering the gap values reported in literature. The type I band alignment is consistent with the one observed by Schütz et al. [9], while the valence band offset in our measurements is 0.29 eV, less than the 0.60 eV reported. This suggests that there can be many difference between the PLD-grown film and our film grown by RF-sputtering, possibly in crystal structure and strain.

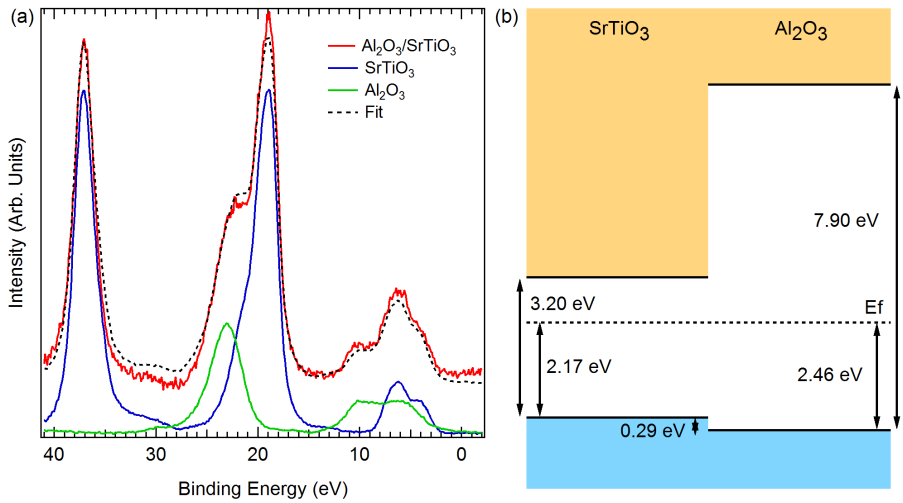

Figure 5.5: XPS analysis of the band alignment. (a): Linear combination of the Al_2O_3 and $SrTiO_3$ signals, which produces the fit (dashed line) of the signal of the $Al_2O_3/SrTiO_3$ heterointerface. (b): Resulting type I band alignment.

5.4 CuO on $SrTiO_3$

In order to obtain high-quality $CuO/SrTiO_3$ heterostructure we initially calibrated the deposition temperature through the growth of CuO films on silicon substrates, and then we grew a set of $CuO/SrTiO_3$ heterostructures with different film thickness (estimated by XPS analysis calibration). The AFM analysis reveals that the film grown at RT already displays many CuO clusters (Figure 5.6 (a)), which form a partially ordered polycrystalline structure when the film is grown with a substrate temperature of 600°C (Figure 5.6 (b)). For this film, the XPS analysis reveal an excess of Cu (Table 5.2), which is compatible with the formation of the Cu_2O compound. Thus a substrate temperature of 500°C is chosen for the deposition on STO, which enables a more homogeneous distribution of surface crystals (Figure 5.6 (c)). The high roughness and crystal size measured for the

films grown on Si decrease upon deposition on STO, and are further reduced for thinner films (Figure 5.6 (d-f)). Indeed, the 4.3 nm-thick film (hereafter labeled 'Thin', Figure 5.6 (e)) displays smaller crystals which start to displace homogeneously along the STO terraces, and an epitaxial CuO layer is obtained for the 2.7 nm-thick film (hereafter labeled 'Ultrathin', Figure 5.6 (f)).

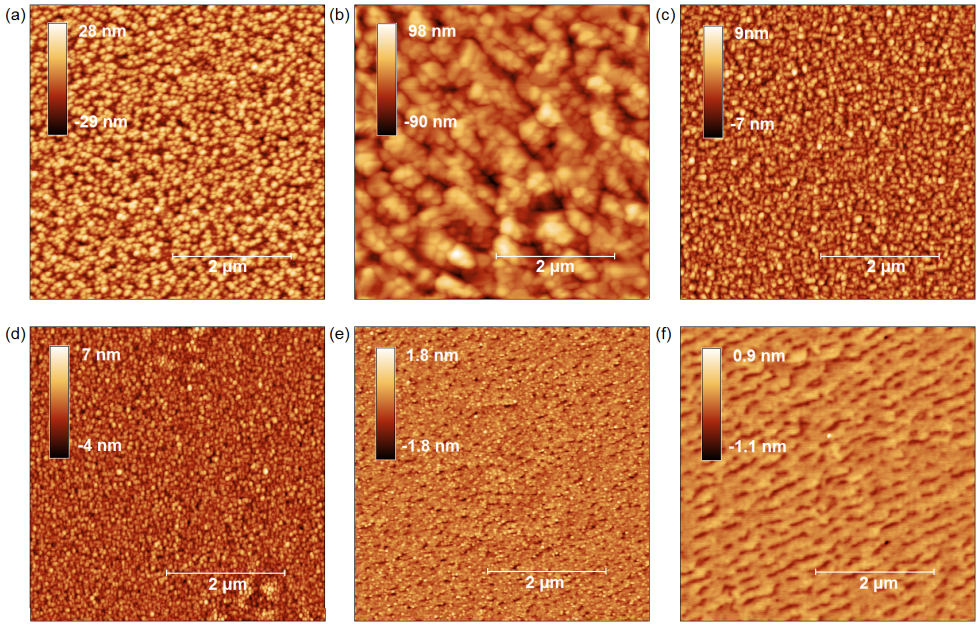

Figure 5.6: AFM topographic analysis carried out on CuO films with different growth conditions. (a) CuO grown on Si at RT. (b) CuO grown on Si at 600°C. (c-f) Films grown on STO at 500°C with decreasing film thickness (see Table 5.2). Each image covers an area of 5×5 μm.

Substrate	T (°C)	Roughness (± 0.01 nm)	Crystal Size (± 1 nm)	Cu:O Ratio	O_{2C} Ratio	Thickness (± 0.1 nm)
Si	RT	5.28	94	0.97	46%	110.0
Si	600	7.30	380	1.94	34%	110.0
$SrTiO_3$	500	0.85	59	1.36	27%	42.0
$SrTiO_3$	500	0.59	31	1.28	30%	18.0
$SrTiO_3$	500	0.18	11	1.27	21%	4.3
$SrTiO_3$	500	0.09	-	0.99	17%	2.7

Table 5.2: Sample list with the substrates and annealing temperatures considered; in the third and fourth column, average roughness and crystals average lateral size deduced from AFM (Figure 5.6) are summarized. For the ultrathin (2.7 nm) sample grown on $SrTiO_3$ the crystal size is not reported since the film covers smoothly the $SrTiO_3$ terraces. In the fifth and sixth column, data obtained from the XPS analysis is reported, namely Cu:O stoichiometry ratio and O_2 contamination (O_{2C}) percentage respect to the total O_2 peak area. In the last column film thickness deduced by XPS analysis is reported for each sample.

The stoichiometry is improved upon deposition of thinner films, with a Cu:O ratio approaching the 1:1 expected value. The obtained ratio is however strictly related to

the possible presence of O_2 environmental contamination. In this case, XPS can be used for the quantification of the O_2 contamination percentage with respect to the total O_2 content (Table 5.2), as the contamination produces an additional XPS peak at higher binding energies (Figure 5.7 (a)), which can be separated from the component involved in chemical bonding through a simple peak fitting procedure. Despite the contamination content is reduced for thinner films, the Cu:O ratio measured is not totally accurate, since part of the O 1s peak area is due to the oxygen present in the $SrTiO_3$ substrate.

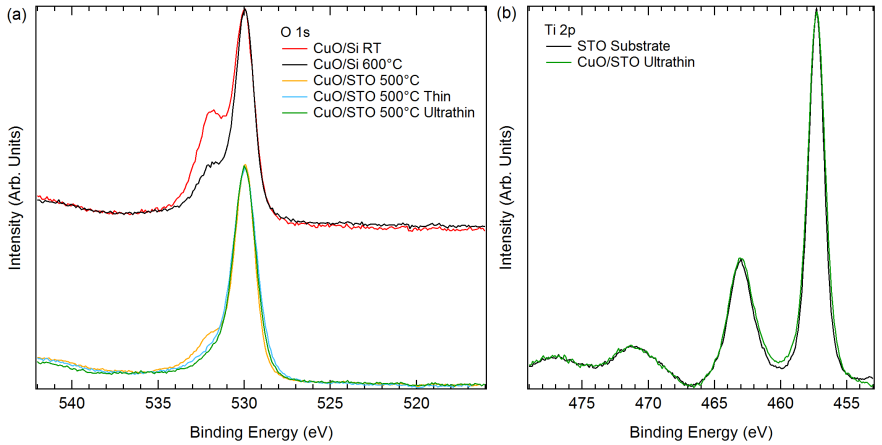

Figure 5.7: (a) O 1s spectra collected for different CuO films grown on Si and $SrTiO_3$ substrates. (b) Ti 2p XPS peak spectra, measured for the thinner film and for the $SrTiO_3$ substrate.

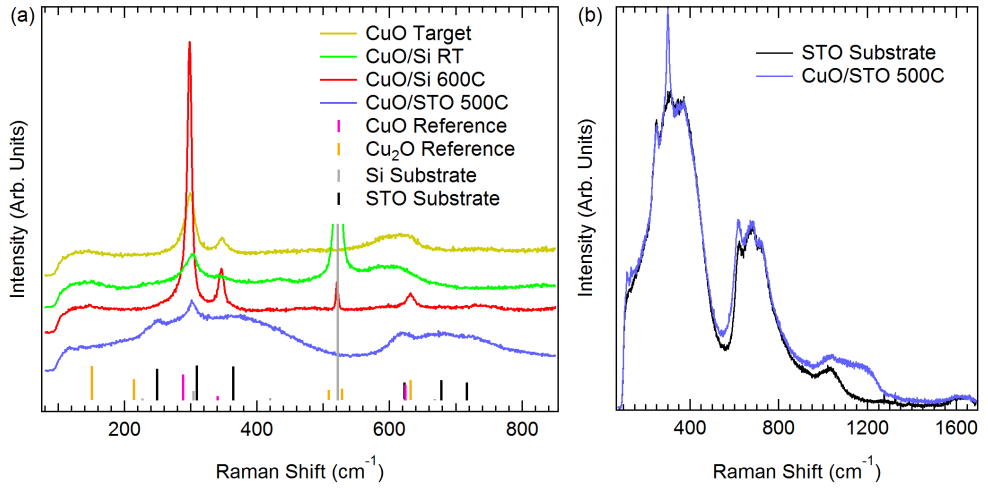

Figure 5.8: (a) μ-Raman spectra collected from CuO thick films grown on Si and on $SrTiO_3$; predominant features are marked in pink (CuO), orange (Cu_2O), grey (Si) and in black ($SrTiO_3$). Raman spectrum collected from the CuO sputtering target is reported as a reference. Reference peak position for CuO and Cu_2O spectra are adapted from [225]. (b) Comparison between μ-Raman spectra collected from the CuO/$SrTiO_3$ heterostructure and from the $SrTiO_3$ substrate.

The substrate XPS peaks can be really useful for the analysis of interface properties, since the presence of a 2DEG is usually related to the formation of Ti^{3+} states in the Ti 2p XPS spectrum. Such states are however unobserved in our samples, and the peaks shape suggest a completely oxidized Ti^{4+} interface (Figure 5.7 (b)).

The absence of impurity inclusions within the CuO films is studied by Raman spectroscopy (Figure 5.8 (a)). The Raman spectrum of the target used for the sputtering deposition is consistent with the CuO Raman peaks available in literature [225], and the deposition of CuO on Si results in a similar spectrum, with the addition of new peaks related to the substrate. The film grown on Si at 600°C shows a reduced signal arising from the substrate, but a new peak arises at $\approx 640\ cm^{-1}$, consistent with the formation of Cu_2O inclusions predicted by XPS quantification. Finally, the growth of a CuO thick film on $SrTiO_3$ shows a Raman spectrum which is dominated by features related to the $SrTiO_3$ substrate. However in the direct comparison between spectra collected from the $CuO/SrTiO_3$ heterostructure and from the $SrTiO_3$ substrate (Figure 5.8 (b)) a few differences arise, which can be ascribed to the deposition of a CuO film without Cu_2O inclusions. The chemical composition analysis of the deposited thin films must however be further analyzed by XPS measurements.

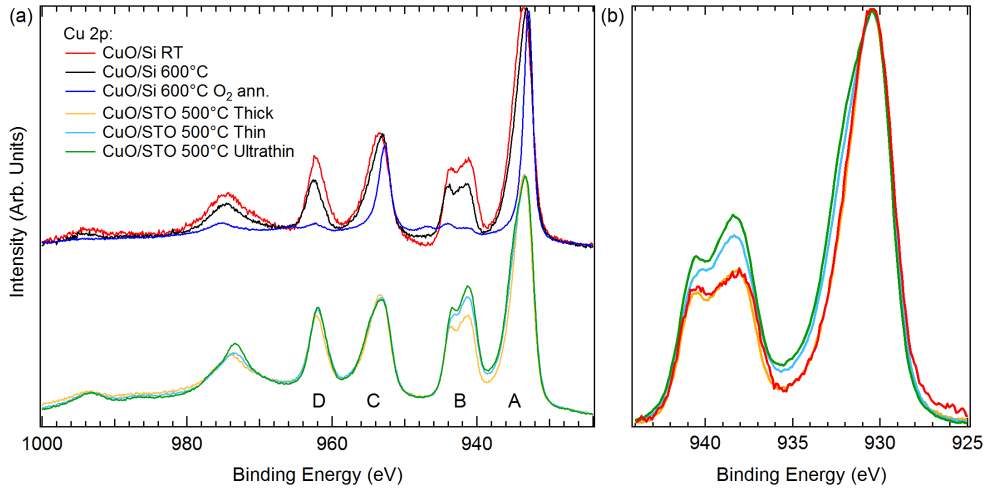

Figure 5.9: (a) Cu 2p spectra collected for different CuO films grown on Si and $SrTiO_3$ substrates. (b) Detail of the changes in intensity and shape of the Cu $2p_{3/2}$ XPS peak spectra, collected from films grown on $SrTiO_3$ substrates with different thickness. For quantification details see Table 5.3.

The Cu 2p XPS peak analysis (Figure 5.9 (a)) confirm that the growth of CuO at 600°C produces a Cu_2O impurity inclusion, since the overall peak shape is comparable with the Cu 2p XPS spectra characteristic of Cu_2O [226]. The annealing of this sample at $\approx$ 450°C in oxygen atmosphere ($p_{O2} = 1 \times 10^{-6} mbar$) enhances further the Cu_2O contribution, resulting in a flattening of the charge-transfer peaks. The off-axis sputtering deposition of CuO on $SrTiO_3$ at 500°C results in a spectrum shape and peaks intensity similar to the one observed for the film grown at room temperature. However, the growth of thinner films (Figure 5.9 (b)) affects the charge-transfer contribution and change the distance between satellites (B) and main lines (A, Table 5.3). The measured value of ΔE (peak distance) and I_A/I_B (peak intensity ratio) can be used to determine the Coulomb inter-

action Q, the energy distance between unhybridized one-hole states (Δ) and the mixing matrix element of the Hamiltonian (T, Figure 5.10) [227]. These parameters can be used for the evaluation of the energy gap (E_g) characteristic of the system as E_g scales with Δ [228]. This analysis results in a gap which increases of about 0.2 eV as the film thickness decreases.

Thickness ($\pm$ 0.1 nm)	I_A/I_B	ΔE (eV)	Δ (eV)	Q (eV)
42.0	2.3	8.07	1.28	8.00
4.3	1.9	7.81	1.43	7.98
2.7	1.7	7.71	1.47	8.02

Table 5.3: Variation of the peak intensity and position for CuO films grown on $SrTiO_3$ with different film thickness, as evaluated from the XPS analysis (Figure 5.9 (b)). The sum of the intensity of the two peaks at $\approx$ 930 eV (I_A) is compared to the one of the two peaks at $\approx$ 940 eV (I_B). The area-weighted average of the two peak position at at $\approx$ 930 eV is compared to the one of the peaks at $\approx$ 940 eV in order to obtain the distance ΔE. Resulting values for Coulomb interaction Q and energy distance between unhybridized one-hole states (Δ) are also reported.

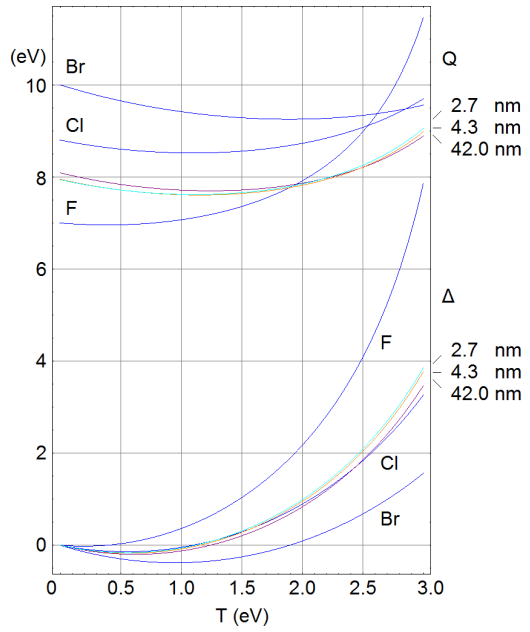

Figure 5.10: Variation of the Coulomb interaction Q and of the energy distance between unhybridized one-hole states (Δ) respect to the mixing matrix element of the Hamiltonian (T), plotted using experimental values of ΔE and I_A/I_B. Values obtained from copper dihalides, plotted in blue, are adapted from [227]. Values for 2.7 nm, 4.3 nm and 42.0 nm thick films are plotted in light blue, red and violet respectively.

The epitaxial order of CuO films is probed by X-ray photoelectron diffraction (XPD) measurements (Figure 5.11 (a)). The XPD spectrum of the thick film grown on Si at 600°C shows a featureless background produced by the intensity attenuation of XPS peaks with

the increase of tilt angle. The growth on a $SrTiO_3$ substrate triggers the appearance of XPD peaks, even for the thickest sample ($\approx$ 42 nm), which is less intense due to the higher roughness (see Table 5.2). This result, combined with AFM images, demonstrate the deposition of high-quality and epitaxial CuO films by RF sputtering. Full stereographic images have been acquired both for Cu 2p and Sr 3d XPS peaks, which give information about the film and the substrate, respectively. A detailed analysis reveal that the structure of the CuO film can't be monoclinic, because a XPD peak arises at $\phi = 45°$. A cubic reconstruction is also excluded, since the peak which arises at $\theta \approx 45°$ in the Sr 3d stereographic pattern (Figure 5.11 (b), yellow marker), characteristic of a cubic phase, show a different θ position for the Cu 2p image (Figure 5.11 (c), yellow marker). The CuO film is thus in a tetragonal phase, and the difference in the feature at $\theta \approx 45°$ suggest a unit cell with a square base area of 3.9x3.9 Å, and an unit cell height of $\approx$ 5.7 Å.

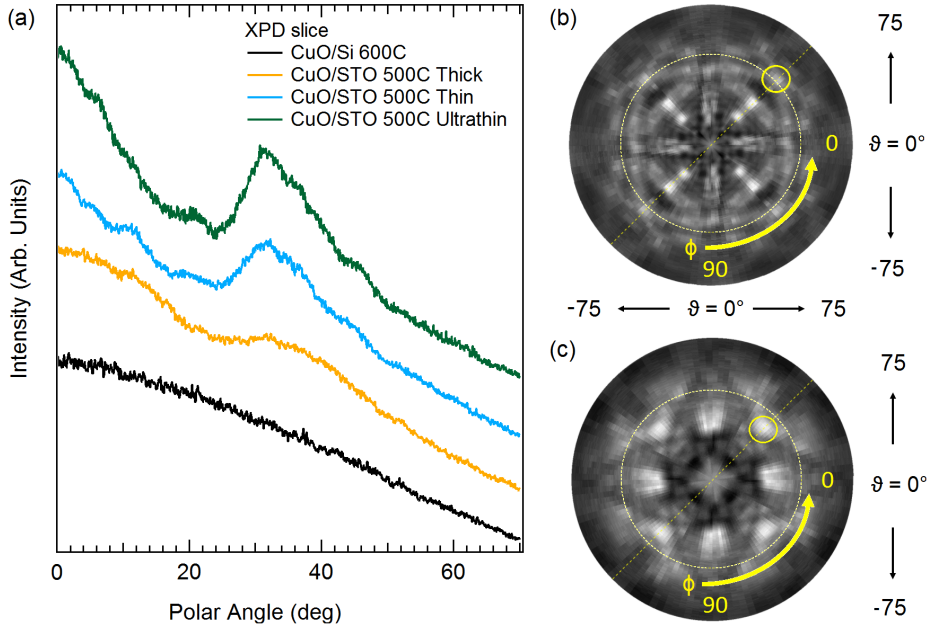

Figure 5.11: (a) XPD analysis of Cu 2p XPS peak area from a CuO/$SrTiO_3$ heterostructure for different film thickness. The spectra are collected by sweeping the sample polar angle in the (010) substrate plane, with a fixed azimuthal angle ($\varphi = 0°$). (b) Full stereographic images obtained from the Sr 3d XPS peak analysis. (c) Full stereographic images obtained from the Cu 2p XPS peak analysis.

Finally, the band alignment at the CuO/$SrTiO_3$ interface is analyzed. The valence band maxima (VBM) are obtained by fitting the valence band spectrum of the heterojunction with the linear combination of the spectra characteristic of pristine parent compounds, which allow a fine alignment of their relative energy position (Figure 5.12 (a)). The evaluation of the VBM for the CuO thick film is strongly influenced by a small shoulder near the Fermi edge which is still ascribable to the CuO film. Indeed such a structure doesn't display a sharp drop in intensity, so the determined leading edge position display an uncertainty of $\pm$ 0.15 eV. Taking into account this uncertainty and the possible variation of energy gap with film thickness, the conduction band (CB) of CuO can be

almost aligned to the CB of the $SrTiO_3$ substrate, and the band alignment results always in a Type I junction.

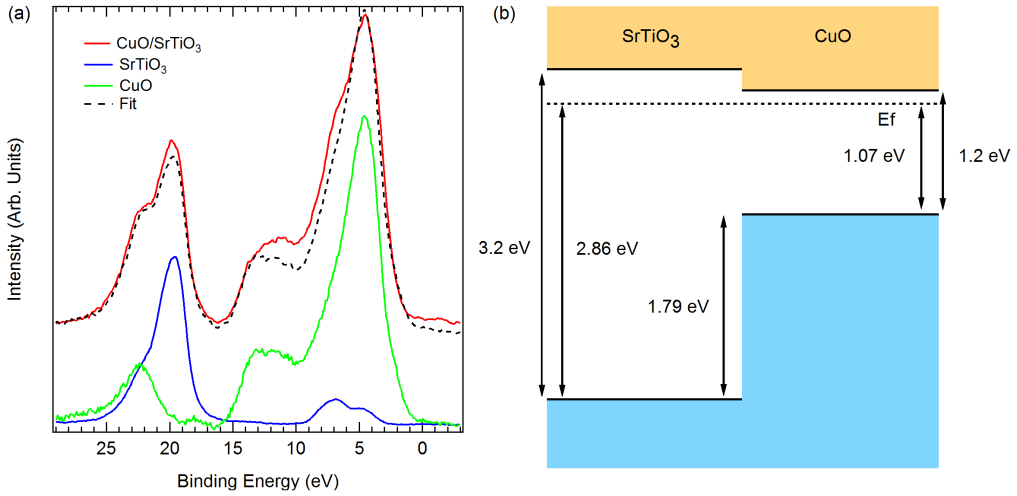

Figure 5.12: XPS analysis of the band alignment. (a): Linear combination of the CuO and $SrTiO_3$ signals, which produces the fit (dashed line) of the signal of the $CuO/SrTiO_3$ heterointerface. (b): Resulting type I band alignment.

5.5 Conclusions

In conclusion, we demonstrated the epitaxial growth of Al_2O_3 and CuO thin films on $SrTiO_3$ by RF sputtering, both by AFM and XPD analysis. Films with a good stoichiometry, as probed by XPS analysis, have been obtained for both materials. In particular, annealing in air of Al_2O_3 films results in oxygen deficient samples, thus a direct annealing during deposition is preferable. For CuO, a deposition temperature of 600°C induce the formation of Cu_2O inclusions, as probed by μ-Raman and XPS analysis. In XPS measurements the Ti^{3+} features, which are usually related to the formation of a 2DEG, aren't observed for either sample. The band alignment at the interface is reported for both heterostructures, and a type I band alignment is observed in both cases. The higher conduction band maxima of Al_2O_3 respect of $SrTiO_3$ can trigger the confinement of a 2DEG within the substrate, while the $CuO/SrTiO_3$ junction suggest a possible confinement of mobile charge within the CuO film. Also, for heterostructures which host the 2DEG a low valence band offset is usually observed, and the high (1.79 eV) VBO at the $CuO/SrTiO_3$ interface further suggests an unlikely 2DEG formation.

Conclusions

In this work we demonstrated the possibility to grow high-quality epitaxial oxide films on $SrTiO_3$ substrates by RF sputtering. The epitaxial growth is analyzed both by AFM topographic images and XPD results. Indeed, XPD has proven to be an extremely powerful technique for the determination of epitaxial character in ultrathin overlayers. The possible defect doping mechanism of the $SrTiO_3$ substrate by annealing and sputtering are discussed, and the formation of in-gap states, along with a strong Ti^{3+} oxidation is reported. The growth of $BiFeO_3$ by RF sputtering is strongly dependent on deposition temperature, and an homogeneous, smooth and polycrystalline film is obtained for a substrate temperature of $550°C$. Furthermore, the films show the correct stoichiometry and multiferroic properties. For the growth on $SrTiO_3$, a small Fe^{2+} inclusion is detected by resonant photoemission measurements, which is probably related to intermixing phenomena, which can produce an ilmenite-like local coordination. For all the grown materials, temperature controlled growth is more reliable than room-temperature deposition followed by post-growth annealing, especially in terms of homogeneity. Furthermore, the post-growth annealing induces the formation of oxygen defects in Al_2O_3 films. $BiFeO_3$, Al_2O_3 and tetragonal CuO films are thus grown epitaxially on $SrTiO_3$ by the employment of off-axis sputtering geometry. Ti^{3+} oxidation state features, which are the signature of the presence of a 2DEG at the interface, aren't detected in either heterostructure analyzed. RF sputtered films could thus be less suitable for the growth of heterostructure which can host the 2DEG compared to ALD or PLD. Despite conductivity is not directly evaluated for our samples, this situation may confirm the observations of Dildar et al. [224], where sputtered $LaAlO_3/SrTiO_3$ heterostructures were not conductive and could not be rendered conductive by post-annealing treatments. The band alignment at the obtained oxide heterojunction show that the deposition of $BiFeO_3$ and CuO films results in a large displacement of STO VBM (0.75 eV) with respect to the bare STO surface. Such shift drives the substrate conduction band minimum closer to the Fermi level and thus can ultimately favor the formation of a 2DEG, since a notched structure which crosses the Fermi level can arise in 2DEG-based interfaces. The absence of such a shift can be one of the sources for the absence of conductivity and Ti^{3+} states in sputtered Al_2O_3 films. Usually, in conductive oxide interfaces the 2DEG is confined in the $SrTiO_3$ substrate, which is related to a lower conduction band minimum in the $SrTiO_3$ side with respect to the overlayer. The opposite situation measured, and the high (1.79 eV) VBO at the $CuO/SrTiO_3$ interface suggest an unlikely 2DEG formation in this heterostructure. The band offset within $CuO/SrTiO_3$ are however strongly dependent on the thickness of the films, since the band gap can vary of ± 0.2 eV, and a completely different band alignment may arise when thinner films are considered. The presence

of a 2DEG at the $BiFeO_3/SrTiO_3$ interface cannot instead be discriminated by the band alignment alone.

Possible future directions are related to the growth of electrical contacts at the interface between $SrTiO_3$ and the overlayer. Transport measurements are indeed needed in order to demonstrate the presence of a 2DEG at the interface, and to verify the possibility to obtain a conductive interface also in heterostructures grown by RF sputtering. Upon detection of a 2DEG further synchrotron-based measurements would be needed for the analysis of in-gap states. This analysis would need high quality ultrathin films ($\approx$ 1-2 nm) in order to fully take advantage of the Ti resonance at substrate states. The final step of this research would be the production of novel multifunctional applications, such as $BiFeO_3$-based devices where the 2DEG properties could in principle be tuned by the application of external electric or magnetic fields.

Bibliography

[1] C. Cen, S. Thiel, J. Mannhart, and J. Levy. Oxide nanoelectronics on demand. *Science*, 323:1026–1030, 2009.

[2] Y. S. Lee, D. Chua, R. E. Brandt, S. C. Siah, J. V. Li, J. P. Mailoa, S. W. Lee, R. G. Gordon, and T. Buonassisi. Atomic layer deposited gallium oxide buffer layer enables 1.2 v open-circuit voltage in cuprous oxide solar cells. *Adv. Mater.*, 26:4704–4710, 2014.

[3] Y. Mi and Y. Weng. Band alignment and controllable electron migration between rutile and anatase TiO_2. *Scientific Reports*, 5:11482, 2015.

[4] U. Treske, N. Heming, M. Knupfer, B. Büchner, E. Di Gennaro, A. Khare, U. Scotti Di Uccio, F. Miletto Granozio, S. Krause, and A. Koitzsch. Universal electronic structure of polar oxide hetero-interfaces. *Sci. Rep.*, 5:14506, 2015.

[5] A. Ohtomo and H. Y. Hwang. A high-mobility electron gas at the $LaAlO_3/SrTiO_3$ heterointerface. *Nature*, 427:423–426, 2004.

[6] A. Janotti, L. Bjaalie, B. Himmetoglu, and Van de Walle C. G. Band alignment at band-insulator/mott-insulator interfaces. *Phys. Status Solidi RRL*, 8:577–582, 2014.

[7] S. A. Chambers, T. C. Kaspar, A. Prakash, G. Haugstad, and B. Jalan. Band alignment at epitaxial $BaSnO_3/SrTiO_3$ (001) and $BaSnO_3/LaAlO_3$ (001) heterojunctions. *Appl. Phys. Lett.*, 108:152104, 2016.

[8] H. Yan, H. Deng, N. Ding, J. Hea, L. Peng, L. Sun, P. Yang, and J. Chu. Influence of transition elements doping on structural, optical and magnetic properties of $BiFeO_3$ films fabricated by magnetron sputtering. *Mater. Lett.*, 111:123–125, 2013.

[9] P. Schütz, F. Pfaff, P. Scheiderer, Y. Z. Chen, N. Pryds, M. Gorgoi, M. Sing, and R. Claessen. Band bending and alignment at the spinel/perovskite γ-$Al_2o_3/SrTiO_3$ heterointerface. *Phys. Rev. B*, 91:165118, 2015.

[10] M. Kawwam, F. Alharbi, A. Aldwayyan, and K. Lebbou. Morphological study of PLD grown CuO films on $SrTiO_3$, sapphire, quartz and MgO substrates. *Applied Surface Science*, 258:9949–9953, 2012.

[11] S. Choudhary, A. Solanki, S. Upadhyay, N. Singh, V. R. Satsangi, R. Shrivastav, and S. Dass. Nanostructured $CuO/SrTiO_3$ bilayered thin films for photoelectrochemical water splitting. *J Solid State Electrochem*, 17:2531–2538, 2013.

[12] G. Koster, M. Huijben, and G. Rijnders. *Epitaxial Growth of Complex Metal Oxides*. Woodhead Publishing, 2015.

[13] A. Ohtomo, D. A. Muller, J. L. Grazul, and H. Y. Hwang. Artificial charge-modulation in atomic-scale perovskite titanate superlattices. *Nature*, 419:378, 2002.

[14] H. Y. Hwang, Y. Iwasa, M. Kawasaki, B. Keimer, N. Nagaosa, and Y. Tokura. Emergent phenomena at oxide interfaces. *Nature Materials*, 11:103, 2012.

[15] S. Thiel, G. Hammerl, A. Schmehl, C. W. Schneider, and J. Mannhart. Tunable quasi-two-dimensional electron gases in oxide heterostructures. *Science*, 313:1942–1945, 2006.

[16] N. Reyren, S. Thiel, A. D. Caviglia, L. Fitting Kourkoutis, G. Hammer, C. Richter, C. W. Schneider, T. Kopp, A. S. Retschi, D. Jaccard, M. Gabay, D. A. Muller, J. M. Triscone, and J. Mannhart. Superconducting interfaces between insulating oxides. *Science*, 317:1196, 2007.

[17] A. Brinkman, M. Huijben, M. Van Zalk, J. Huijben, U. Zeitler, J. K. Maan, W. G. Van der Wiel, G. Rijnders, D. H. A. Blank, and H. Hilgenkamp. Magnetic effects at the interface between nonmagnetic oxides. *Nature Materials*, 6:493, 2007.

[18] M. Huijben, A. Brinkman, G. Koster, G. Rijnders, H. Hilgenkamp, and D. H. A. Blank. Structure-property relation of $SrTiO_3/LaAlO_3$ interfaces. *Adv. Mat.*, 21:1665, 2009.

[19] Z. Q. Liu, C. J. Li, W. M. Lü, H. Huang, Z. Huang, S. W. Zeng, X. P. Qiu, L. S. Huang, A. Annadi, J. S. Chen, J. M. D. Coey, T. Venkatesan, and Ariando. Origin of the two-dimensional electron gas at $LaAlO_3/SrTiO_3$ interfaces: The role of oxygen vacancies and electronic reconstruction. *Phys. Rev. X*, 3:021010, 2013.

[20] L. Qiao, W. Li, H. Xiao, H. M. Meyer, X. Liang, N. V. Nguyen, W. J. Weber, and M. D. Biegalski. Electronic structure and band alignment at an epitaxial spinel/perovskite heterojunction. *ACS Applied Materials and Interfaces*, 6:14338–14344, 2014.

[21] E. Assmann, P. Blaha, R. Laskowski, K. Held, S. Okamoto, and G. Sangiovanni. Oxide heterostructures for efficient solar cells. *Phys. Rev. Lett.*, 110:078701, 2013.

[22] H. L. Lu, Z. M. Liao, L. Zhang, W. T. Yuan, Y. Wang, X. M. Ma, and D. P. Yu. Reversible insulator-metal transition of $LaAlO_3/SrTiO_3$ interface for nonvolatile memory. *Scientific Reports*, 3:2870, 2013.

[23] S. Wu, S. X. Luo, Turner, H. Peng, W. Lin, J. Ding, A. David, B. Wang, G. Van Tendeloo, J. Wang, and T. Wu. Nonvolatile resistive switching in $Pt/LaAlO_3/SrTiO_3$ heterostructures. *Phys. Rev. X*, 3:041027, 2013.

[24] C. W. Bark, P. Sharma, Y. Wang, S. H. Baek, S. Lee, S. Ryu, C. M. Folkman, T. R. Paudel, A. Kumar, S. V. Kalinin, A. Sokolov, E. Y. Tsymbal, M. S. Rzchowski, A. Gruverman, and C. B. Eom. Switchable induced polarization in $LaAlO_3/SrTiO_3$ heterostructures. *NanoLetters*, 12:1765, 2012.

[25] A. Kumar, T. M. Arruda, Y. Kim, I. N. Ivanov, S. Jesse, C. W. Bark, N. C. Bristowe, E. Artacho, P. B. Littlewood, C. B. Eom, and S. V. Kalinin. Probing surface and bulk electrochemical processes on the $LaAlO_3/SrTiO_3$ interface. *ACS Nano*, 6:3841, 2012.

[26] S. M. Sze and K. K. Ng. *Physics of Semiconductor Devices*. Wiley-Interscience, 2007.

[27] M. Lallart. *Ferroelectrics - Characterization and Modeling*. InTech, 2011.

[28] T. Yajima, Y. Hikita, M. Minohara, C. Bell, J. A. Mundy, L. F. Kourkoutis, D. A. Muller, H. Kumigashira, M. Oshima, and H. Y. Hwang. Controlling band alignments by artificial interface dipoles at perovskite heterointerfaces. *Nat. Commun.*, 6:6759, 2015.

[29] J. D. Burton and E. Y. Tsymbal. Evolution of the band alignment at polar oxide interfaces. *Phys. Rev. B*, 82:161407(R), 2010.

[30] G. Conti, A. M. Kaiser, A. X. Gray, S. Nemšák, G. K. Pálsson, J. Son, P. Moetakef,

A. Janotti, L. Bjaalie, C. S. Conlon, D. Eiteneer, A. A. Greer, A. Keqi, A. Rattanachata, A. Y. Saw, A. Bostwick, W. C. Stolte, A. Gloskovskii, W. Drube, S. Ueda, M. Kobata, K. Kobayashi, C. G. Van de Walle, S. Stemmer, C: M. Schneider, and C. S. Fadley. Band offsets in complex-oxide thin films and heterostructures of $SrTiO_3/LaNiO_3$ and $SrTiO_3/GdTiO_3$ by soft and hard X-ray photoelectron spectroscopy. *J. Appl. Phys.*, 113:143704, 2013.

[31] G. Berner, A. Müller, F. Pfaff, J. Walde, C. Richter, J. Mannhart, S. Thiess, A. Gloskovskii, W. Drube, M. Sing, and R. Claessen. Band alignment in $LaAlO_3/SrTiO_3$ oxide heterostructures inferred from hard x-ray photoelectron spectroscopy. *Phys. Rev. B*, 88:115111, 2013.

[32] L. Bjaalie, B. Himmetoglu, L. Weston, A. Janotti, and C. G. Van de Walle. Oxide interfaces for novel electronic applications. *New J. Phys.*, 16:025005, 2014.

[33] Y. S. Lee, D. Chua, R. E. Brandt, S. C. Siah, J. V. Li, J. P. Mailoa, S. W. Lee, R. G. Gordon, and T. Buonassisi. Atomic layer deposited gallium oxide buffer layer enables 1.2 v open-circuit voltage in cuprous oxide solar cells. *Adv. Mater.*, 26:4704–4710, 2014.

[34] G. P. Schwartz, M. S. Hybertsen, J. Bevk, R. G. Nuzzo, J. P. Mannaerts, and G. J. Gualtieri. Core-level photoemission measurements of valence-band offsets in highly strained heterojunctions: Si-Ge system. *Phys. Rev. B*, 39:1235–1241, 1989.

[35] V. Stevanović, K. Hartman, R. Jaramillo, S. Ramanathan, T. Buonassisi, and P. Graf. Variations of ionization potential and electron affinity as a function of surface orientation: The case of orthorhombic SnS. *Appl. Phys. Lett.*, 104:211603, 2014.

[36] R. B. Comes, P. Xu, B. Jalan, and S. A. Chambers. Band alignment of epitaxial $SrTiO_3$ thin films with $(LaAlO_3)_{0.3}$-$(Sr_2AlTaO_6)_{0.7}$ (001). *Appl. Phys. Lett.*, 107:131601, 2015.

[37] P. R. Brown, D. Kim, R. R. Lunt, N. Zhao, M. G. Bawendi, J. C. Grossman, and V. Bulović. Energy level modification in lead sulfide quantum dot thin films through ligand exchange. *ACS Nano*, 8:5863–5872, 2014.

[38] R. Comes and S. Chambers. Interface structure, band alignment, and built-in potentials at $LaFeO_3$/n-$SrTiO_3$ heterojunctions. *Phys. Rev. Lett.*, 117:226802, 2016.

[39] R. E. Brandt, M. Young, H. H. Park, A. Dameron, D. Chua, Y. S. Lee, G. Teeter, R. G. Gordon, and T. Buonassisi. Band offsets of n-type electron-selective contacts on cuprous oxide (Cu_2O) for photovoltaics. *Appl. Phys. Lett.*, 105:263901, 2014.

[40] S. S. Wilson, J. P. Bosco, Y. Tolstova, D. O. Scanlon, G. W. Watson, and H. A. Atwater. Interface stoichiometry control to improve device voltage and modify band alignment in ZnO/Cu_2O heterojunction solar cells. *Energy Environ. Sci.*, 7:3606, 2014.

[41] S. A. Chambers, Y. Liang, Z. Yu, R. Droopad, J. Ramdani, and K. Eisenbeiser. Band discontinuities at epitaxial $SrTiO_3$/Si (001) heterojunctions. *Appl. Phys. Lett.*, 77:1662, 2000.

[42] S. Stemmer and S. J. Allen. Two-dimensional electron gases at complex oxide interfaces. *Annu. Rev. Mater. Res.*, 44:151–71, 2014.

[43] G. Drera, G. Salvinelli, F. Bondino, E. Magnano, M. Huijben, A. Brinkman, and L. Sangaletti. Intrinsic origin of interface states and band-offset profiling of nanostructured $LaAlO_3/SrTiO_3$ heterojunctions probed by element-specific resonant spectroscopies. *Phys. Rev. B*, 90:035124, 2014.

[44] Y. Li, S. N. Phattalung, S. Limpijumnong, J. Kim, and J. Yu. Formation of oxygen vacancies and charge carriers induced in the n-type interface of a $LaAlO_3$ overlayer on $SrTiO_3$(001). *Phys. Rev. B*, 84:245307, 2011.

[45] K. Yoshimatsu, R. Yasuhara, H. Kumigashira, and M. Oshima. Origin of metallic states at the heterointerface between the band insulators $LaAlO_3$ and $SrTiO_3$. *Phys. Rev. Lett.*, 101:026802, 2008.

[46] R. Schafranek, J. D. Baniecki, M. Ishii, Y. Kotaka, K. Yamanka, and K. Kurihara. Band offsets at the epitaxial $SrTiO_3/SrZrO_3$ (0 0 1) heterojunction. *J. Phys. D: Appl. Phys.*, 45:055303, 2012.

[47] S. A. Chambers, T. Droubay, T. C. Kaspar, and M. Gutowski. Experimental determination of valence band maxima for $SrTiO_3$, TiO_2, and SrO and the associated valence band offsets with Si(001). *J. Vac. Sci. Technol. B*, 22:2205–2215, 2004.

[48] S. A. Chambers, Y. Liang, Z. Yu, R. Droopad, and J. Ramdani. Band offset and structure of $SrTiO_3$ / Si (001) heterojunctions. *J. Vac. Sci. Technol. A*, 19:934, 2001.

[49] E. A. Kraut, R. W. Grant, J. R. Waldrop, and S. P. Kowalczyk. Precise determination of the valence-band edge in x-ray photoemission spectra: Application to measurement of semiconductor interface potentials. *Phys. Rev. Lett.*, 44:1620–1623, 1980.

[50] S. Siol, J. C. Hellmann, S. D. Tilley, M. Graetzel, J. Morasch, J. Deuermeier, W. Jaegermann, and A. Klein. Band alignment engineering at Cu_2O/ZnO heterointerfaces. *ACS Appl. Mater. Interfaces*, 8:21824–21831, 2016.

[51] G. Salvinelli, G. Drera, C. Baratto, A. Braga, and L. Sangaletti. Stoichiometry gradient, cation interdiffusion, and band alignment between a nanosized TiO_2 blocking layer and a transparent conductive oxide in dye-sensitized solar cell front contacts. *ACS Appl. Mater. Interfaces*, 7:765–773, 2015.

[52] S. A. Chambers, M. H. Engelhard, V. Shutthanandan, Z. Zhu, T. C. Droubay, L. Qiao, P. V. Sushko, T. Feng, H. D. Lee, T. Gustafsson, E. Garfunkel, A. B. Shah, J. M. Zuo, and Q. M. Ramasse. Instability, intermixing and electronic structure at the epitaxial $LaAlO_3/SrTiO_3$(001) heterojunction. *Surface Science Reports*, 65:317–352, 2010.

[53] Y. Segal, J. H. Ngai, J. W. Reiner, F. J. Walker, and C. H. Ahn. X-ray photoemission studies of the metal-insulator transition in $LaAlO_3/SrTiO_3$ structures grown by molecular beam epitaxy. *Phys. Rev. B*, 80:241107(R), 2009.

[54] G. Drera, G. Salvinelli, A. Brinkman, M. Huijben, G. Koster, H. Hilgenkamp, G. Rijnders, D. Visentin, and L. Sangaletti. Band offsets and density of Ti^{3+} states probed by x-ray photoemission on $LaAlO_3/SrTiO_3$ heterointerfaces and their $LaAlO_3$ and $SrTiO_3$ bulk precursors. *Phys. Rev. B*, 87:075435, 2013.

[55] A. I. Lebedev. Band offsets in heterojunctions formed by oxides with cubic perovskite structure. *Physics of the Solid State*, 56:1039–1047, 2014.

[56] R. Pentcheva and W. E. Pickett. Ionic relaxation contribution to the electronic reconstruction at the n-type $LaAlO_3/SrTiO_3$ interface. *Phys. Rev. B*, 78:205106, 2008.

[57] H. Banerjee, S. Banerjee, M. Randeria, and T. Saha-Dasgupta. Electronic structure of oxide interfaces: A comparative analysis of $GdTiO_3/SrTiO_3$ and $LaAlO_3/SrTiO_3$ interfaces. *Sci. Rep.*, 5:18647, 2015.

[58] Z. S. Popović, S. Satpathy, and R. M. Martin. Origin of the two-dimensional electron gas carrier density at the $LaAlO_3$ on $SrTiO_3$ interface. *Phys. Rev. Lett.*, 101:256801, 2008.

[59] C. G. Van de Walle and R. M. Martin. Theoretical calculations of semiconductor heterojunction discontinuities. *J. Vac. Sci. Technol. B*, 4:1055, 1986.

[60] A. D. Katnani and G. Margaritondo. Microscopic study of semiconductor heterojunctions: Photoemission measurement of the valance-band discontinuity and of

the potential barriers. *Phys. Rev. B*, 28:1944–1956, 1983.

[61] C. Feng, W. Wen-Bin, L. Shun-Yi, and A. Kleinb. Energy band alignment at ferroelectric/electrode interface determined by photoelectron spectroscopy. *Chin. Phys. B*, 23:017702, 2014.

[62] R. Schafranek, S. Li, F. Chen, W. Wu, and A. Klein. $PbTiO_3/SrTiO_3$ interface: Energy band alignment and its relation to the limits of Fermi level variation. *Phys. Rev. B*, 84:045317, 2011.

[63] J. Tersof. Theory of semiconductor heterojunctions: The role of quantum dipoles. *Phys. Rev. B*, 30:4874–4877, 1984.

[64] M. Huijben, G. Rijnders, D. H. A. Blank, S. Bals, S. Van Aert, J. Verbeeck, G. Van Tendeloo, A. Brinkman, and H. Hilgenkamp. Electronically coupled complementary interfaces between perovskite band insulators. *Nature Materials*, 5:556–560, 2006.

[65] N. Nakagawa, H. Y. Hwang, and D. A. Muller. Why some interfaces cannot be sharp. *Nature Materials*, 5:204–209, 2006.

[66] A. Kalabukhov, R. Gunnarsson, J. Börjesson, E. Olsson, T. Claeson, and D. Winkler. Effect of oxygen vacancies in the $SrTiO_3$ substrate on the electrical properties of the $LaAlO_3/SrTiO_3$ interface. *Phys. Rev. B*, 75:121404(R), 2007.

[67] G. Drera, F. Banfi, F. Federici Canova, P. Borghetti, L. Sangaletti, F. Bondino, E. Magnano, J. Huijben, M. Huijben, G. Rijnders, D. H. A. Blank, H. Hilgenkamp, and A. Brinkman. Spectroscopic evidence of in-gap states at the $SrTiO_3$ /$LaAlO_3$ ultrathin interfaces. *App. Phys. Lett.*, 98:052907, 2011.

[68] G. Berner, M. Sing, H. Fujiwara, A. Yasui, Y. Saitoh, A. Yamasaki, Y. Nishitani, A. Sekiyama, N. Pavlenko, T. Kopp, C. Richter, J. Mannhart, S. Suga, and R. Claessen. Direct k-space mapping of the electronic structure in an oxide-oxide interface. *Phys. Rev. Lett.*, 110:247601, 2013.

[69] C. Cancellieri, M. L. Reinle-Schmitt, M. Kobayashi, V. N. Strocov, T. Schmitt, P. R. Willmott, S. Gariglio, and J. M. Triscone. Interface fermi states of $LaAlO_3/SrTiO_3$ and related heterostructures. *Phys. Rev. Lett.*, 110:137601, 2013.

[70] C. Cancellieri, M. L. Reinle-Schmitt, M. Kobayashi, V. N. Strocov, P. R. Willmott, D. Fontaine, Ph. Ghosez, A. Filippetti, P. Delugas, and V. Fiorentini. Doping-dependent band structure of $LaAlO_3/SrTiO_3$ interfaces by soft x-ray polarization-controlled resonant angle-resolved photoemission. *Phys. Rev. B*, 89:121412(R), 2014.

[71] K. Janicka, J. P. Velev, and E. Y. Tsymbal1. Quantum nature of two-dimensional electron gas confinement at $LaAlO_3/SrTiO_3$ interfaces. *Phys. Rev. Lett.*, 102:106803, 2009.

[72] G. J. De Raad, D. M. Bruls, P. M. Koenraad, and J. H. Wolter. Interplay between tip-induced band bending and voltage-dependent surface corrugation on GaAs (110) surfaces. *Phys. Rev. B*, 66:195306, 2002.

[73] Y. P. Chiu, B. C. Huang, M. C. Shih, J. Y. Shen, P. Chang, C. S. Chang, M. L. Huang, M. H. Tsai, M. Hong, and J. Kwo. Atomic-scale determination of band offsets at the Gd_2O_3/GaAs (100) hetero-interface using scanning tunneling spectroscopy. *Appl. Phys. Lett.*, 99:212101, 2011.

[74] B. C. Huang, Y. P. Chiu, P. C. Huang, W. C. Wang, V. T. Tra, J. C. Yang, Q. He, J. Y. Lin, C. S. Chang, and Y. H. Chu. Mapping band alignment across complex oxide heterointerfaces. *Phys. Rev. Lett.*, 109:246807, 2012.

[75] M. Sing, G. Berner, K. Goß, A. Müller, A. Ruff, A. Wetscherek, S. Thiel, J. Mannhart,

S. A. Pauli, C. W. Schneider, P. R. Willmott, M. Gorgoi, F. Schäfers, and R. Claessen. Profiling the interface electron gas of $LaAlO_3/SrTiO_3$ heterostructures with hard X-ray photoelectron spectroscopy. *Phys. Rev. Lett.*, 102:176805, 2009.

[76] L. Qiao, T. C. Droubay, T. C. Kaspar, P. V. Sushko, and S. A. Chambers. Cation mixing, band offsets and electric fields at $LaAlO_3/SrTiO_3$(001) heterojunctions with variable La:Al atom ratio. *Surface Science*, 605:1381–1387, 2011.

[77] A. Janotti, L. Bjaalie, L. Gordon, and C. G. Van de Walle. Controlling the density of the two-dimensional electron gas at the $SrTiO_3/LaAlO_3$ interface. *Phys. Rev. B*, 86:241108(R), 2012.

[78] G. Singh-Bhalla, C. Bell, J. Ravichandran, W. Siemons, Y. Hikita, S. Salahuddin, A. F. Hebard, H. Y. Hwang, and R. Ramesh. Built-in and induced polarization across $LaAlO_3/SrTiO_3$ heterojunctions. *Nature Physics*, 7:80–86, 2011.

[79] E. Slooten, Z. Zhong, H. J. A. Molegraaf, P. D. Eerkes, S. De Jong, F. Massee, E. Van Heumen, M. K. Kruize, S. Wenderich, J. E. Kleibeuker, M. Gorgoi, H. Hilgenkamp, A. Brinkman, M. Huijben, G. Rijnders, D. H. A. Blank, G. Koster, P. J. Kelly, and M. S. Golden. Hard x-ray photoemission and density functional theory study of the internal electric field in $SrTiO_3/LaAlO_3$ oxide heterostructures. *Phys. Rev. B*, 87:085128, 2013.

[80] L. Qiao, T. C. Droubay, V. Shutthanandan, Z. Zhu, P. V. Sushko, and S. A. Chambers. Thermodynamic instability at the stoichiometric $LaAlO_3/SrTiO_3$(001) interface. *J. Phys.: Condens. Matter*, 22:312201, 2010.

[81] C. Li, Z. Liu, Z. Lu, X. R. Wang, A. Annadi, Z. Huang, S. Zeng, and T. Venkatesan. Tailoring the two dimensional electron gas at polar $ABO_3/SrTiO_3$ interfaces for oxide electronics. *Scientific Reports*, 5:13314, 2015.

[82] S. A. Chambers, L. Qiao, T. C. Droubay, T. C. Kaspar, B.W. Arey, and P.V. Sushko. Band alignment, built-in potential, and the absence of conductivity at the $LaCrO_3/SrTiO_3$ (001) heterojunction. *Phys. Rev. Lett.*, 107:206802, 2011.

[83] P. Moetakef, T. A. Cain, D. G. Ouellette, J. Y. Zhang, D. O. Klenov, A Janotti, C. G. Van de Walle, S. Rajan, S: J. Allen, and S. Stemmer. Electrostatic carrier doping of $GdTiO_3/SrTiO_3$ interfaces. *Appl. Phys. Lett.*, 99:232116, 2011.

[84] B. Yin, P. Aguado-Puente, S. Qu, and E. Artacho. Two-dimensional electron gas at the $PbTiO_3/SrTiO_3$ interface: An ab initio study. *Phys. Rev. B*, 92:115406, 2015.

[85] P. Delugas, A. Filippetti, A. Gadaleta, I. Pallecchi, D. Marré, and V. Fiorentini. Large band offset as driving force of two-dimensional electron confinement: The case of $SrTiO_3/SrZrO_3$ interface. *Phys. Rev. B*, 88:115304, 2013.

[86] R. Schafranek, J. D. Baniecki, M. Ishii, Y. Kotaka, and K. Kurihara. The $SrTiO_3/BiFeO_3$ (001) interface: commutativity of energy band discontinuities. *New Journal of Physics*, 15:053014, 2013.

[87] C. Chen, S. Lv, J. Li, Z. Wang, X. Liang, Y. Li, D. Viehland, K. Nakajima, and Y. Ikuhara. Two-dimensional electron gas at the Ti-diffused $BiFeO_3/SrTiO_3$ interface. *Appl. Phys. Lett.*, 107:031601, 2015.

[88] C. He, T. D. Sanders, M. T. Gray, F. J. Wong, V. V. Mehta, and Y. Suzuki. Metal-insulator transitions in epitaxial $LaVO_3$ and $LaTiO_3$ films. *Phys. Rev. B*, 86:081401(R), 2012.

[89] A. Annadi, A. Putra, Z. Q. Liu, K. Wang, X.and Gopinadhan, Z. Huang, S. Dhar, T. Venkatesan, and Ariando. Electronic correlation and strain effects at the interfaces between polar and nonpolar complex oxides. *Phys. Rev. B*, 86:085450, 2012.

[90] S. W. Lee, Y. Liu, J. Heo, and R. G. Gordon. Creation and control of two-

dimensional electron gas using al-based amorphous oxides/$SrTiO_3$ heterostructures grown by atomic layer deposition. *Nano Lett.*, 12:4775–4783, 2012.

[91] D. F. Li, Y. Wang, and J. Y. Dai. Tunable electronic transport properties of $DyScO_3$/$SrTiO_3$ polar heterointerface. *Appl. Phys. Lett.*, 98:122108, 2011.

[92] A. Kalabukhov, T. Claeson, P. P. Aurino, R. Gunnarsson, D. Winkler, E. Olsson, N. Tuzla, J. Börjesson, Y. A. Boikov, I. T. Serenkov, V. I. Sakharov, and M. P. Volkov. Electrical and structural properties of ABO_3/$SrTiO_3$ interfaces. *Mater. Res. Soc. Symp. Proc.*, 1454:167–172, 2012.

[93] Y. Chen, F. Trier, T. Kasama, D. V. Christensen, N. Bovet, Z. I. Balogh, H. Li, K. T. S. Thydén, W. Zhang, S. Yazdi, P. Norby, N. Pryds, and S. Linderoth. Creation of high mobility two-dimensional electron gases via strain induced polarization at an otherwise nonpolar complex oxide interface. *Nano Lett.*, 15:1849–1854, 2015.

[94] M. Salluzzo, S. Gariglio, D. Stornaiuolo, V. Sessi, S. Rusponi, C. Piamonteze, G. M. De Luca, M. Minola, D. Marré, A. Gadaleta, H. Brune, F. Nolting, N. B. Brookes, and G. Ghiringhelli. Origin of interface magnetism in $BiMnO_3$/$SrTiO_3$ and $LaAlO_3$/$SrTiO_3$ heterostructures. *Phys. Rev. Lett.*, 111:087204, 2013.

[95] Y. Du, H. Y. Peng, H. Mao, K. X. Jin, H. Wang, F. Li, X. Y. Gao, W. Chen, and T. Wu. Evolution of the $SrTiO_3$-MoO_3 interface electronic structure: An in situ photoelectron spectroscopy study. *ACS Appl. Mater. Interfaces*, 7:11309–11314, 2015.

[96] C. Ke, W. Zhu, Z. Zhang, E. S. Tokb, and J. Panb. Energy band alignment of SnO_2/$SrTiO_3$ epitaxial heterojunction studied by X-ray photoelectron spectroscopy. *Surf. Interface Anal.*, 47:824–827, 2015.

[97] S. A. Chambers, T. Ohsawa, C. M. Wang, I. Lyubinetsky, and J. E. Jaffe. Band offsets at the epitaxial anatase TiO_2/n-$SrTiO_3$(001) interface. *Surface Science*, 603:771–780, 2009.

[98] W. Siemons, G. Koster, H. Yamamoto, T. H. Geballe, D. H. A. Blank, and M. R. Beasley. Experimental investigation of electronic properties of buried heterointerfaces of $LaAlO_3$ on $SrTiO_3$. *Phys. Rev. B*, 76:155111, 2007.

[99] M. Pavan, S. Rühle, A. Ginsburg, D. A. Keller, H. Barad, P. M. Sberna, D. Nunes, R. Martins, A. Y. Anderson, A. Zaban, and E. Fortunato. TiO_2/Cu_2O all-oxide heterojunction solar cells produced by spray pyrolysis. *Solar Energy Materials and Solar Cells*, 132:549–556, 2015.

[100] D. Sharma, S. Upadhyay, V. R. Satsangi, R. Shrivastav, U. V. Waghmare, and S. Dass. Improved photoelectrochemical water splitting performance of Cu_2O/$SrTiO_3$ heterojunction photoelectrode. *J. Phys. Chem. C*, 118:25320–25329, 2014.

[101] C. Liu, P. Li, G. Wu, B. Luo, S. Lin, Ren A., and W. Shi. Enhanced photoelectrochemical and photocatalytic activity by Cu_2O/$SrTiO_3$ p-n heterojunction via a facile deposition-precipitation technique. *RSC Adv.*, 5:33938, 2015.

[102] C. Wang, X. Zhang, Y. Wei, L. Kong, F. Chang, H. Zheng, L. Wu, J. Zhi, and Y. Liu. Correlation between band alignment and enhanced photocatalysis: a case study with anatase/TiO_2(B) nanotube heterojunction. *Dalton Trans.*, 44:13331, 2015.

[103] T. Ohno, K. Tokieda, S. Higashida, and M. Matsumura. Synergism between rutile and anatase TiO_2 particles in photocatalytic oxidation of naphthalene. *Appl. Catal. A: Gen.*, 244:383–391, 2003.

[104] S. Shen, X. Wang, T. Chen, Z. Feng, and C. Li. Transfer of photoinduced electrons in anatase-rutile TiO_2 determined by time-resolved mid-infrared spectroscopy. *J. Phys. Chem. C*, 118:12661–12668, 2014.

[105] D. O. Scanlon, C. W. Dunnill, J. Buckeridge, S. A. Shevlin, A. J. Logsdail, S. M. Woodley, C. R. A. Catlow, M. J. Powell, R. G. Palgrave, I. P. Parkin, G. W. Watson, T. W. Kea, P. Sherwood, A. Walsh, and A. A. Sokol. Band alignment of rutile and anatase TiO_2. *Nature Materials*, 12:798–801, 2013.

[106] X. Zhang, Y. Lin, D. He, J. Zhang, Z. Fan, and T. Xie. Interface junction at anatase/rutile in mixed phase TiO_2: Formation and photo-generated charge carriers properties. *Chem. Phys. Lett.*, 504:71–75, 2011.

[107] D. C. Hurum, A. G. Agrios, K. A: Gray, T. Rajh, and M. C. Thurnauer. Explaining the enhanced photocatalytic activity of degussa P25 mixed-phase TiO_2 using epr. *Phys. Chem. B*, 107:4545–4549, 2003.

[108] J. Kullgren, B. Aradi, T. Frauenheim, L. Kavan, and P. Deák. Resolving the controversy about the band alignment between rutile and anatase: The role of OH^-/H^+ adsorption. *J. Phys. Chem. C*, 119:21952–21958, 2015.

[109] V. Assunção, E. Fortunato, A. Marques, H. Àguas, I. Ferreira, M. E. V. Costa, and R. Martins. Influence of the deposition pressure on the properties of transparent and conductive ZnO:Ga thin-film produced by RF sputtering at room temperature. *Thin Solid Films*, 427:401–405, 2003.

[110] A. A. Tracton. *Coatings Technology - Fundamentals, Testing and Processing Techniques*. CRC Press, 2007.

[111] K. Seshan. *Handbook of Thin-Film Deposition Processes and Techniques - Principles, Methods, Equipment and Applications*. Noyes Publications, 2002.

[112] P. J. Goodhew, J. Humphreys, and R. Beanland. *Electron Microscopy and Analysis*. Taylor and Francis, 2001.

[113] G. Kaupp. *Atomic Force Microscopy, Scanning Nearfield Optical Microscopy And Nanoscratching - Application to Rough and Natural Surfaces*. Springer, 2006.

[114] V. L. Mironov. *Fundamentals of scanning probe microscopy*. The Russian academy of sciences institute of physics of microstructures, 2004.

[115] J. A. Christman, R. R. Woolcott Jr., A. I. Kingon, and R. J. Nemanich. Piezoelectric measurements with atomic force microscopy. *Appl. Phys. Lett.*, 73:3851–3853, 1998.

[116] E. Soergel. Piezoresponse force microscopy (PFM). *J. Phys. D: Appl. Phys.*, 44:464003, 2011.

[117] W. Kim, J. Y. Son, and H. M. Jang. Confinement of ferroelectric domain-wall motion at artificially formed conducting-nanofilaments in epitaxial $BiFeO_3$ thin films. *ACS Appl. Mater. Interfaces*, 6:6346–6350, 2014.

[118] A. Baji, Y. Mai, Q. Li, S. Wong, Y. Liu, and Q. W. Yao. One-dimensional multiferroic bismuth ferrite fibers obtained by electrospinning techniques. *Nanotechnology*, 22:235702, 2011.

[119] N. Balke, S. Jesse, Q. Li, P. Maksymovych, M. B. Okatan, E. Strelcov, A. Tselev, and S. V. Kalinin. Current and surface charge modified hysteresis loops in ferroelectric thin films. *J. Appl. Phys.*, 118:072013, 2015.

[120] F. Fan, B. Luo, M. Duan, and C. Chen. Domain switching and effects in $BiFeO_3$ thin film on a $Pt/Ti/SiO_2/Si$ (111) substrate. *Chinese Journal of Physics*, 51:834–843, 2013.

[121] S. Kalinin and A. Gruverman. *Scanning Probe Microscopy: Electrical and Electromechanical Phenomena at the Nanoscale*. Springer, 2007.

[122] A. Gruverman and S. V. Kalinin. Piezoresponse force microscopy and recent advances in nanoscale studies of ferroelectrics. *Journal of materials science*, 41:107–116, 2006.

[123] S. Hüfner. *Photoelectron Spectroscopy - Principles and Applications*. Springer, 2003.

[124] C. R. Brundle and A. D. Baker. *Electron Spectroscopy: Theory, Techniques and Applications - Volume 2*. Academic Press, 1978.

[125] C. S. Fadley. X-ray photoelectron spectroscopy: Progress and perspectives. *Journal of Electron Spectroscopy and Related Phenomena*, 178-179:2–32, 2010.

[126] P. Y. Yu and M. Cardona. *Fundamentals of Semiconductors - Physics and Materials Properties, 3rd Ed*. Springer, 2005.

[127] N. Mårtensson, M. Weinelt, O. Karis, M. Magnuson, N. Wassdahl, A. Nilsson, J. Stöhr, and M. Samant. Coherent and incoherent processes in resonant photoemission. *Appl. Phys. A*, 65:159–167, 1997.

[128] A. Pancotti, N. Barrett, L. F. Zagonel, and G. M. Vanacore. Multiple scattering x-ray photoelectron diffraction study of the $SrTiO_3$(100) surface. *J. Appl. Phys.*, 106:034104, 2009.

[129] D. P. Woodruff. Adsorbate structure determination using photoelectron diffraction: Methods and applications. *Surface Science Reports*, 62:1–38, 2007.

[130] L. Despont, C. Lichtensteiger, F. Clerc, M. G. Garnier, F. J. Garcia de Abajo, M. A. Van Hove, and P. Triscone, J. M.and Aebi. X-ray photoelectron diffraction study of ultrathin $PbTiO_3$ films. *Eur. Phys. J. B*, 49:141–146, 2006.

[131] A. Winkelmann, C. S. Fadley, and F. J. Garcia de Abajo. High-energy photoelectron diffraction: model calculations and future possibilities. *New Journal of Physics*, 10:113002, 2008.

[132] S. Mobilio, F. Boscherini, and C. Meneghini. *Synchrotron Radiation - Basics, Methods and Applications*. Springer, 2015.

[133] P. A. Brühwiler, O. Karis, and N. Mårtensson. Charge-transfer dynamics studied using resonant core spectroscopies. *Rev. Mod. Phys.*, 74:703–740, 2002.

[134] U. Fano. Effects of configuration interaction on intensities and phase shifts. *Physical Review*, 124:1866–1878, 1961.

[135] C. S. Schnohr and M. C. Ridgway. *X-Ray Absorption Spectroscopy of Semiconductors*. Springer, 2015.

[136] J. A. McCleverty and T. J. Meyer. *Comprehensive Coordination Chemistry II*. Elsevier Science, 2003.

[137] J. J. Rehr and R. C. Albers. Theoretical approaches to x-ray absorption fine structure. *Rev. Mod. Phys.*, 72:621–654, 2000.

[138] G. A. Waychunas. Synchrotron radiation XANES pectroscopy of Ti in minerals: Effects of Ti bonding distances, Ti valence, and site geometry on absorption edge structure. *American Mineralogist*, 72:89–101, 1987.

[139] G. Bunker. *Introduction to XAFS*. Cambridge University Press, 2010.

[140] J. Stöhr and S. Anders. X-ray spectro-microscopy of complex materials and surfaces. *IBM J. Res. Develop.*, 44:535–551, 2000.

[141] P. Söderlind, O. Eriksson, B. Johansson, R. C. Albers, and A. M. Boring. Spin and orbital magnetism in Fe-Co and Co-Ni alloys. *Phys. Rev. B*, 45:12911, 1992.

[142] J. S. Lee, Y. W. Xie, H. K. Sato, C. Bell, Y. Hikita, H. Y. Hwang, and C. C. Kao. Titanium d_{xy} ferromagnetism at the $LaAlO_3/SrTiO_3$ interface. *Nature Materials*, 12:703–706, 2013.

[143] J. Stöhr. Exploring the microscopic origin of magnetic anisotropies with X-ray magnetic circular dichroism (XMCD) spectroscopy. *Journal of Magnetism and Magnetic Materials*, 200:470–497, 1999.

[144] D. Pesquera, G. Herranz, A. Barla, E. Pellegrin, F. Bondino, E. Magnano, Sánchez

F., and J. Fontcuberta. Surface symmetry-breaking and strain effects on orbital occupancy in transition metal perovskite epitaxial films. *Nature Communication*, 3:1189, 2012.

[145] J. Stöhr, H. A. Padmore, S. Anders, T. Stammler, and M. R. Scheinfein. Principles of X-ray magnetic dichroism spectromicroscopy. *Surface Review and Letters*, 5:1297–1308, 1998.

[146] M. Salluzzo, J. C. Cezar, N. B. Brookes, V. Bisogni, G. M. De Luca, C. Richter, S. Thiel, J. Mannhart, M. Huijben, A. Brinkman, G. Rijnders, and G. Ghiringhelli. Orbital reconstruction and the two-dimensional electron gas at the $LaAlO_3/SrTiO_3$ interface. *Phys. Rev. Lett.*, 102:166804, 2009.

[147] K. A. Müller and H. Burkard. $SrTiO_3$: An intrinsic quantum paraelectric below 4 K. *Phys. Rev. B*, 19:3593, 1979.

[148] J. H. Haeni, P. Irvin, W. Chang, R. Uecker, P. Reiche, Y. L. Li, S. Choudhury, W. Tian, M. E. Hawley, B. Craigo, A. K. Tagantsev, X. Q. Pan, S. K. Streiffer, L. Q. Chen, S. W. Kirchoefer, J. Levy, and D. G. Schlom. Room-temperature ferroelectricity in strained $SrTiO_3$. *Nature*, 430:758, 2004.

[149] H. P. R. Frederikse and W. R. Hosler. Hall mobility in $SrTiO_3$. *Phys. Rev.*, 161:822, 1967.

[150] G. Binnig, A. Baratoff, H. E. Hoenig, and J. G. Bednorz. Two-Band Superconductivity in Nb-Doped $SrTiO_3$. *Phys. Rev. Lett.*, 45:1352, 1980.

[151] H. Bea, M. Bibes, A. Barthelemy, K. Bouzehouane, E. Jacquet, A. Khodan, J. P. Contour, S. Fusil, F. Wyczisk, A. Forget, D. Lebeugle, D. Colson, and M. Viret. Influence of parasitic phases on the properties of $BiFeO_3$ epitaxial thin films. *Appl. Phys. Lett.*, 87:072508, 2005.

[152] G. D. Wilk, R. M. Wallace, and J. M. Anthony. High-k gate dielectrics: Current status and materials properties considerations. *J. Appl. Phys.*, 89:5243, 2001.

[153] A. Kosola, M. Putkonen, L. S. Johansson, and L. Niinistö. Effect of annealing in processing of strontium titanate thin films by ALD. *Appl. Surf. Sci.*, 211:102, 2003.

[154] W. J. Weber, R. C. Ewing, C. R. A. Catlow, T. Diaz de la Rubia, L. W. Hobbs, C. Kinoshita, Hj. Matzke, A. T. Motta, M. Nastasi, E. K. H. Salje, E. R. Vance, and S. J. Zinkle. Radiation effects in crystalline ceramics for the immobilization of high-level nuclear waste and plutonium. *J. Mater. Res.*, 13:1434, 1998.

[155] F. T. Wagner and G. A. Somorjai. Photocatalytic hydrogen production from water on Pt-free $SrTiO_3$ in alkali hydroxide solutions. *Nature*, 285:559, 1980.

[156] J. C. Ruiz-Morales, J. Canales-Vázquez, C. Savaniu, D. Marrero-López, W. Zhou, and J. T. S. Irvine. Disruption of extended defects in solid oxide fuel cell anodes for methane oxidation. *Nature*, 439:568, 2006.

[157] R. A. McKee, F. J. Walker, and M. F. Chisholm. Physical Structure and Inversion Charge at a Semiconductor Interface with a Crystalline Oxide. *Science*, 293:468, 2001.

[158] J. Zhang, S. Walsh, C. Brooks, D. G. Schlom, and L. J. Brillson. Depth-resolved cathodoluminescence spectroscopy study of defects in $SrTiO_3$. *Journal of Vacuum Science and Technology B*, 26:1466, 2008.

[159] H. Yamada and G. R. Miller. Point defects in reduced strontium titanate. *J. Solid State Chem.*, 6:169, 1973.

[160] D. A. Muller, N. Nakagawa, A. Ohtomo, J. L. Grazul, and H. Y. Hwang. Atomic-scale imaging of nanoengineered oxygen vacancy profiles in $SrTiO_3$. *Nature*, 430:657, 2004.

[161] V. E. Henrich, G. Dresselhaus, and H. J. Zeiger. Surface defects and the electronic structure of $SrTiO_3$ surfaces. *1978*, 17:4908, Phys. Rev. B.

[162] A. Gentils, O. Copie, G. Herranz, F. Fortuna, M. Bibes, K. Bouzehouane, É. Jacquet, C. Carrétéro, M. Basletić, E. Tafra, A. Hamzić, and A. Barthélémy. Point defect distribution in high-mobility conductive $SrTiO_3$ crystals. *Phys. Rev. B*, 81:144109, 2010.

[163] O. N. Tufte and P. W. Chapman. Electron Mobility in Semiconducting Strontium Titanate. *Phys. Rev.*, 155:796, 1967.

[164] J. Son, P. Moetakef, B. Jalan, O. Bierwagen, N. J. Wright, R. Engel-Herbert, and S. Stemmer. Epitaxial $SrTiO_3$ films with electron mobilities exceeding 30,000 cm^2 v^{-1} s^{-1}. *Nat. Mater.*, 9:482, 2010.

[165] Y. S. Kim, J. Kim, S. J. Moon, W. S. Choi, Y. J. Chang, J. G. Yoon, J. Yu, J. S. Chung, and T. W. Noh. Localized electronic states induced by defects and possible origin of ferroelectricity in strontium titanate thin films. *Appl. Phys. Lett.*, 94:202906, 2009.

[166] D. W. Oh, J. Ravichandran, C. W. Liang, W. Siemons, B. Jalan, C. M. Brooks, M. Huijben, D. G. Schlom, S. Stemmer, L. W. Martin, A. Majumdar, R. Ramesh, and D. G. Cahill. Thermal conductivity as a metric for the crystalline quality of $SrTiO_3$ epitaxial layers. *Appl. Phys. Lett.*, 98:221904, 2011.

[167] D. Kan, T. Terashima, R. Kanda, A. Masuno, K. Tanaka, S. Chu, H. Kan, A. Ishizumi, Y. Kanemitsu, Y. Shimakawa, and M. Takano. Blue-light emission at room temperature from ar^+-irradiated $SrTiO_3$. *Nat. Mater.*, 4:816, 2005.

[168] C. M. Brooks, R. B. Wilson, A. Schäfer, J. A. Mundy, M. E. Holtz, D. A. Muller, J. Schubert, D. G. Cahill, and D. G. Schlom. Tuning thermal conductivity in homoepitaxial $SrTiO_3$ films via defects. *Appl. Phys. Lett.*, 107:051902, 2015.

[169] A. Leitner, C. T. Rougers, J. C. Price, D. A. Herman, and D. R. Herman. Pulsed laser deposition of superconducting Nb-doped strontium titanate thin films. *Appl. Phys. Lett.*, 72:3065, 1998.

[170] N. Shanthi and D. D. Sarma. Electronic structure of electron doped $SrTiO_3$: $SrTiO_{3-\delta}$ and $Sr_{1-x}La_xTiO_3$. *Phys. Rev. B*, 57:2153, 1998.

[171] H. Wang, D. Cui, S. Dai, H. Lu, Y. Zhou, Z. Chen, and G. Yang. Optical and transport properties of Sb-doped $SrTiO_3$ thin films. *J. Appl. Phys.*, 90:4664, 2009.

[172] T. Higuchi, T. Tsukamoto, N. Sata, M. Ishigame, Y. Tezuka, and S. Shin. Electronic structure of p-type $SrTiO_3$ by photoemission spectroscopy. *Phys. Rev. B*, 57:6978, 1998.

[173] T. Fix, R. Bali, N. Stelmashenko, and M. G. Blamire. Influence of the dopant concentration in In-doped $SrTiO_3$ on the structural and transport properties. *Solid State Communications*, 146:428–430, 2008.

[174] L. Qiao, T. C. Droubay, T. Varga, M. E. Bowden, V. Shutthanandan, Z. Zhu, T. C. Kaspar, and S. A. Chambers. Epitaxial growth, structure, and intermixing at the $LaAlO_3/SrTiO_3$ interface as the film stoichiometry is varied. *Phys. Rev. B*, 83:085408, 2011.

[175] G. Drera, L. Sangaletti, F. Bondino, M. Malvestuto, L. Malavasi, Y. Diaz-Fernandez, S. Dash, M. C. Mozzati, and P. Galinetto. Labeling interacting configurations through an analysis of excitation dynamics in a resonant photoemission experiment: the case of rutile TiO_2. *J. of Phys. Cond. Mat.*, 25:075502, 2013.

[176] G. Drera, M. C. Mozzati, P. Galinetto, Y. Diaz-Fernandez, L. Malavasi, F. Bondino, M. Malvestuto, and L. Sangaletti. Enhancement of room temperature ferromagnetism in N-doped TiO_{2-x} rutile: Correlation with the local electronic properties.

Appl. Phys. Lett., 97:012506, 2010.

[177] G. Koster, B. L. Kropman, G. J. H. M. Rijnders, D. H. A. Blank, and H. Rogalla. Quasi-ideal strontium titanate crystal surfaces through formation of strontium hydroxide. *Appl. Phys. Lett.*, 73:2920, 1998.

[178] F. M. F. De Groot, J. C. Fuggle, B. T. Thole, and G. A. Sawatzky. $L_{2,3}$ x-ray-absorption edges of d^0 compounds: K^+, ca^{2+}, sc^{3+}, and ti^{4+} in o_h (octahedral) symmetry. *Phys. Rev. B*, 41:928–937, 1990.

[179] W. Eerenstein, N. D. Mathur, and J. F. Scott. Multiferroic and magnetoelectric materials. *Nature*, 442:759–765, 2006.

[180] L. Yan, M. Zhuo, Z. Wang, J. Yao, N. Haberkorn, S. Zhang, L. Civale, J. Li, D. Viehland, and Q. X. Jia. Magnetoelectric properties of flexible $BiFeO_3$/Ni tapes. *Appl. Phys. Lett.*, 101:012908, 2012.

[181] R. Guo, L. You, Y. Zhou, Z. S. Lim, X. Zou, L. Chen, R. Ramesh, and J. Wang. Non-volatile memory based on the ferroelectric photovoltaic effect. *Nat. Communications*, 4:1990, 2013.

[182] V. V. Abramova, A. Slesarev, and A. Sinitskii. Synthesis of high-quality inverse opals based on magnetic complex oxides: yttrium iron garnet ($Y_3Fe_5O_{12}$) and bismuth ferrite ($BiFeO_3$). *J. Mat. Chem. C*, 1:2975–2982, 2013.

[183] J. H. Lee, I. Fina, X. Marti, Y. H. Kim, D. Hesse, and M. Alexe. Spintronic functionality of $BiFeO_3$ domain walls. *Adv. Mater*, 26:7078–7082, 2014.

[184] W. Ji, K. Yao, and Y. C. Liang. Bulk photovoltaic effect at visible wavelength in epitaxial ferroelectric $BiFeO_3$ thin films. *Adv. Mater*, 22:1763–1766, 2010.

[185] R. Ramesh and N. A. Spaldin. Multiferroics: progress and prospects in thin films. *Nat. Mater.*, 6:21–29, 2007.

[186] J. Kabelac, S. Ghosh, P. Dobal, and R. Katiyar. RF oxygen plasma assisted molecular beam epitaxy growth of $BiFeO_3$ thin films on $SrTiO_3$ (001). *J. Vac. Sci. Technol. B*, 25:1049–1052, 2007.

[187] R. Y. Zheng, X. S. Gao, Z. H. Zhou, and J. Wang. Thin films deposited on $SrRuO_3$ buffer layer by rf sputtering. *J. Appl. Phys.*, 101:054104, 2007.

[188] Y. H. Lee, J. M. Wu, Y. L. Chueh, and L. J Chou. Low-temperature growth and interface characterization of $BiFeO_3$ thin films with reduced leakage current. *Appl. Phys. Lett.*, 87:172901, 2005.

[189] J. O. Cha, J. S. Ahn, and K. B. Lee. Multiferroic $BiFeO_3$ thin films prepared by using a conventional RF magnetron sputtering method. *J. Korean Phys. Soc.*, 54:844–848, 2009.

[190] H. A. Begum, H. Naganuma, M. Oogane, and Y. Ando. Fabrication of multiferroic Co-substituted $BiFeO_3$ epitaxial films on $SrTiO_3$ (100) substrates by radio frequency magnetron sputtering. *Materials*, 4:1087–1095, 2011.

[191] S. R. Jian, H. W. Chang, Y. C. Tseng, P. H. Chen, and J. Y. Juang. Structural and nanomechanical properties of $BiFeO_3$ thin films deposited by radio frequency magnetron sputtering. *Nano. Res. Lett.*, 8:297, 2013.

[192] C. Ternon, J. Thery, T. Baron, C. Ducros, F. Sanchette, and J. Kreisel. Structural properties of films grown by magnetron sputtering of a $BiFeO_3$ target. *Thin Solid Films*, 515:481–484, 2006.

[193] G. Drera, G. Salvinelli, J. Ahlundb, P. G. Karlsson, B. Wannbergb, E. Magnano, S. Nappini, and L. Sangaletti. Transmission function calibration of an angular resolved analyzer for x-ray photoemission spectroscopy: theory vs experiment. *J. of Elect. Spec. Relat. Phen*, 195:109–116, 2014.

[194] R. Yamamoto, C. Bell, Y. Hikita, H. Y. Hwang, H. Nakamura, T. Kimura, and Y. Wakabayashi. Structural comparison of n-type and p-type $LaAlO_3/SrTiO_3$ interfaces. *Phys. Rev. Lett.*, 107:036104, 2011.

[195] J.C. Yang, Q. He, S. J. Suresha, C. Y. Kuo, C. Y. Peng, R. C. Haislmaier, M. A. Motyka, G. Sheng, C. Adamo, H. J. Lin, Z. Hu, L. Chang, L. H. Tjeng, E. Arenholz, N. J. Podraza, M. Bernhagen, R. Uecker, D. G. Schlom, V. Gopalan, L. Q. Chen, C. T. Chen, R. Ramesh, and Y. H. Chu. Orthorhombic $BiFeo_3$. *Phys. Rev. Lett.*, 109:247606, 2012.

[196] J. B. Neaton, C. Ederer, U. V. Waghmare, N. A. Spaldin, and K. M. Rabe. First-principles study of spontaneous polarization in multiferroic $BiFeO_3$. *Phys. Rev. B*, 71:014113, 2005.

[197] S. J. Chiu, Y. T. Liu, H. Y. Lee, G. P. Yu, and J. H. Huang. Strain enhanced ferroelectric properties of multiferroic $BiFeO_3/SrTiO_3$ superlattice structure prepared by radio frequency magnetron sputtering. *Thin Solid Films*, 539:75–80, 2013.

[198] B. Ziegler, K. Martens, T. Giamarchi, and P. Paruch. Domain wall roughness in stripe phase $BiFeO_3$ thin films. *Phys. Rev. Lett.*, 111:3247604, 2013.

[199] R. R. Das, D. M. Kim, S. H. Baek, C. B. Eom, F. Zavaliche, S. Y. Yang, R. Ramesh, Y. B. Chen, X. Q. Pan, X. Ke, Rzchowski. M. S., and S. K. Streiffer. Synthesis and ferroelectric properties of epitaxial $BiFeO_3$ thin films grown by sputtering. *Appl Phys. Lett.*, 88:242904, 2006.

[200] S. H. Baek, H. W. Jang, C. M. Folkman, Y. Li, B. Winchester, J. X. Zhang, Q. He, Y. H. Chu, C.T. Nelson, M. S. Rzchowski, X. Q. Pan, R. Ramesh, L. Q. Chen, and C. B. Eom. Ferroelastic switching for nanoscale non-volatile magnetoelectric devices. *Nat. Materials*, 9:309, 2010.

[201] F. J. Garcia de Abajo, M. A. Van Hove, and C. S. Fadley. Multiple scattering of electrons in solids and molecules: A cluster-model approach. *Phys. Rev. B*, 63:075404, 2001.

[202] A. Z. Simões, A. H. M. Gonzalez, L. S. Cavalcante, C. S. Riccardi, E. Longo, and J. A. Varela. Ferroelectric characteristics of $BiFeO_3$ thin films prepared via a simple chemical solution deposition. *J. Appl. Phys.*, 101:074108, 2007.

[203] D. N. Zhigalina O. M., Khmelenin, K. A. Vorotilov, N. M. Kotova, A. A. Mazitov, I. S. Seregin, and N. B. D'yakonova. Structure and phase composition of $BiFeO_3$: La films synthesized by chemical deposition from solutions. *Phys. Solid State*, 54:997–998, 2012.

[204] M. K. Singh, H. M. Jang, S. Ryu, and M. H. Jo. Polarized raman scattering of multiferroic $BiFeO_3$ epitaxial films with rhombohedral R_3c symmetry. *Appl. Phys. Lett.*, 88:042907, 2006.

[205] C. Beekman, A. A. Reijnders, Y. S. Oh, S. W. Cheong, and K. S Burch. Raman study of the phonon symmetries in $BiFeO_3$ single crystals. *Phys. Rev. B*, 86:020403, 2012.

[206] T. Yamashita and P. Hayes. Analysis of XPS spectra of Fe^{2+} and Fe^{3+} ions in oxide materials. *Appl. Surf. Sci.*, 254:2441–2449, 2009.

[207] T. J. Regan, H. Ohldag, C. Stamm, C. Nolting, J. Lüning, J. Stöhr, and R. L. White. Chemical effects at metal/oxide interfaces studied by X-ray absorption spectroscopy. *Phys. Rev. B*, 64:214422, 2001.

[208] V. R. Singh, V. K. Verma, K. Ishigami, G. Shibata, Y. Yamazaki, A. Fujimori, Y. Takeda, T. Okane, Y. Saitoh, H. Yamagami, Y. Nakamura, M. Azuma, and Y. Shimakawa. Enhanced ferromagnetic moment in Co-doped $BiFeO_3$ thin films studied by soft x-ray circular dichroism. *J. Appl. Phys.*, 114:103905, 2013.

[209] S. Brice-Profeta, M. A. Arrio, E. Tronc, N. Menguy, I. Letard, C. Cartier dit Moulin, M. Nogués, C. Chaneác, J. P. Jolivet, and P. Sainctavit. Magnetic order in γ-Fe_2O_3 nanoparticles:a XMCD study. *Journal of Magnetism and Magnetic Materials*, 288:354–365, 2005.

[210] G. Drera, A. Giampietri, I. Alessandri, E. Magnano, F. Bondino, and S. Nappini. Grain size and stoichiometry control over RF-sputtered multiferroic $BiFeO_3$ thin films on silicon substrates. *Thin Solid Films*, 589:551–555, 2015.

[211] Y. Chen, N. Pryds, J. E. Kleibeuker, G. Koster, J. Sun, E. Stamate, B. Shen, G. Rijnders, and S. Linderoth. Metallic and insulating interfaces of amorphous $SrTiO_3$-based oxide heterostructures. *Nano Lett.*, 11:3774–3778, 2011.

[212] C. Mix, S. Finizio, M. Buzzi, F. Kronast, F. Nolting, G. Jakob, and M. Kläui. Direct observation of temperature dependent magnetic domain structure of the multiferroic $La_{0.66}Sr_{0.34}MnO_3/BiFeO_3$ bilayer system by x-ray linear dichroism- and x-ray magnetic circular dichroism-photoemission electron microscopy. *J. Appl. Phys.*, 115:193901, 2014.

[213] T. Fujii, M. Yamashita, S. Fujimori, Y. Saitoh, T. Nakamura, K. Kobayashi, and J. Takada. Large magnetic polarization of Ti^{4+} ions in $FeTiO_3$. *J. Magn. Magn. Mater.*, 310:e555–e557, 2007.

[214] A. Fujimori, M. Saeki, and N. Kimizuka. Photoemission satellites and electronic structure of Fe_20_3. *Phys. Rev. B*, 34:7318–7328, 1986.

[215] M. Cardona. Optical properties and band structure of $SrTiO_3$ and $BaTiO_3$. *Phys. Rev.*, 140:A651, 1965.

[216] S. J. Clark and J. Robertson. Band gap and schottky barrier heights of multiferroic $BiFeO_3$. *Appl. Phys. Lett.*, 90:132903, 2007.

[217] Y. Z. Chen, N. Bovet, F. Trier, D. V. Christensen, F. M. Qu, N. H. Andersen, T. Kasama, W. Zhang, R. Giraud, J. Dufouleur, T. S. Jespersen, J. R. Sun, A. Smith, J. Nygård, L. Lu, B. Büchner, B. G. Shen, S. Linderoth, and N. Pryds. A high-mobility two-dimensional electron gas at the spinel/perovskite interface of γ-$Al_2O_3/SrTiO_3$. *Nat. Commun.*, 4:1371, 2013.

[218] T. Q. Ngo, N. J. Goble, A. Posadas, K. J. Kormondy, S. Lu, M. D. McDaniel, J. Jordan-Sweet, D. J. Smith, X. P. A. Gao, A. A. Demkov, and J. G. Ekerdt. Quasi-two-dimensional electron gas at the interface of γ-$Al_2O_3/SrTiO_3$ heterostructures grown by atomic layer deposition. *J. Appl. Phys.*, 118:115303, 2015.

[219] K. Ueno, I. H. Inoue, H. Akoh, M. Kawasaki, Y. Tokura, and H. Takagi. Field-effect transistor on $SrTiO_3$ with sputtered Al_2O_3 gate insulator. *Appl. Phys. Lett.*, 83:1755–1757, 2003.

[220] C. Franchini, X. Chen, and R. Podloucky. Thickness dependent structural and electronic properties of CuO grown on $SrTiO_3$(100): a hybrid density functional theory study. *J. Phys.: Condens. Matter*, 23:045004, 2011.

[221] S. Åsbrink and L. J. Norrby. A refinement of the crystal structure of copper(ii) oxide with a discussion of some exceptional e.s.d.'s. *Acta Cryst.*, B26:8–15, 1970.

[222] W. Siemons, G. Koster, D. H. A. Blank, R. H. Hammond, T. H. Geballe, and M. R. Beasley. Tetragonal CuO: End member of the 3d transition metal monoxides. *Phys. Rev. B*, 79:195122, 2009.

[223] J. Bednorz and K. Muller. Perovskite-type oxides - The new approach to high-T_c superconductivity. *Rev. Mod. Phys.*, 60:585–600, 1988.

[224] I. M. Dildar, M. Neklyudova, Q. Xu, S. Zandbergen, H. W.and Harkema, D. Boltje, and J. Aarts. Growing $LaAlO_3/SrTiO_3$ interfaces by sputter deposition. *AIP Ad-*

vances, 5:067156, 2015.

[225] L. Debbichi, M. C. Marco de Lucas, J. F. Pierson, and P. Krüger. Vibrational properties of CuO and Cu_4O_3 from first-principles calculations, and raman and infrared spectroscopy. *J. Phys. Chem. C*, 116:10232–10237, 2012.

[226] S. Poulston, P. M. Parlett, P. Stone, and M. Bowker. Surface oxidation and reduction of CuO and Cu_2O studied using XPS and XAES. *Surface and Interface Analysis*, 24:811–820, 1996.

[227] G. Van der Laan, C. Westra, C. Haas, and G. A. Sawatzky. Satellite structure in photoelectron and auger spectra of copper dihalides. *Phys. Rev. B*, 23:4369–4380, 1981.

[228] J. Zaanen and G. A. Sawatzky. The electronic structure and superexchange interactions in transition-metal compounds. *Canadian Journal of Physics*, 65:1262–1271, 1987.

List of Figures

List of Tables

List of Publications

As of 01/12/2016

Refereed publications

- **A. Giampietri**, G. Drera, I. Píš, E. Magnano, L. Sangaletti, *Tracking the amorphous to epitaxial transition in RF-sputtered cubic BFO-STO heterojunctions by means of X-ray photoelectron diffraction*, Applied Physics Letters **109** (2016) 132903

- G. Drera, **A. Giampietri**, I. Alessandri, E. Magnano, F. Bondino, S. Nappini, *Grain size and stoichiometry control over RF-sputtered multiferroic $BiFeO_3$ thin films on silicon substrates*, Thin Solid Films, **589** (2015) 551-555

- G. Salvinelli, G. Drera, **A. Giampietri**, L. Sangaletti, *Layer-Resolved Cation Diffusion and Stoichiometry at the $LaAlO_3/SrTiO_3$ Heterointerface Probed by X-ray Photoemission Experiments and Site Occupancy Modeling*, ACS applied materials & interfaces **7** (2015) 25648-25657

Publications in preparation

- **A. Giampietri**, G. Drera, L. Sangaletti, *Band alignment at the heteroepitaxial perovskite oxide interfaces: $LaAlO_3/SrTiO_3$ and beyond*, to be submitted to Advanced Materials Interfaces as mini-review

- G. Drera, A. Giampietri, A. Verdini, L. Floreano, A. Cossaro, L. Sangaletti, *Electronic properties and in-gap states of the sputtered and annealed (001) surface of $SrTiO_3$ single crystals*, in preparation

- **A. Giampietri**, G. Drera, F. Taglietti, L. Sangaletti, *Electronic properties of tetragonal CuO epitaxial layers grown on $SrTiO_3$*, in preparation

Conference presentations

- *Novel multifunctional applications of RF-sputtered $BiFeO_3/SrTiO_3$: the influence of long range crystal order probed by X-ray photoelectron diffraction*, oral presentation at: E-MRS 2016 Fall Meeting (19-22 September 2016, Warsaw)
- *Epitaxial growth of $BiFeO_3$ thin films by RF sputtering: effects of substrate termination and grain-size control*, poster presentation at: TRENDOXIDES2015 - New TRENDS in Correlated OXIDES and Interfaces (12-18 November 2015, Brescia)
- *Epitaxial growth of $BiFeO_3$ thin films by RF sputtering: effects of substrate termination and grain-size control*, poster presentation at: XIII School on Synchrotron Radiation: Fundamentals, Methods and Applications (14-25 September 2015, Grado (GO))
- *Characterization of multiferroic $BiFeO_3$ polycrystalline thin films grown by RF sputtering*, poster presentation at: SuperFOx 2014 - Second Conference on Superconductivity and Functional Oxides (24-26 September 2014, Roma)

Beamtimes

- *Hybridized carbon electronic states in strongly and weakly interacting graphene-nickel interfaces probed by resonant and dichroic angle-resolved photoemission*, BACH Beamline at Elettra Sincrotrone (16-20 May 2016, Basovizza (Trieste))
- *Ti 3d electronic states in ultrathin epitaxial $BiFeO_3/SrTiO_3$ interface probed through resonant photoemission*, BACH Beamline at Elettra Sincrotrone (11-17 April 2016, Basovizza (Trieste))
- *Probing interface effects in TiO_2 based magnetic oxides with dichroic X-ray absorption spectroscopies*, BACH Beamline at Elettra Sincrotrone (21-25 May 2014, Basovizza (Trieste))
- *Resonant angle resolved photoelectron spectroscopy of buried interface in $LaAlO_3/SrTiO_3$ heterostructures*, BACH Beamline at Elettra Sincrotrone (1-6 April 2014, Basovizza (Trieste))

Other publications in preparation

- G. Drera, S. Pagliara, **A. Giampietri**, C. Pintossi, L. Sangaletti, C. Cepek, F. Bondino, E. Magnano, S. Nappini, N. Joshi, P. Ghosh, A. Barla, S. K. Mahatha, *Identification of Γ-point hybridized electronic states with p character at different growth stages of graphene on Ni(111)*, to be submitted to Phys. Rev. B

Acknowledgments

- I'm grateful to Prof. Luigi Sangaletti and to Dr. Giovanni Drera, since they taught me almost everything I know about UHV technology, XPS, growth and characterization of oxide heterostructures.
- I wish to thank my parents and relatives for the constant moral and economic support during all the university studies.
- I want to thank my friends, especially Romeo, Stefano (both of them), Cristian, Cesare and Valentina, for the time spent together having fun, which helped me to fight the stress and to keep the morale high.
- I need to thank all the colleagues I worked with during the last three years, especially Emanuele, Stefano, Silvia, Chiara and Federica, for both the ordinary moments and the unforgettable situations.
- I'd like to thank all the people who socialized with me during the doctorate course, especially the great group met at the XIII SILS summer school.